University of Florida
Civil and Coastal Engineering

University of Florida
Civil and Coastal Engineering

Final Report **May 2009**

SHEAR PERFORMANCE OF EXISTING PRESTRESSED CONCRETE BRIDGE GIRDERS

Principal investigator:
H. R. Hamilton III

Research assistants:
Gustavo Llanos
Brandon E. Ross

Department of Civil and Coastal Engineering
University of Florida
P.O. Box 116580
Gainesville, Florida 32611

Sponsor:
Florida Department of Transportation (FDOT)
Marcus H. Ansley, P.E. – Project Manager

Contract:
UF Project No. 00056470
FDOT Contract No. BD 545-56

DISCLAIMER

The opinions, findings, and conclusions expressed in this publication are those of the authors and not necessarily those of the State of Florida Department of Transportation.

Technical Report Documentation Page

1. Report No.	2. Government Accession No.	3. Recipient's Catalog No.
BD 545-56		

4. Title and Subtitle	5. Report Date
Shear Performance of Existing Prestressed Concrete Bridge Girders	May 2009
	6. Performing Organization Code

7. Author(s)	8. Performing Organization Report No.
Gustavo Llanos, Brandon E. Ross, and H. R. Hamilton III	00056470

9. Performing Organization Name and Address	10. Work Unit No. (TRAIS)
University of Florida Department of Civil & Coastal Engineering P.O. Box 116580 Gainesville, FL 32611-6580	11. Contract or Grant No. BD 545-56

12. Sponsoring Agency Name and Address	13. Type of Report and Period Covered
Florida Department of Transportation Research Management Center 605 Suwannee Street, MS 30 Tallahassee, FL 32301-8064	Final Report
	14. Sponsoring Agency Code

15. Supplementary Notes

16. Abstract

This report presents the results of testing conducted on three types of concrete bridge girders: AASHTO Type IV, AASHTO Type III, and circa 1950's Post-Tensioned Girders. Testing generally focused on shear capacity and behavior under shear loading.

The AASHTO Type IV test girders were built to replicate existing girders that are in service in Florida. It was found that capacity was not controlled by the typical shear failure mechanisms, but rather was due to the cracking and separation of the bottom bulb flange of the girder. This was a result of the unusual debonding pattern that placed the fully bonded strands out in the bulb flange and the debonded strands under the web. A CFRP fabric strengthening scheme was tested to mitigate issues associated with the strand debonding pattern. The bonded CFRP reinforcement provided an increase in capacity of nine and 21 percent for shear span-to-depth (a/d) ratios of one and three, respectively.

The AASHTO Type III test girders were salvaged from an existing bridge. Specimens were tested at a/d ratios ranging from one to five. For a/d ratios of three or less, the failure mode was strand slip, which was precipitated by the formation of cracks in the strand development length zone. While these cracks resulted in strand slip, transverse and longitudinal mild steel reinforcement at the girder end were engaged, which improved the capacity and ductility beyond first strand slip.

Post-Tensioned test girders were constructed to replicate a circa 1950s bridge design. Unique features included presence of both straight and parabolic PT bars, and lack of shear reinforcement away from the end block. The girder tested with a direct bearing on concrete displayed a 7% larger capacity and nearly half the displacement capacity of the girder tested on neoprene.

17. Key Words	18. Distribution Statement
prestressed concrete, shear, pretensioned, post-tensioned, bridge girder	No restrictions. This document is available to the public through the National Technical Information Service, Springfield, VA, 22161

19. Security Classif. (of this report)	20. Security Classif. (of this page)	21. No. of Pages	22. Price
Unclassified	Unclassified	148	

Form DOT F 1700.7 (8-72) Reproduction of completed page authorized

ACKNOWLEDGMENTS

The authors would like to acknowledge and thank the Florida Department of Transportation for funding this research project. In addition, the authors would like to thank, David Allen, Frank Cobb, Steve Eudy, Tony Hobbs, Will Potter, Paul Tighe, and Chris Weigly, of the FDOT Structures Research Center in Tallahassee for their assistance with the design, fabrication, and testing of these girders. The authors would also like to thank Marc Ansley for his technical input and support. The assistance of Adrian Lawrence and Sujatha Kalyanam in the construction and testing of the Type IV girders is gratefully acknowledged.

EXECUTIVE SUMMARY

This report presents the results of testing conducted on three types of concrete bridge girders: AASHTO Type IV, AASHTO Type III, and circa 1950's Post-Tensioned Girders. Testing generally focused on shear capacity and behavior under shear loading.

The AASHTO Type IV test girders were built to replicate existing girders that are in service in Florida. It was found that capacity was not controlled by the typical shear failure mechanisms, but rather was due to the cracking and separation of the bottom bulb flange of the girder. This was a result of the unusual debonding pattern that placed the fully bonded strands out in the bulb flange and the debonded strands under the web. A CFRP fabric strengthening scheme was tested to mitigate issues associated with the strand debonding pattern. The bonded CFRP reinforcement provided an increase in capacity of nine and 21 percent for shear span-to-depth (a/d) ratios of one and three, respectively.

The AASHTO Type III test girders were salvaged from an existing bridge. Specimens were tested at a/d ratios ranging from one to five. For a/d ratios of three or less, the failure mode was strand slip, which was precipitated by the formation of cracks in the strand development length zone. While these cracks resulted in strand slip, transverse and longitudinal mild steel reinforcement at the girder end were engaged, which improved the capacity and ductility beyond first strand slip.

Post-Tensioned test girders were constructed to replicate a circa 1950s bridge design. Unique features included presence of both straight and parabolic PT bars, and lack of shear reinforcement away from the end block. The girder tested with a direct bearing on concrete displayed a 7% larger capacity and nearly half the displacement capacity of the girder tested on neoprene.

TABLE OF CONTENTS

LIST OF FIGURES

LIST OF TABLES

1 INTRODUCTION

1.1 OVERVIEW

Florida has a significant number of bridges with prestressed concrete girders as the primary superstructure elements. This form of construction has been used for nearly 60 years. Consequently, the design approach and construction style has varied over the years as codes have changed and needs have changed.

1.2 OBJECTIVES AND APPROACH

This research report covers load testing of bridge girders that have been used to construct bridges in Florida. Some of the testing was conducted on girders that were recovered during bridge demolition and others were constructed using the same design as girders that are currently in service. The common element of the testing was to determine the capacity of the girders under three-point bending. The shear span-to-depth ratio for the tests ranged from one to five depending on the number of specimens and specific target behavior.

1.3 REPORT ORGANIZATION

This report is divided into chapters that cover each of the three testing programs. In addition, the background chapter covers the approach used to test the girders and the current code provisions used to calculated the design capacity for these girders. Following the background chapter is the nomenclature and the test data chapter. This chapter describes the notation used to describe the instrumentation to aid in interpreting the data files. Data gathered during each of the load tests will be available in electronic format in separate data files.

Next are the three primary chapters that each report on the respective testing. The first covers the testing of two AASHTO Type IV girders to evaluate the effect of unconventional debonding patterns used in the early 1980's and a repair scheme used to improve the capacity. The next chapter covers the testing of four AASHTO Type III girders that were constructed in 1979. These tests were conducted to evaluate the capacity of the girder and the effect of the light shear reinforcement. Finally, three post-tensioned girders were constructed to replicate early (circa 1950's) post-tensioned concrete girders. They were tested with a/d of two and three. The effects of different bearing conditions were also evaluated.

2 BACKGROUND

AASHTO Type III, Type IV pretensioned girders along with a custom post-tensioned girder were tested in this research program. The primary focus was on short shear spans to determine the shear behavior of the girders that had been used in FDOT bridges in service. Three-point loading was chosen to ensure that majority of the failure modes were not flexural. Brown et al. (2006) indicated that generally the shear strength of girders with uniform loads are greater than when loaded with concentrated loads. Consequently, using a test configuration with concentrated loads will ensure that the results are applicable for uniform load conditions.

Figure 1 shows that strut and tie action begins to dominate behavior as the shear span ratio (a/d) drops below approximately 2.5. Above this mark, the plot indicates that a sectional model controls. This is presumed to indicate that either shear or flexure will control the failure mode. Although the exact point is dependent on the specific conditions of the testing and specimen, this provides reasonable guidance on the selection of a shear span ratio for conducting shear testing.

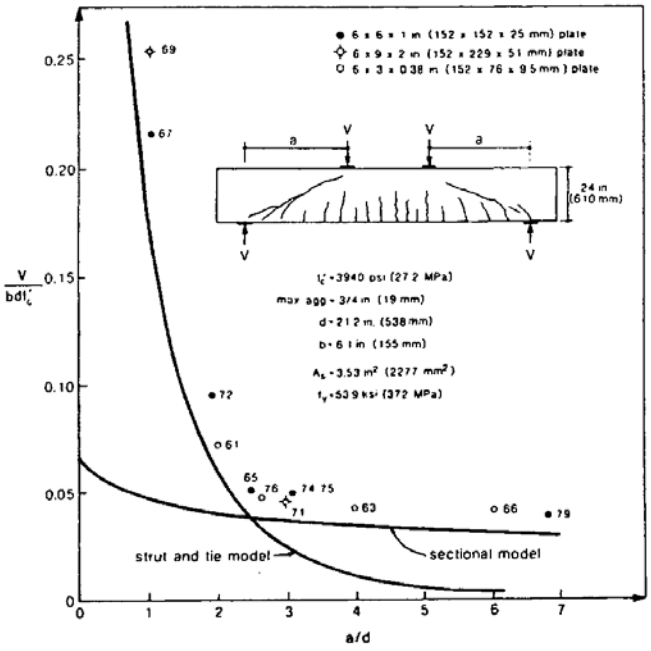

Figure 1 – Strength of concrete beams with short shear spans. (Collins and Mitchell (1991))

When a/d is less than about 2.5 in pretensioned concrete girders, the peak capacity is typically marked by slipping of the prestressing strand at the end of the girder. This behavior has been characterized as a type of flexural failure in which the distance from the support to the critical section is less than the development length of the strand (Ramirez and Russell 2007). It can also be modeled as a strut and tie in which the tie capacity (prestressing tendon) is limited by the anchorage. In either case, the fundamental controlling issue is the anchorage of the prestressing tendon and supplemental reinforcement provided in the end region. End blocks and various end reinforcement schemes will marginally improve the capacity of a girder that is prone to this failure mode.

The literature covering shear in concrete is expansive. The particular focus of each set of tests in this research was slightly different depending on the objectives and was not particularly focused on revising shear design provisions, but rather in evaluating the capacity of existing bridge girders. Consequently, rather than providing an exhaustive treatise on the history of research in shear of beams the reader is directed to a recent NCHRP report that focused on simplifying the AASHTO provisions for shear (Hawkins et al. 2005). Further information specific to shear provisions for prestressed concrete can be found in Avendano and Bayrak (2008). The remainder of this chapter is devoted to a general background of methods currently used to calculate the shear capacity of prestressed concrete girders.

This report compares the results obtained from load testing to ACI 318 Building Code Requirements for Structural Concrete (2008), AASHTO LRFD Bridge Design Specifications (2007). For the remainder of this report these provisions will be referred to as "ACI" and "LRFD," respectively.

ACI presents a section-based approach for calculating the design shear strength of prestressed concrete girders. The contribution of the concrete and the steel reinforcement are calculated independently, then added together to determine the total design strength. For prestressed concrete, the concrete contribution is calculated using a single simplified equation, or by using more detailed equations. The detailed method considers the strength of the concrete against web cracking due to diagonal principal tensile stresses, and against flexural-shear cracking due to combined moment and shear. The ACI detailed method was added to the LRFD as an alternative method to MCFT and is referred to in AASHTO as the "simplified method". This method is also used in The AASHTO Standard Specifications for Highway Bridges, which

is sometimes still used for load rating existing bridges in Florida. The two primary equations for calculating the resistance provided by the concrete are:

$$V_{ci} = 0.6\sqrt{f'_c}\,b_w d_p + V_d + \frac{V_i M_{cre}}{M_{\max}} \qquad \text{Eqn. 1}$$

$$V_{cw} = (3.5\sqrt{f'_c} + 0.3 f_{pc}) b_w d_p + V_p \qquad \text{Eqn. 2}$$

Where:

V_{ci} = Nominal shear strength provided by concrete when diagonal cracking results from combined shear and moment.

f'_c = Specified compressive strength of concrete.

b_w = Web width.

d_p = Distance from extreme compression fiber to centroid of prestressing steel.

V_d = Shear force at section due to unfactored dead load.

V_i = Factored shear force at section due to externally applied loads occurring simultaneously with M_{max}.

M_{cre} = Moment causing flexural cracking at section due to externally applied loads.

M_{max}= Maximum factor moment at section due to externally applied loads.

V_{cw} = Nominal shear strength provided by concrete when diagonal cracking results from high principal tensile stress in web.

f_{pc} = Resultant compressive stress at centroid of composite section due to both prestress and moments resisted by non-composite section acting alone.

V_p = Vertical component of effective prestress force at section.

The shear design provisions in LRFD are based on the Modified Compression Field Theory (MCFT). The basis of MCFT is the assumption that diagonal cracks form a series (or field) of concrete compression struts in the web. The transverse tension in the struts is zero at the cracks, but is nonzero between cracks. The net effect of the concrete tension, summed over multiple cracks is the concrete contribution to the shear resistance. As part of the calculations for the concrete contribution, LRFD gives equations for calculating the angle of the inclined cracks. The primary equation, LRFD Equation 5.8.3.3-3, used to calculate the concrete contribution to shear capacity by MCFT is:

$$V_c = 0.0316\beta\sqrt{f'_c}\,b_v d_v \qquad \text{Eqn. 3}$$

where:

V_c = Nominal shear strength provided by concrete.

β = Factor indicating ability of diagonally cracked concrete to transmit tension and shear as specified by AASHTO article 5.8.3.4

f'_c = Specified compressive strength of concrete.

b_v = Effective web width taken as the minimum web width within the depth d_v.

d_v = Effective shear depth as determined in AASHTO article 5.8.2.9.

Calculating β is an iterative process requiring the use of factors from LRFD. Results from calculations using this method are denoted as "MCFT" through this report.

Several of the load tests in this research involved load points that are close to the reaction. In these tests, sectional models are insufficient to capture the complexity of the stress state. The flow of forces, however, can be reduced to series of struts and ties. Struts are assumed to be regions of concrete that can safely transfer compressive load from node to node. Likewise, ties carry tension and are assumed to occur in reinforcement that extend uninterrupted from node to node. The transfer of forces can then be studied using statics and the truss formed by the struts, ties, and nodes. Individual capacities of struts, ties, and nodes are checked to ensure sufficient strength. LRFD was used to calculate the strut and tie capacity for tests with short shear spans. Results from this method are denoted as "Strut and Tie", or "STM" throughout this report.

3 NOMENCLATURE AND TEST DATA

The data gathered during testing are available from the FDOT Research Office website in comma delimited (.csv) format (http://www.dot.state.fl.us/Research-Center/). The data from each test are included in a single electronic file that includes that particular test name in the filename. The data in each file are arranged so that the readings from a single instrument occupy one column. That instrument name is included in the column heading. Each row of data represents a single data acquisition scan. The nomenclature used in the electronic files is the same as that used in the following sections of this report (Figure 2).

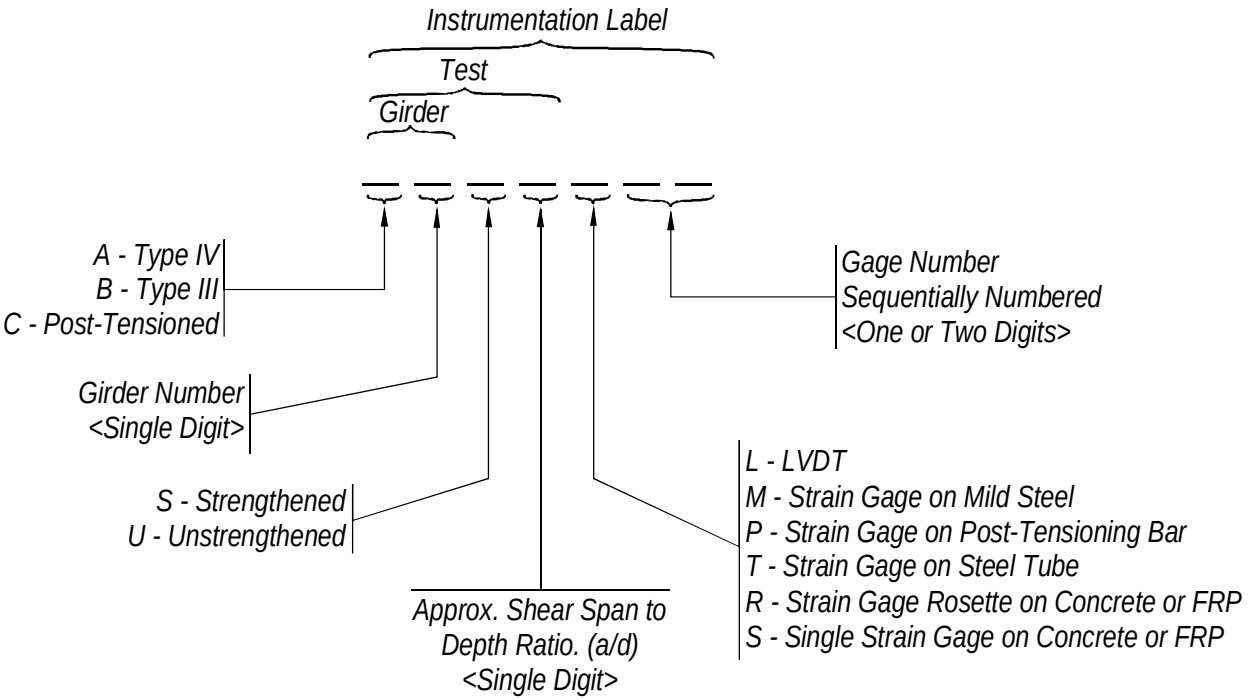

Figure 2 – Girder nomenclature.

Some examples of nomenclature use are as follows:

1. *C1* denotes specimen one of PT girders.
2. *A2S2* denotes a strengthened Type IV girder with an a/d of approximately two.
3. *B2U3L3* denotes LVDT number three on Type III unstrengthened girder two with an a/d of approximately three.
4. *C1U3R2_45* is a strain gage (within a rosette) that is oriented to read strain at a 45 deg angle from the beam axis. The gage number is two and it was used on specimen one of the PT girders with an a/d ratio of approximately three.

Instrumentation layout for each test is located in the respective sections of the report and can be used to cross-reference the data to the particular girder, test, orientation, and location for which that instrument was used. Each strain gage rosette is an array of three individual strain gages. The rosette gage numbers in the data files are followed by an underscore and the angle of that particular gage relative to the beam axis.

The recovered Type III girders were delivered with labels that were used by the demolition contractor during removal. Table 1 provides the cross reference between the names used in this report and the original girder designation used by the contractor.

Table 1 – Labeling of Type III girders.

New Girder Designation	Original Girder Designation
1	3H
2	3L
3	1J
4	1H

4 AASHTO TYPE IV GIRDERS

4.1 OBJECTIVES

The objective of this testing was to determine the behavior of AASHTO Type IV girders constructed with excessive debonded strands and loaded in three-point bending. Furthermore, carbon FRP (CFRP) composites were used to strengthen one end of each girder. Identical tests were conducted on strengthened and unstrengthened ends of each girder to compare the improvement in capacity and difference in behavior provided by the CFRP composites. Current design methods were evaluated by comparison with the experimental results.

4.2 BACKGROUND

Razaqpur and Isgor (2006) proposed a method for calculating the shear capacity of FRP-reinforced concrete without stirrups. This method accounts for the contribution of plain concrete and the contribution of the aggregate interlock mechanism. The method was compared to other methods such as the Canadian Standards Association (CSA), American Concrete Institute (ACI), a method proposed by Frosch and Tureyen, and the Japanese Society for Civil Engineers (JSCE). Comparisons were made using experimental results in the literature for 63 beams. The average standard deviation of the other methods ranged from 0.39 to 1.95 while the proposed method had an average standard deviation of 0.27. Saenz and Pantelides (2005) administered push-off tests with varying CFRP laminate wrap configurations (Figure 3). Experimental results found that the CFRP does not begin to contribute capacity until the concrete shear capacity is reached. This finding shows that the failure with these CFRP wraps has two stages, imposed shear stress is controlled by concrete alone and then the CFRP begins to carry shear force by acting as a clamp and an interlocking mechanism for the aggregate. The member can carry force until cohesive concrete failure or bond failure between the CFRP laminate and concrete. The capacity of specimens strengthened with CFRP increased by a factor of 1.32 to 3.25 for a CFRP reinforcement ratio of 0.3-1.2%.

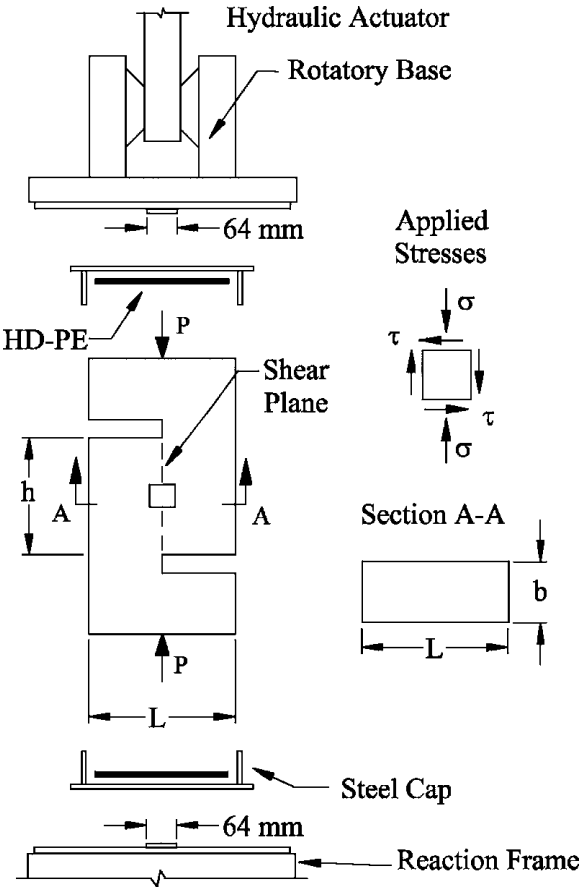

Figure 3 – Push-off test.

Khalifa and Nanni (2000) tested reinforced concrete (RC) beams with different confirgurations of CFRP applied. A control beam without CFRP failed at an ultimate strength, V_n, of 20 kips. The minimum shear capacity of the strengthened beams was 27 kips, showing that CFRP provides the beam with additional capacity. Two of the five configurations were continuous sheets in the form of U-wraps. In the first configuration, the ends of the wraps were anchored into the side of the beam. The other configuration was unanchored. The anchored specimen reached a peak V_n of 50 kips and failed due to flexure while the unanchored specimen reached a peak V_n of 35 kips and failed due to the CFRP debonding. The results show that anchoring the laminate the CFRP provides additional capacity, and can lead to a different failure mode.

4.3 APPROACH

Test girders were constructed to replicate existing Type IV girders that are in service in Florida. These girders are of particular interest because they have a debonding pattern that is in violation of the LRFD specification.

Two precast girders were constructed at Dura Stress in Leesburg, FL and shipped to the FDOT Structures Laboratory in Tallahassee, FL for testing. One end of each girder was strengthened using externally applied CFRP fabric. Both the strengthened and unstrengthened ends were tested in three point bending. A shear span-to-depth (a/d) ratio of 1.5 was used for testing one girder, and a ratio of three was used for testing the other girder. The effect of the CFRP strengthening was evaluated by comparing results of the strengthened and unstrengthened tests.

4.4 GIRDER DESIGN

The original girders were designed to support an 8-in. thick bridge deck over a approximately 100-ft. span. They were spaced at 9.25 ft. on center and prestressed with 9/16-in. diameter strands. Testing restrictions dictated that the test girders be shortened to a length of 60-ft. Furthermore, the lack of availability of 9/16-in. strand required that 0.6-in. diameter strand be used. The design jacking force for 9/16-in. diameter strand was used during construction.

ASTM A416 Grade 270 strands were used in the pattern shown in Figure 4. The debonding pattern matches that used in the original girders, which violates current LRFD requirements. The shortened girder length required that four of the strands be debonded over the entire length.

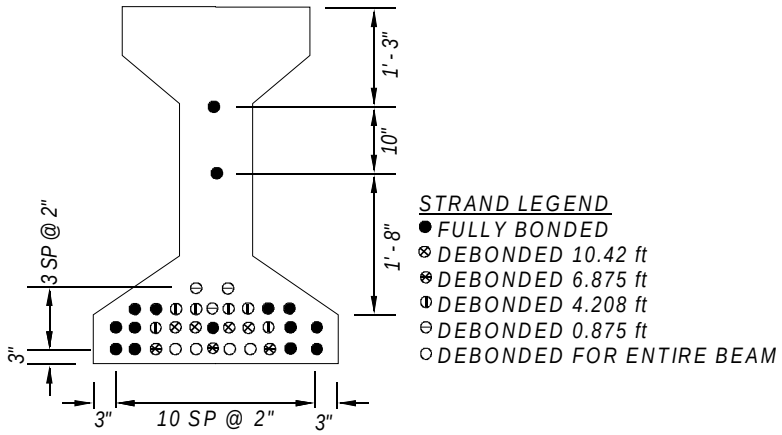

Figure 4 – Girder cross section and strand details.

Figure 5 shows the stirrups and end region reinforcement, in which ASTM – A615 Grade 60 epoxy coated reinforcement was used. The ends were densely reinforced with #6 and #5 bars. The remainder of the girder was reinforced with #4 stirrups spaced at 6 inches on center. The stirrups protruded from the top of the precast section to provide shear transfer between the girder and the deck.

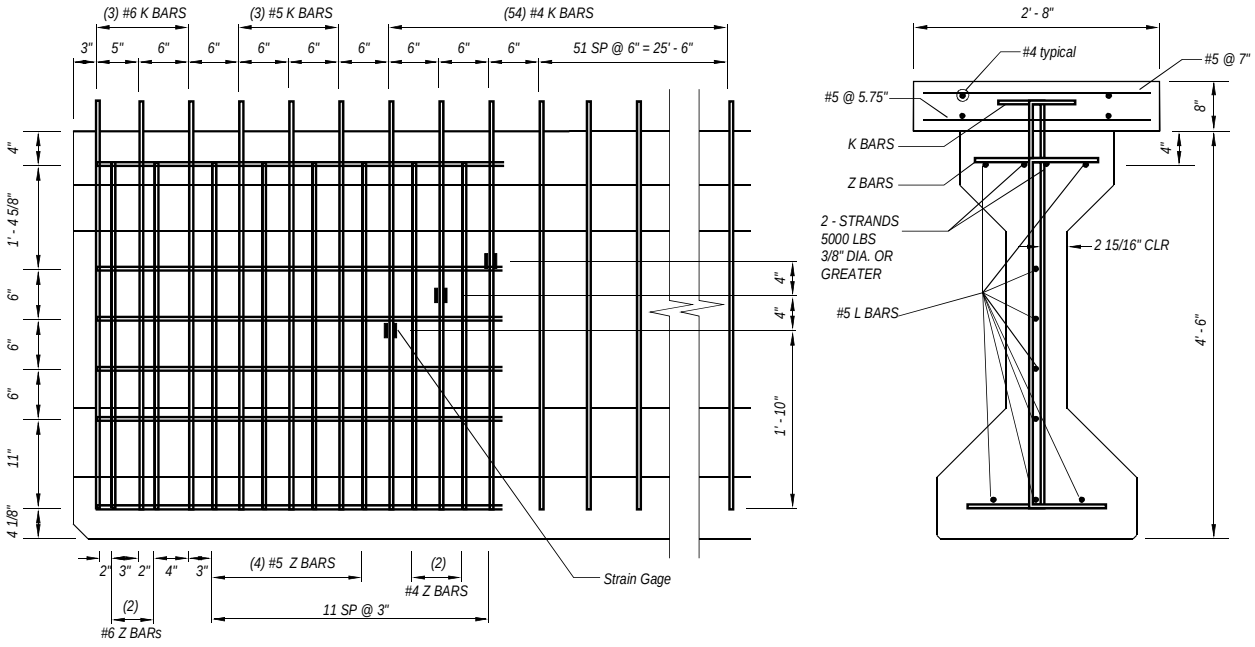

Figure 5 – Stirrup size and configuration.

4.5 GIRDER CONSTRUCTION AND MATERIAL PROPERTIES

The Type IV test girders were constructed in the same stressing bed at Dura-Stress in Leesburg, FL (Figure 6). Each girder required two batches of concrete. Girders were consolidated both internally and externally. The top surface was intentionally roughened to provide horizontal shear transfer between the girder and the topping slab. Prestress was transferred after the required compressive strength (4500 psi) was reached. Girders were transported to the FDOT Structures Laboratory for testing. The concrete cap was cast on each girder at the FDOT structures laboratory using a commercial ready mix concrete with a specified compressive strength of 4000 psi. The cap was allowed to cure for 28-days minimum before the girders were tested.

Figure 6 – Reinforcement and prestressing placement

Figure 7 – Prestress transfer and girder ready for shipping.

Concrete properties were obtained from compression tests on 8-in. tall x 4-in. diameter cylinders and from modulus of rupture (MOR) tests on 4-in. x 4-in. x 8-in. beam. Twenty cylinders and two beams were made from the second batch of concrete, and were representative of the first girder. Twenty additional cylinders and two additional beams were made from the fourth batch of concrete, and were representative of the second girder.

Eight cylinders were tested for each girder to obtain the strength gain curve of the concrete. For both mixtures, the coefficient of variation of the test results of was found to be

within the limiting percentage set by ASTM. Two cylinders were tested for each girder to determine the release strength (Table 2). Three cylinders were tested for each girder to determine the 28-day strength and compressive strength on the day the girders were tested. The design 28-day compressive strength (f'_c) was 5,500 psi. The compressive strength of the deck was 6400 psi.

The remaining cylinders, as well as the MOR beams, were tested on the days coinciding with the load tests of the girders. These test results, as well as the plastic properties of the concrete, are located in Appendix A.

Table 2 – Average girder concrete compressive strength (psi) at indicated ages.

Girder	Release	28-day	Test Day
A1	5340	6270	7220
A2	5430	6030	7180

Four samples of the prestressing strand were tested. The ultimate strength and modulus of elasticity values are reported in the Appendix A. The data indicate that the strand complied with the requirements of ASTM A416, with an average ultimate strength of 280 ksi and an average ultimate elongation of 6.1%.

4.6 CFRP REPAIR

The repair is composed of bi-directional 18.7 oz/sq yd carbon fabric bonded to the girder as shown in Figure 8. The first layer of fabric has five 24-in. wide strips that wrap continuously around the bottom of the girder and terminate at the underside of the deck on each side of the girder. The top layer is composed of three longitudinal strips. Two of the strips are placed on the top bulb and the third strip is wrapped around the bottom bulb. A commercially available system was used for the repair. The manufacturer's test data for the system are included in Table 3.

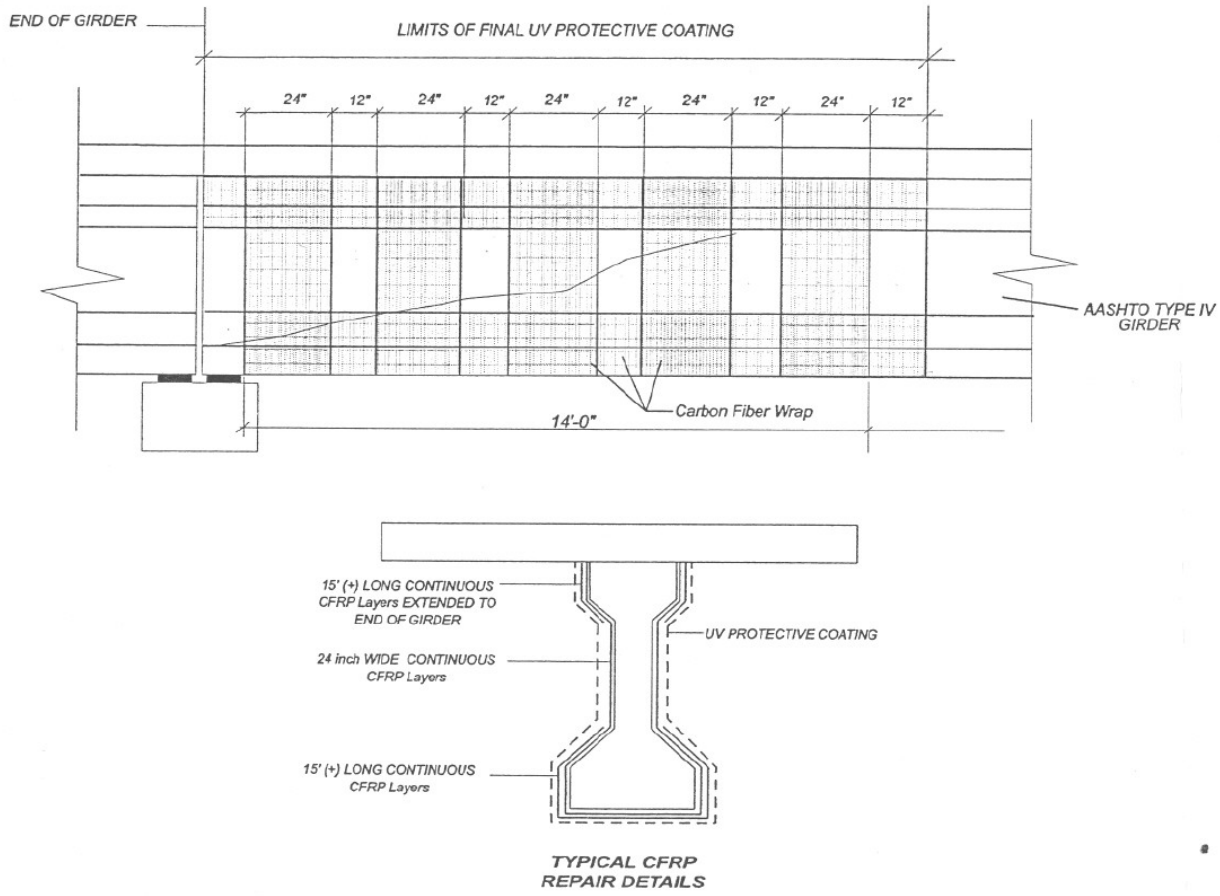

Figure 8 – CFRP repair configuration.

Table 3 – Manufacturer's test data.

Properties after standard cure followed by standard post cure. [70°-75°F (21°-24°C) - 5 days and 48 hour post cure at 140°F (60°C)]

	Average Value[1]		Design Value[2]		ASTM Test
Property	**US Units**	**SI Units**	**US Units**	**SI Units**	**Method**
	Psi	MPa	psi	MPa	
Tensile Strength*	83,980	579	70,870	489	D638
Tensile Modulus*	7,017,555	48,351	6,149,730	42,468	D638
Tensile % Elongation *	1.14	1.14	0.98	0.98	D638
140F - Tensile Strength	74,195	511	64,790	447	D638
140F - Tensile Modulus	6,340,680	43,688	6,203,025	43,739	D638
140F - % Elongation	1.12	1.12	0.96	0.96	D638
Compressive Strength	54,245	373	38,570	267	D695
Compressive Modulus	6,707,855	46,218	6,496,100	44,759	D695
90 deg Tensile Strength	83,980	579	70,870	489	D638
90 deg Tensile Modulus	7,017,555	48,351	6,930,773	47,753	D638
90 deg %Tensile Elongation	1.14	1.14	0.98	0.98	D638
Shear Strength-+/-45 In Plane	14,630	101	12,920	89	D3518
Shear Modulus +/-45 In Plane	0	0	0	0	D3518
Ply Thickness (inch/mm)	0.04	1			
Tensile Strength per inch width in each direction	3359	14.9	2834	12.6	D3039

The installation procedure used to apply the CFRP was as follows:

1. Surface was sandblasted and then sharp corners were ground to facilitate bonding of fabric (Figure 9a).
2. A system compatible paste epoxy was used to fill surface voids (Figure 9b). After epoxy set, the sharp edges were sanded with 60 grit sandpaper.
3. Primer epoxy was trowel applied to concrete surface. This primer typically has a higher viscosity than that of the saturant and is used for vertical or overhead applications where additional tack is needed.
4. Plastic sheeting was placed on a large work surface. Fabric was cut and saturated with epoxy on the plastic sheeting. Epoxy was worked into fabric with a roller. The saturated fabric was then rolled onto a short length of PVC pipe.
5. While the primer was still tacky, the saturated fabric was unrolled onto the primed surface.
6. A squeegee was then used to smooth the surface and remove air bubbles.

Figure 10 shows the finished CFRP repair. The CFRP installation for girder A1 was conducted by a repair contractor. The installation for girder A2 was conducted by the FDOT structures laboratory staff.

(a) (b)

(c)

Figure 9 – CFRP installation: (a) easing corners with grinder (b) patching voids (c) cutting fabric.

Figure 10 – Finished CFRP repair.

After load testing the girders, pull-off tension tests were conducted to determine the bond capacity of the repair (Figure 11). Using a hole saw, a circular cut of approximately 2-in.

diameter was made through the CFRP and into the concrete. A disk was adhered to the circular section of CFRP formed by the cut. After the adhesive had cured, the disk was pulled in direct tension until failure. A valid test is one in which either the concrete fails (cohesive) or the CFRP repair pulls off the surface (adhesive). Tests in which the adhesive bonding the disk to the surface of the CFRP failed were considered invalid. For girder A1, the tensile capacity was 380 psi based on three valid results out of five tests. For girder A2, the tensile capacity was 425 psi based on five valid tests out of five.

Figure 11 – Pull-off test locations.

4.7 Test Setup and Procedures

Both ends of both girders were tested using a three point loading scheme with the intention of causing shear failure. The load was transferred from the actuator to the deck through a 1.5-in. thick x 10-in. x 20-in. (20-in. dimension perpendicular to the length of the girder) reinforced neoprene bearing pad at a loading rate of 0.25 kips/second.

Linear Variable Displacement Transducers, LVDTs, were used to measure displacements. Displacements were measured at each of the supports and at the load point. The actual displacement was determined by subtracting the support settlement from the displacements measured at the load point.

Each end of the girder was supported on a 1.5-in. thick x 9-in. x 24-in. (24-in. dimension perpendicular to the length of the girder) reinforced neoprene bearing pad. A load cell was used to measure load applied by the actuator (See Figure 12). Two different load points were used, one at 7 ft 2 in. and the other at 15 ft. Table 4 and Figure 12 give specific distances for the loading schemes.

LVDTs were also placed at the ends of the strands to measure strand slip. Figure 13 shows the strands that were instrumented.

Strain gages were placed on the stirrups based upon points of intersection of an assumed crack at an angle of 35^{o} originating at the support. Six 6-mm gages were adhered to the bars at each end of the girders for a total of 24 strain gages. Figure 5 indicates the location of the strain gages on the stirrups.

Sixty mm strain gages were used to measure strain in both single and rosette arrangements. Gage and rosette layouts for tests A2U1 and A2S1 are shown in Figure 14 and Figure 15, respectively. Gage and rosette for test A2U3 and A2S3 are shown in Figure 16 and Figure 17, respectively. Strain gages were installed on stirrups at each end of each beam as shown in Figure 18.

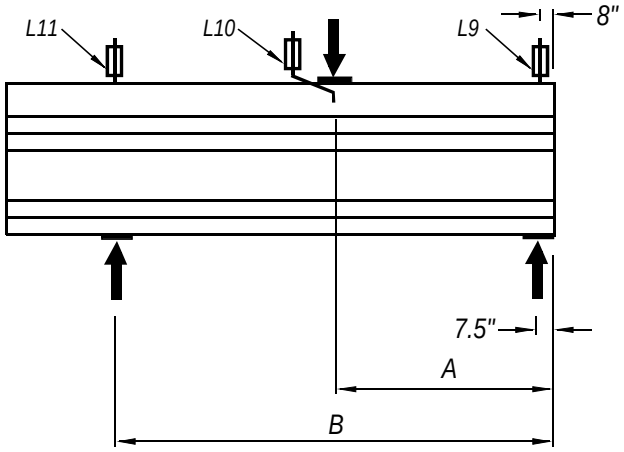

Figure 12 – Shear test setup and instrumentation.

Table 4 – Test setup geometry.

Test-Girder	A	B
A2U1	7'–2"	45 –0"
A2S1	7'-2"	45'-0"
A1U3	15'-0"	45'-0"
A1S3	15'-0"	45'-0"

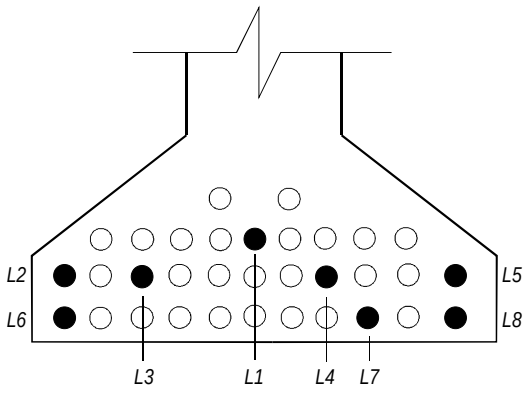

Figure 13 – Strands instrumented with LVDT's. Solid circles indicate instrumented strands

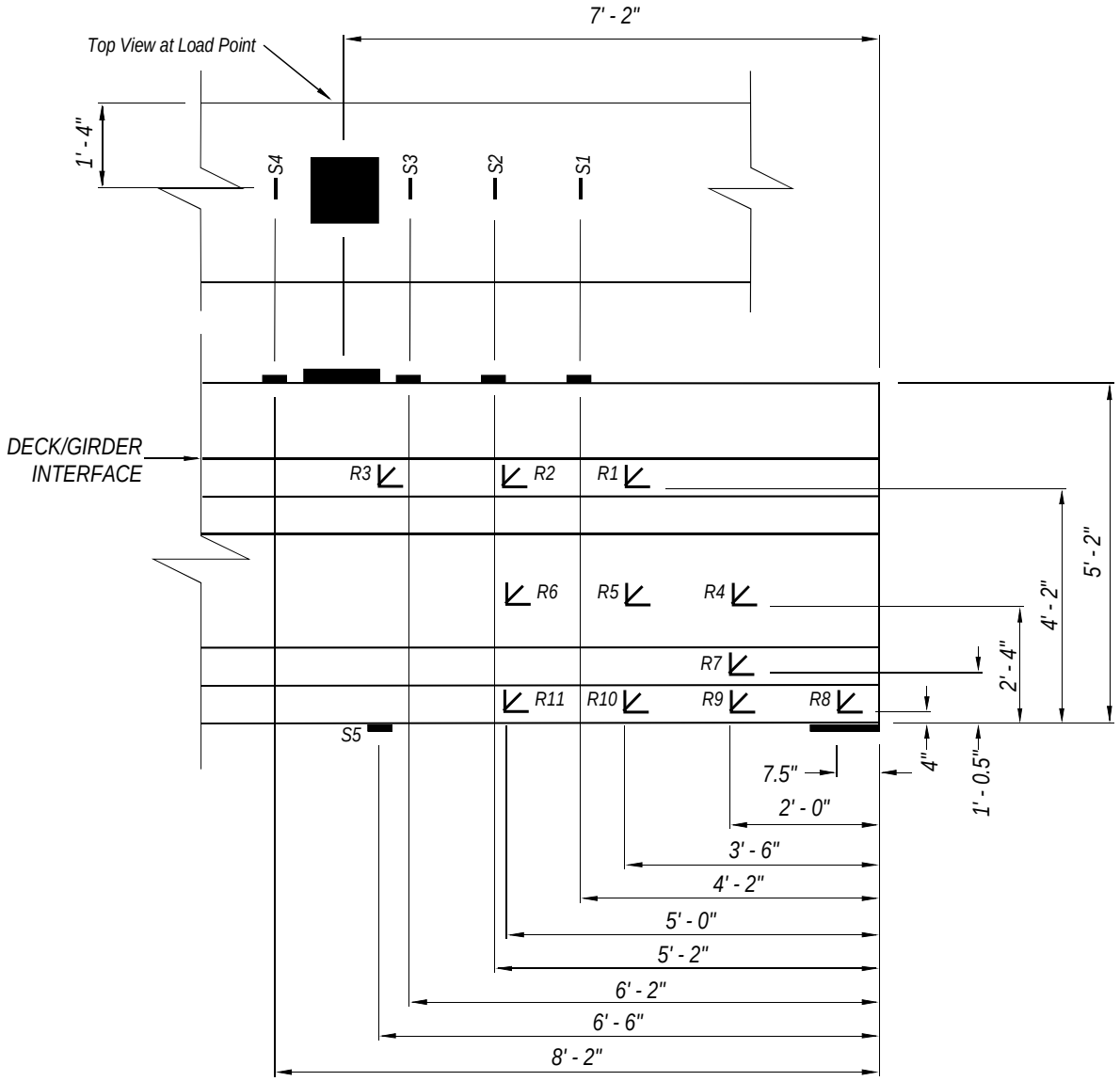

Figure 14 – A2U1 strain gage placement.

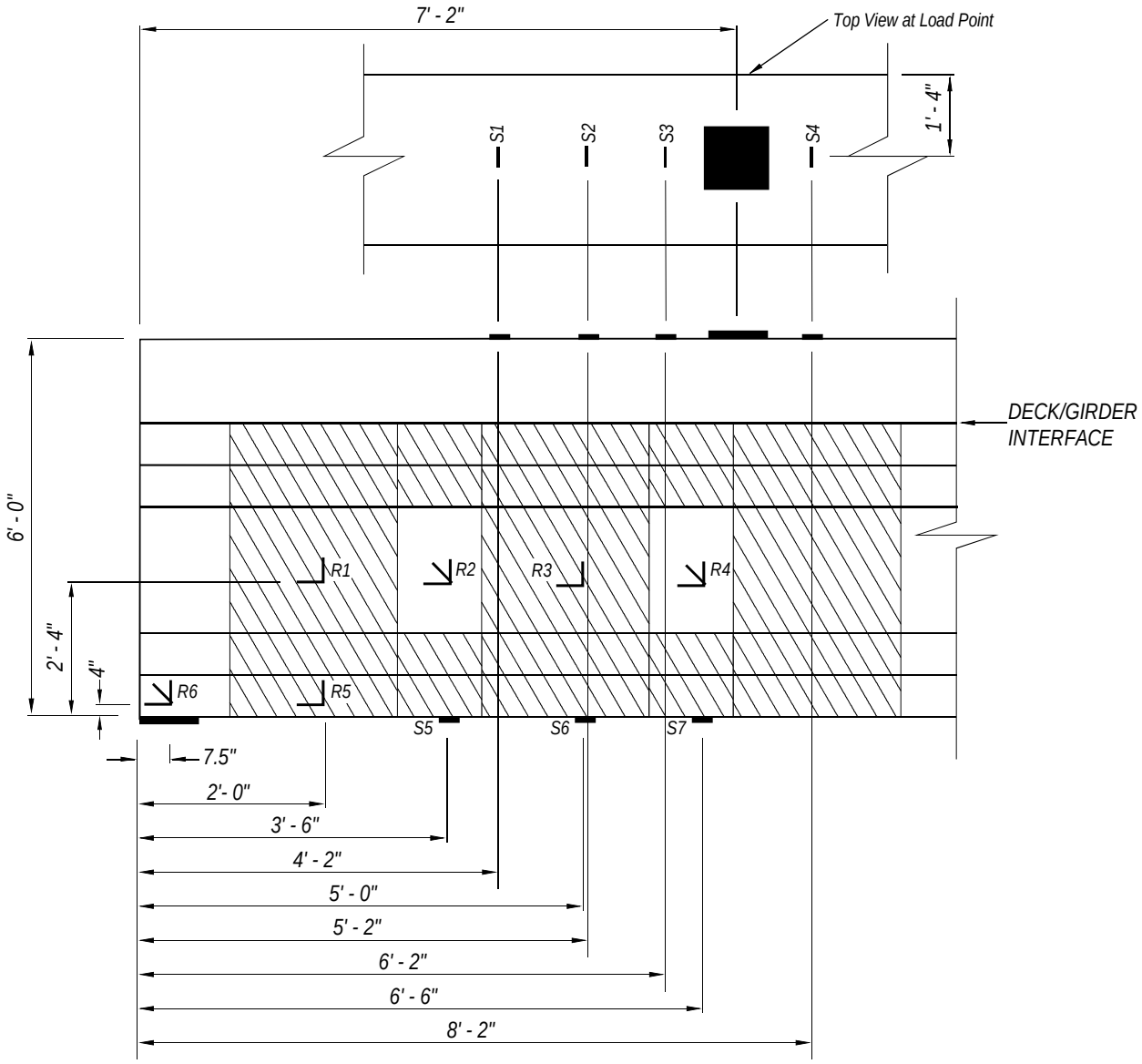

Figure 15 – A2S1 strain gage setup.

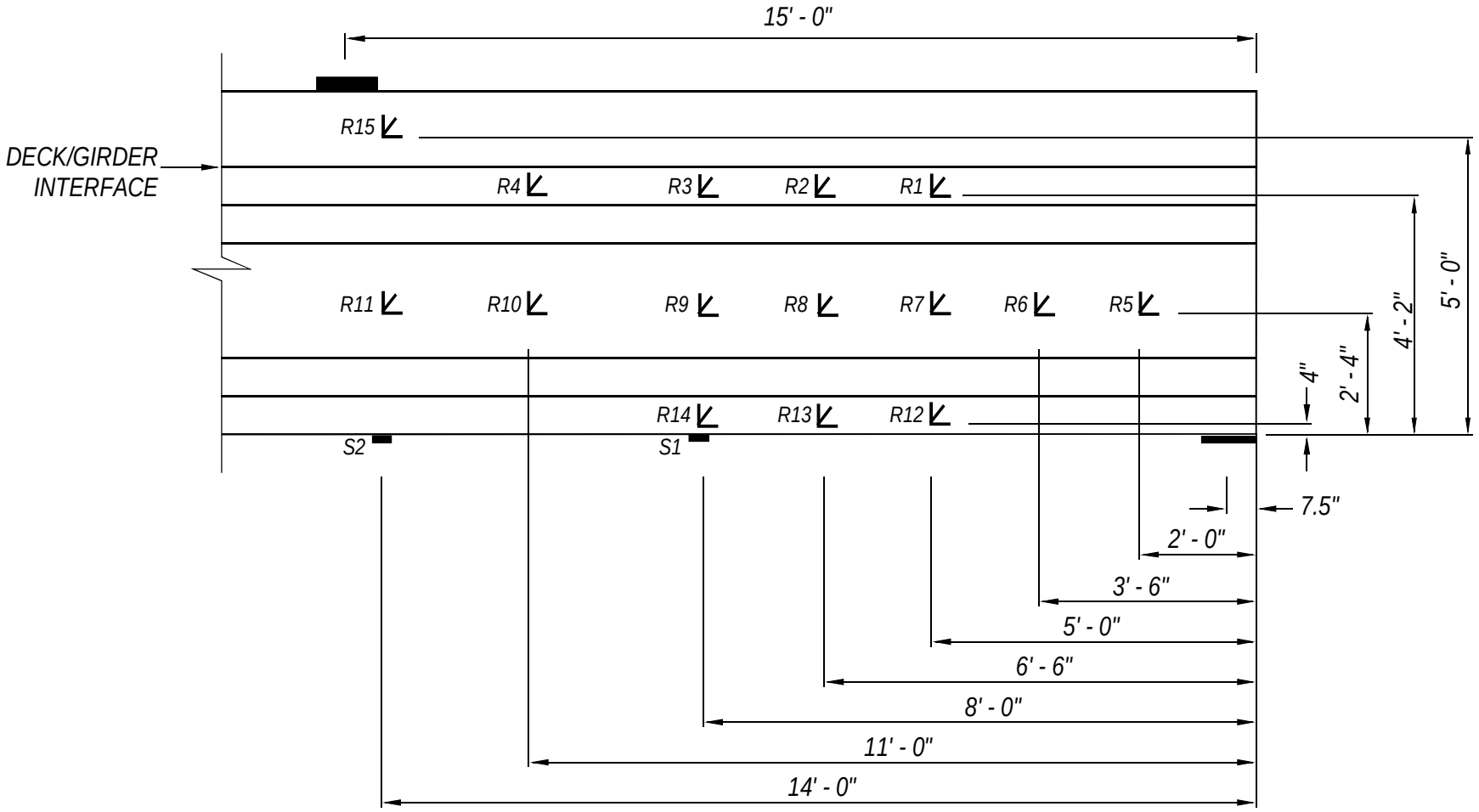

Figure 16 – A1U3 strain gage setup.

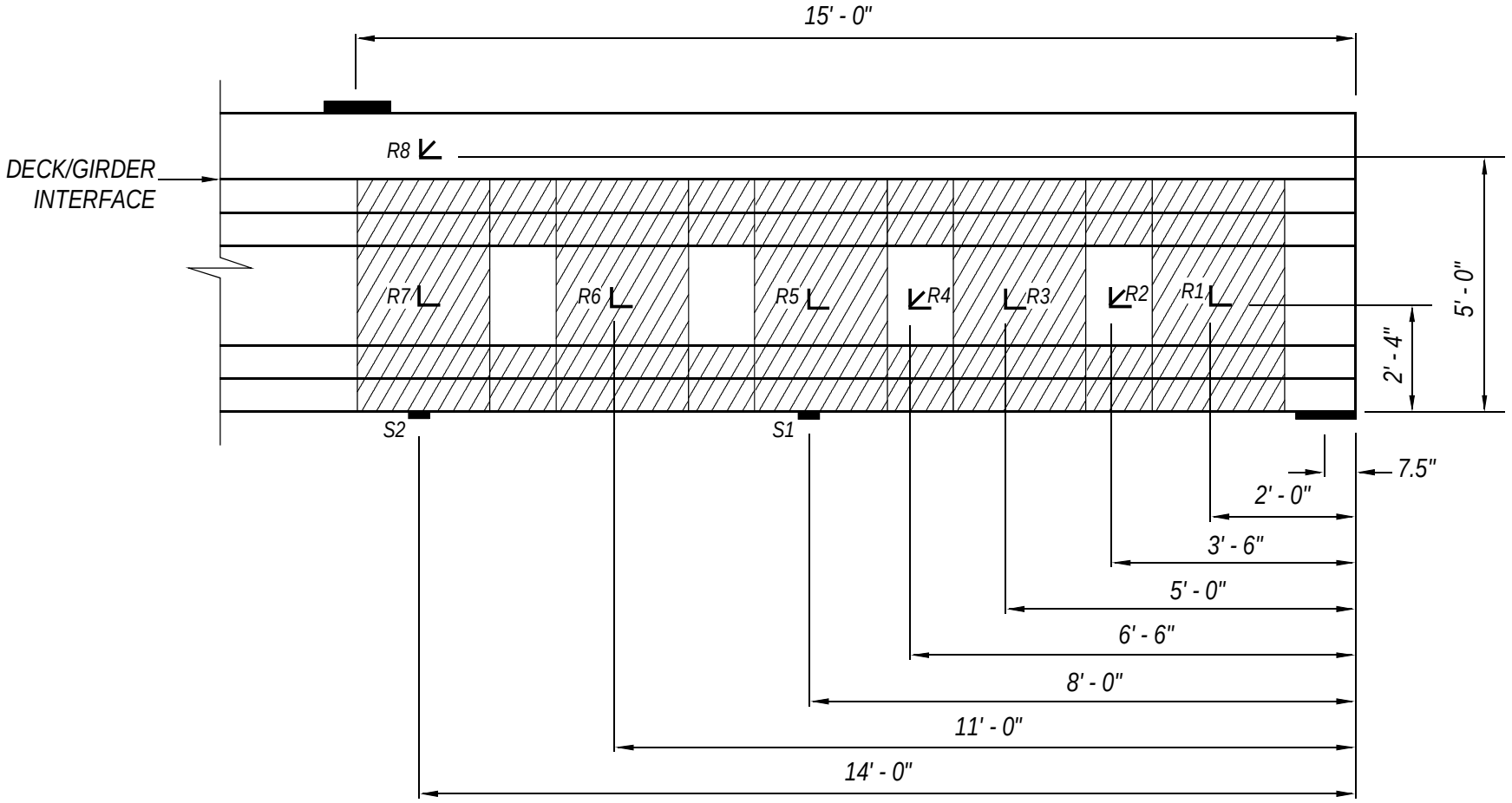

Figure 17 – A1S3 strain gage setup.

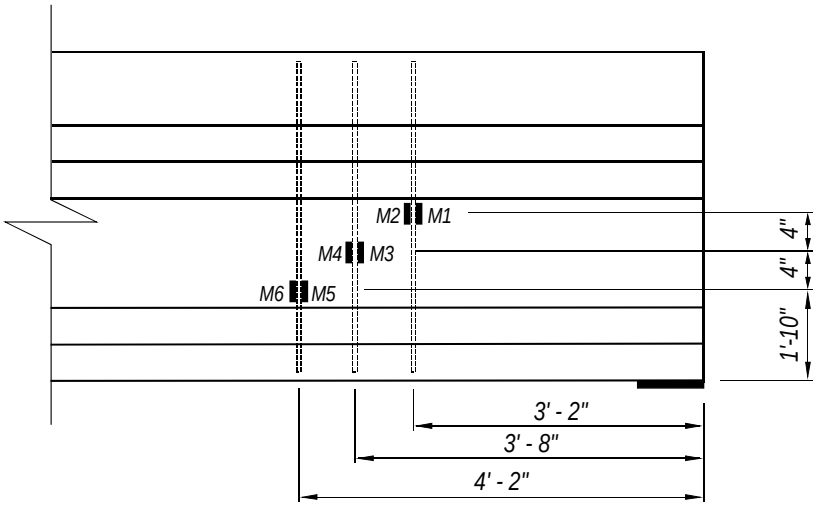

Figure 18 – Stirrup strain gages for girders A1 and A2.

4.8 RESULTS AND DISCUSSION

The superimposed shear vs. displacement curves for A1U3 and A1S3 are shown in Figure 19. The superimposed shear is the shear force at the support nearest the loading point and does not include the self-weight of the girder. The displacement was measured at the load point.

Both the control (A1U3) and CFRP strengthened (A1S3) girders behaved linear-elastically up to first cracking. A1U3 cracked initially at a shear of 165 kips, while A1S3 cracked at a shear of 205 kips, a 24% increase. Cracking shears were confirmed by strain rosette readings shown in Figure 20. It is interesting to note that neither the precracked nor post-cracked stiffness of the strengthened girder is markedly greater than that of the unstrengthened girder.

The unstrengthened girder (A1U3) reached a maximum shear of 256 kips, whereas the strengthened girder (A1S3) reached a maximum shear of 310 kips, a 10% increase. Thus, the FRP repair provided an increase in capacity but not stiffness for the a/d of 3 condition.

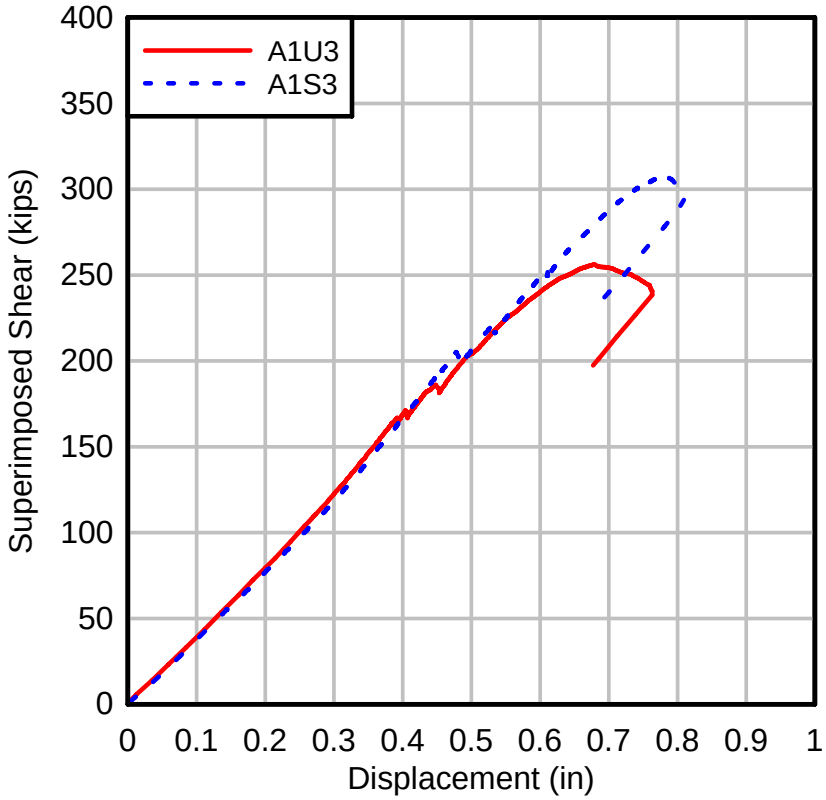

Figure 19 – A1U3 and A1S3 load vs. displacement.

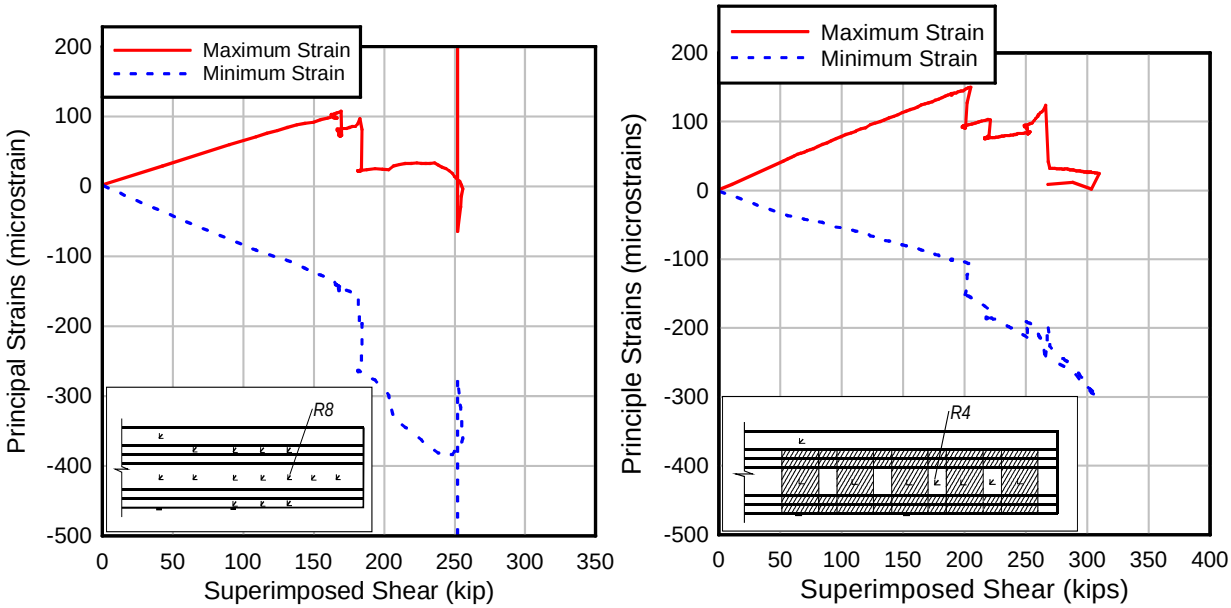

(a) (b)

Figure 20 – Principal strains from rosettes: (a) A1U3R8 and (b) A1S3R4. (Tension is positive)

The initial crack patterns for A1U3 and A1S3 are shown in Figure 21. The cracks in both girders formed at angle of approximately 30 degrees from horizontal. The distribution of additional cracks varied between the control and strengthened specimens. The strengthened specimen had a crack distribution that was evenly spread between the load point and the support, while the control specimens crack pattern spread only halfway from the support to the load. This indicates that the post-cracking behavior was influenced by the CFRP bonded reinforcement.

Examination of the cracking pattern reveals that the failure was not symptomatic of what is typically considered a shear failure. Cracks did not extend into the compression zone, nor did a compression failure occur in the top of the girder. Rather, the cracks extended into the bottom flange of the girders near the support (Figure 22).

The early failure of the girder was attributed to two characteristics of the girder design. One was the irregular debonding pattern that placed fully bonded strands in the flanges of the bottom bulb and debonded strands under the web (Figure 4). The other was the lack of confinement steel in the bottom bulb near the support. Figure 23a illustrates the flow of forces as capacity is imminent in a girder with all strands fully bonded. The strut and tie model shows a diagonal strut and a longitudinal tie that are typical of a girder with a short shear span. The strut passes through the web and terminates under the load point at one end and at a node just over the support at the other end. The tendon forms the tie, which must be anchored into the node over the support point to ensure equilibrium. The typical mode of behavior for this configuration is for the strand to slip. This typically occurs when the load point is very near the support, which results in a short strand development length.

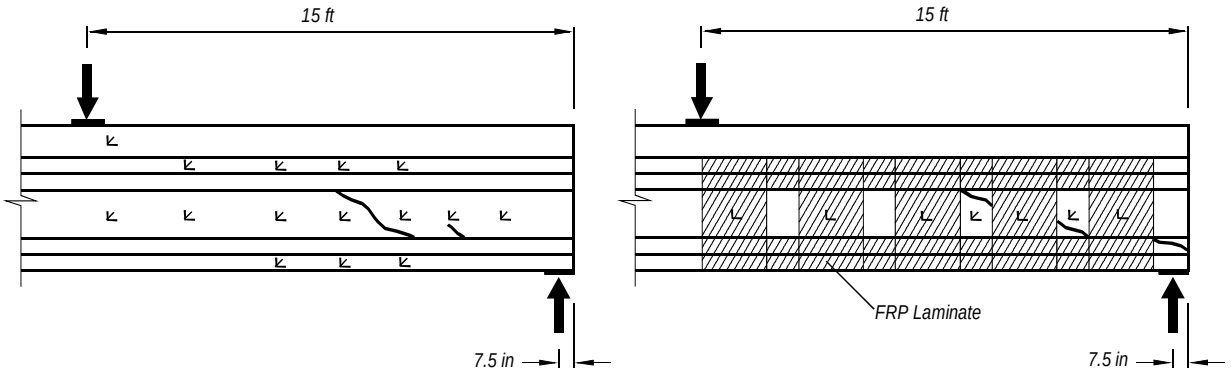

(a) (b)

Figure 21 – First crack pattern for load location a/d = 3 (a) A1U3 and (b) A1S3.

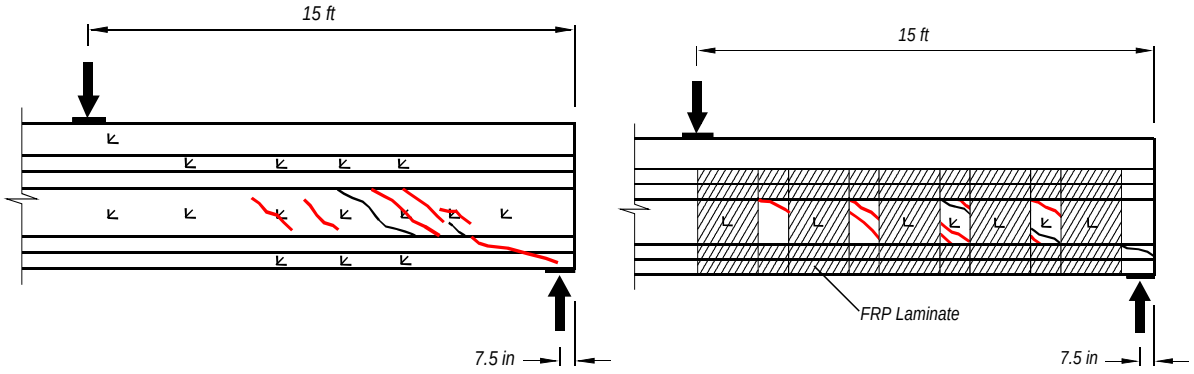

(a) (b)

Figure 22 – Final crack pattern for load location a/d = 3 (a) A1U3 and (b) A1S3.

In these test girders, only the strands in the outside portion of the flange were bonded near the support, and thus able to act as ties as shown in Figure 23b. This resulted in a disruption of the node at the support point. Because of the offset between the strut in the web and the two ties in each flange of the bull (fully bonded strands), secondary struts formed to transfer the load laterally to the nodes at the ties. Additional secondary struts were essential between the support and the nodes at the ties to complete the load path to the support. Both pairs of secondary struts induced horizontal components that acted transverse to the beam. A tension tie is shown between the flange nodes in the illustration. The test beam, however, lacked transverse reinforcement that might have held the bulb together after cracking.

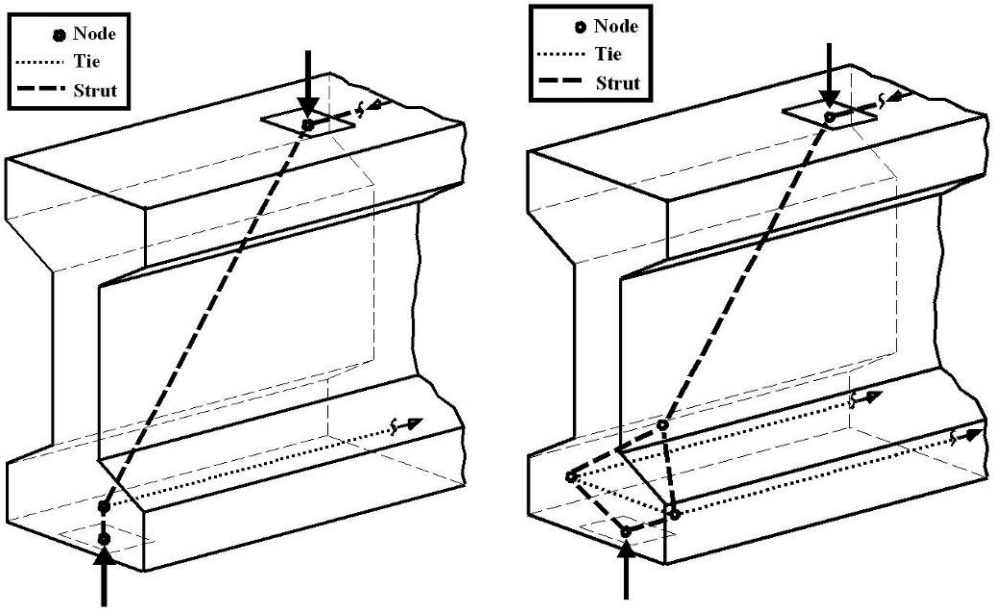

(a) (b)

Figure 23 – Strut and tie model for tendon with (a) fully bonded strands and (b) an excessive number of strands debonded under the web.

Figure 24 shows the cracking pattern exhibited by girder A2U1 after reaching capacity. The girder capacity was controlled by the formation of a large crack at the outer pair of strands in the bulb flange. It is believed that this crack formed as a result of the transverse tensile stresses in the concrete resulting from the splitting of the strut shown in Figure 22b. The crack formed at the edge of the bearing pad. As the crack progressed along the beam it angled toward the web and terminated at the web at a distance of approximately half the girder depth. This crack caused a loss of the tie from the outside node, thus resulting in the strand peeling away from the bulb as indicated by the arrow. This behavior may have caused problems with strand slip measurements, since the frame supporting the displacement devices was attached to the bulbs (Figure 25).

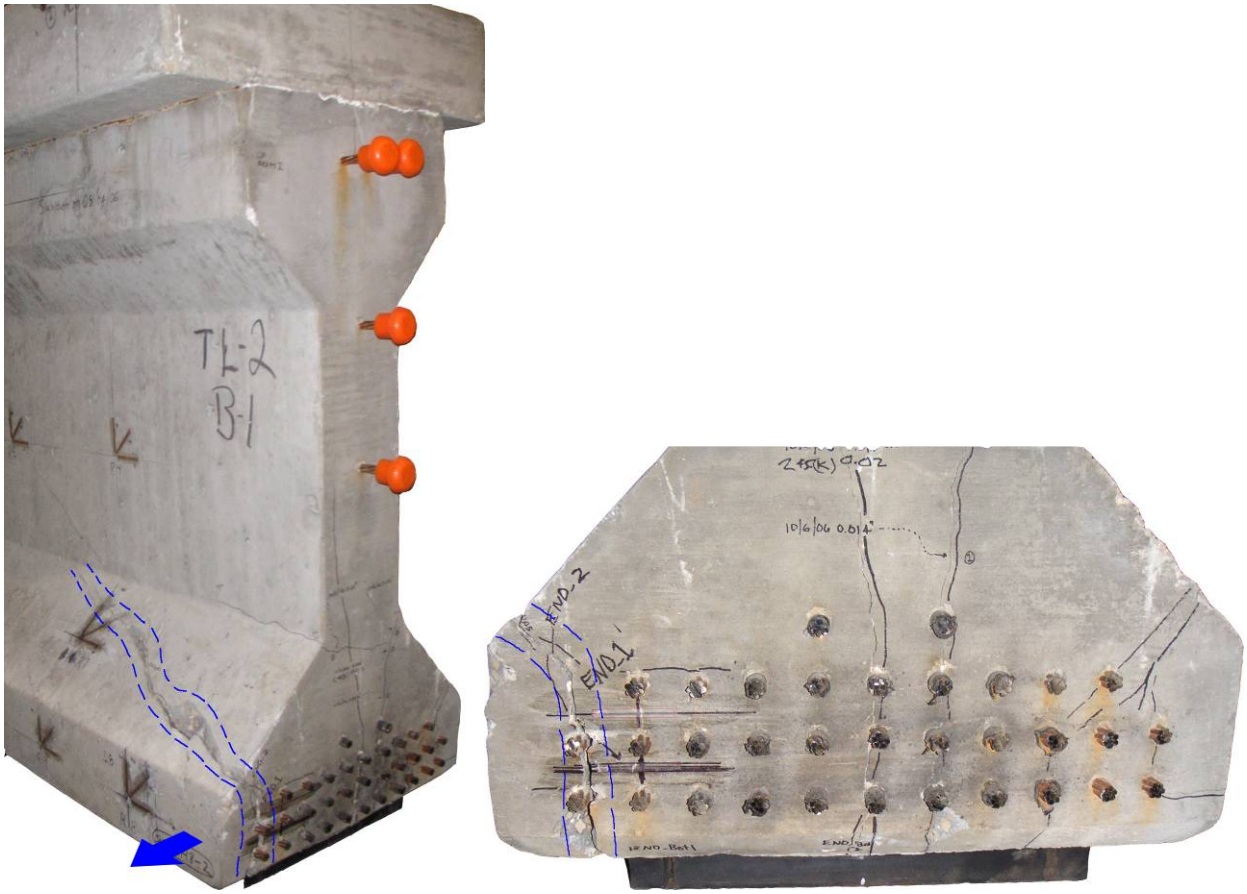

Figure 24 – Bulb cracking pattern caused by excessive debonding under the web.

Figure 25 – Cracking at support and strand instrumentation.

Figure 26 shows the displacement of strands 2 and 6. A1U3L6 reports negative movement at strand 6, likely due to movement of the frame holding the LVDT (Figure 25). The greatest strand movement occurred just prior to reaching girder capacity. This movement is attributed to a combination of strand slip and bulb flange separation.

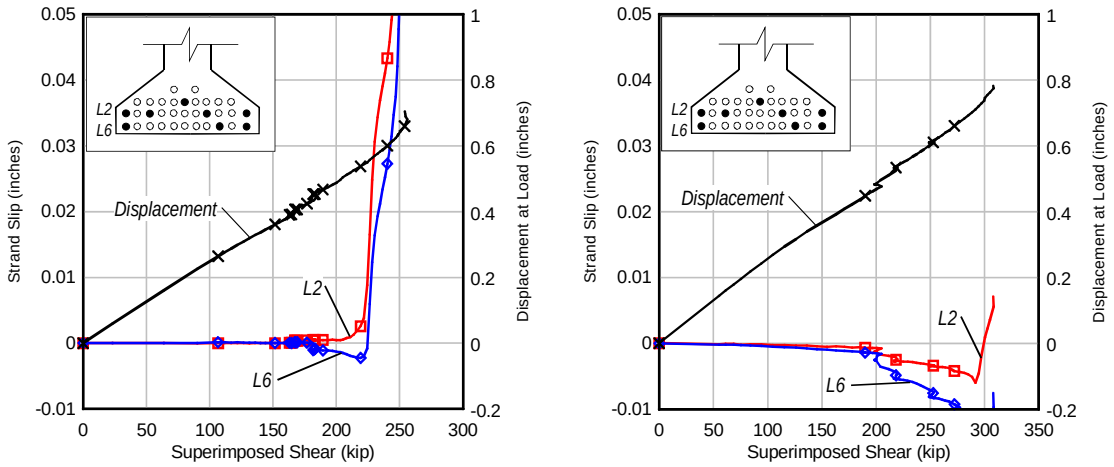

(a) (b)

Figure 26 – Strand slip and girder displacement for (a) A1U3 and (b) A1S3.

The second beam (A2) was tested using a/d = 1. Figure 27 shows the superimposed shear vs. displacement curves for A2U1 and A2S1. Test A2U1 shows a constant stiffness until a shear of 205 kips where the girder first cracked. The first crack for A2S1 appears to have occurred at a shear of 228 kips. Cracking loads were confirmed by strain rosette readings shown in Figure 28. The control girder, A2U1, reached a peak load of 296 kips while the strengthened specimen, A2S1, reached a peak load of 324 kips.

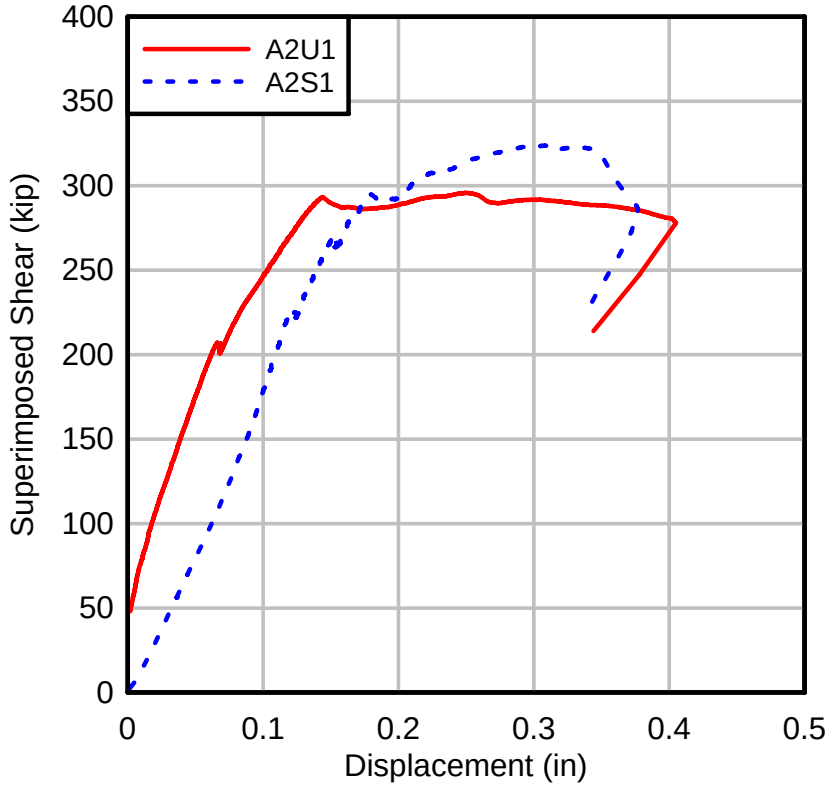

Figure 27 – A2U1 and A2S1 load vs. displacement.

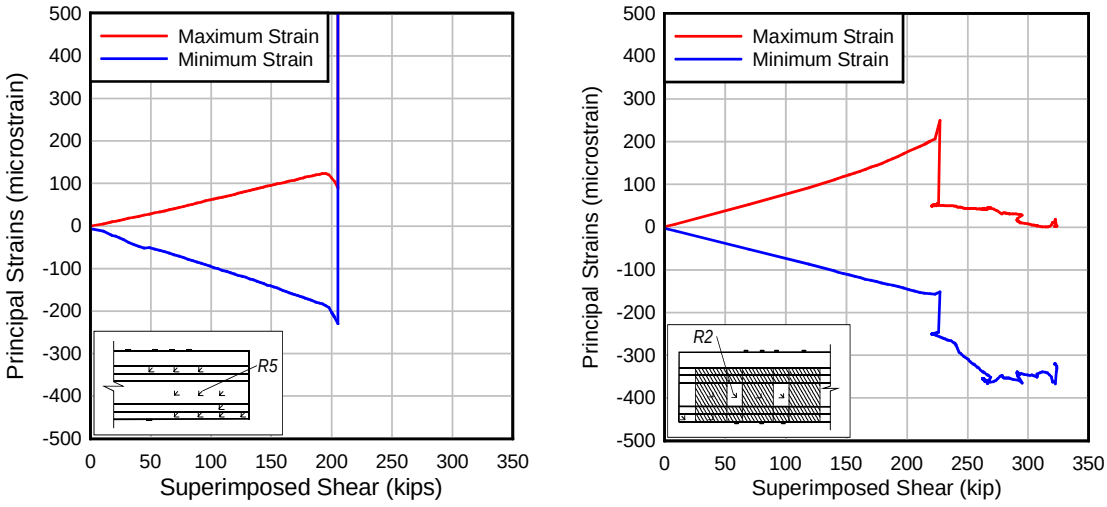

(a) (b)

Figure 28 – Strain rosettes (a) A2U1R5 and (b) A2S1R2.

Figure 29 shows the locations of the initial cracks for A2U1 and A2S1. For both tests, the initial crack occurred at the same location and at similar angles. The CFRP did not influence the cracking pattern, as the final cracks are also similar for both tests (Figure 30). The CFRP strengthening scheme provided an increase in cracking load of 23 kips, a 10 percent increase. The peak load for A2U1 was 296 kips while A2S1 reached a peak load of 324 kips. The FRP provided a 9 percent increase in capacity

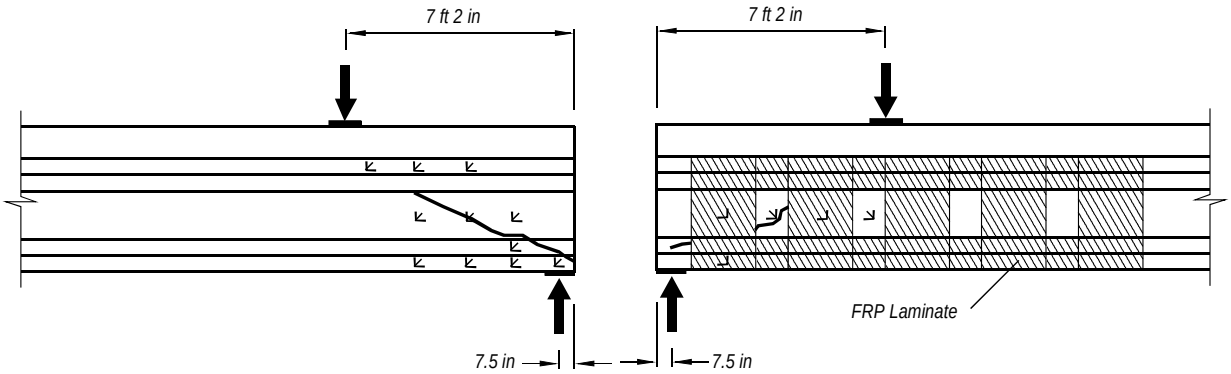

Figure 29 – First crack pattern for load location a/d = 1 (a) A2U1 and (b) A2S1.

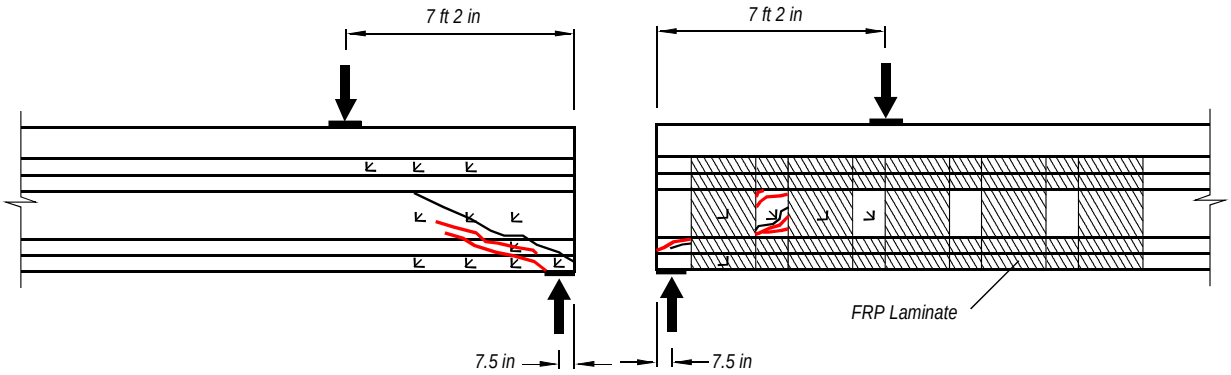

Figure 30 – Final crack pattern for load location a/d = 1 (a) A2U1 and (b) A2S1.

The failure mode for pretensioned girders with such a short a/d ratio is typically strand slip. Similar to the tests conducted with the point load at 15 ft, however, the failure mode for this loading condition was also influenced by excessive number of strands debonded in the web as well as the lack of confinement steel in the bottom bulb. After cracks penetrated the bottom

bulb, the bulb flange cracked and separated from the web. The lack of confinement steel allowed this transverse movement to occur after the bulb flange had cracked. Cracking in the bottom bulb also led to slipping of the strands (Figure 31).

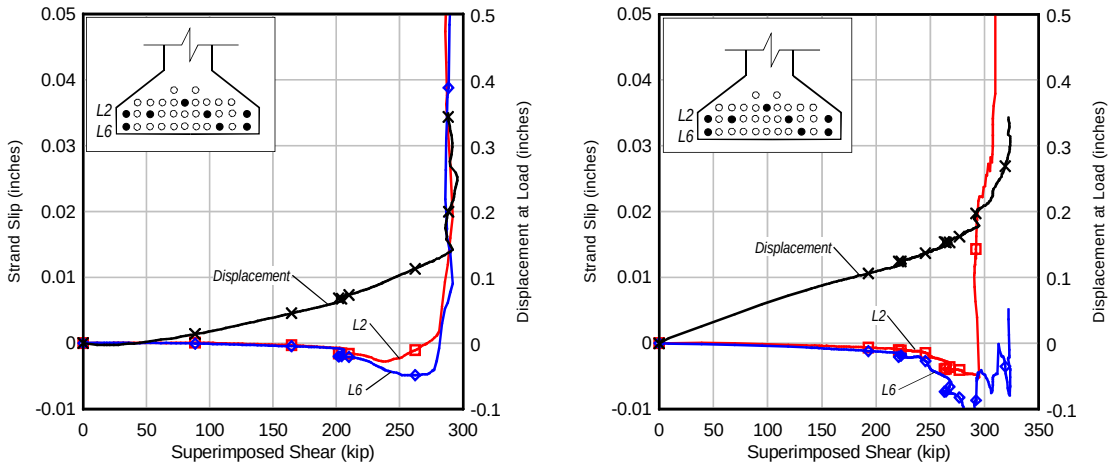

Figure 31 – Strand slip and load displacement for (a) A2U1 and (b) A2S1

Table 5 summarizes the capacities of both the strengthened and control tests of the Type IV girders. In both loading conditions CFRP provided some increase in capacity but was most effective for the a/d = 3, which is typically where shear capacity (as opposed to strut and tie) behavior will control the beam capacity. Some of the increase in capacity was likely due to the confinement of the bottom bulb by the CFRP wrap closest to the support. In addition, the change in cracking pattern caused by the a/d=3 tests indicate that there was some effect from the CFRP wraps bonded to the webs. This is supported by the larger increase in capacity for the a/d=3 test over that of a/d =1 and may indicate that the vertical strips of CFRP are contributing modestly to the overall girder capacity. The control girder was damaged slightly at the end used to conduct the a/d = 3 test. This damage may have reduced the capacity of the control girder, which may explain why the improvement for the a/d=3 test is greater than the a/d=1 test.

Table 5 – Ultimate shear capacity.

a/d	$V_{control}$ (kip)	V_{CFRP} (kip)	$V_{CFRP}/V_{control}$
1	296	324	1.09
3	256	310	1.21

4.9 CALCULATED SHEAR CAPACITY

Table 6 shows a comparison of the experimental girder capacity with calculated capacities using the following methods:

1. Modified compression field theory (MCFT) from AASHTO LRFD Bridge Design Specification (2007).
2. Strut and Tie method (STM) from AASHTO LRFD Bridge Design Specification (2007).
3. Detailed method (ACI) from American Concrete Institute ACI 318 (2008)

The failure modes assumed by these methods do not match those observed in the tests. The comparison, however, gives perspective regarding the predicted vs. actual capacities. The experimental data presented in earlier sections was typically the superimposed shear and does not include the self-weight of the girder. The self-weight was added to the experimental results to reflect the total shear applied to the girder at capacity for the purpose of comparing to the calculated capacities. The following material properties were used to calculate the shear capacity: compressive strength of concrete of 7.2 ksi, yield strength of the shear reinforcement of 60 ksi, and tensile strength of the prestressing steel of 270 ksi.

Table 6 – Comparison of experimental capacity with calculated shear capacity.

a/d	V_{EXP} (kip)	MCFT		STM		ACI	
		V_n (kip)	V_{EXP}/V_n	V_n (kip)	V_{EXP}/V_n	V_n (kip)	V_{EXP}/V_n
1	319	335	0.95	153	0.48	337	0.95
3	272	263	1.03	---	---	349	0.78

For the STM, only the fully bonded strands in the bottom bulb, and lowest layer of mild steel were considered as part of the tie. The force in the tie was limited by the lack of development length, and thus was the controlling factor for the STM prediction. The strut and tie method was not used for a/d of 3 because it is not typically applicable for this load configuration.

It is important to note that the failure mode of the girder did not match that assumed by either the ACI or MCFT methods. Because the failure mode was separation of the bottom bulb flange, the peak shear load was less than that predicted by the sectional shear models.

Due to the strand debonding pattern, the effective prestress force was greater for the section at a/d of 3 than for the section at a/d of 1. For the ACI method, the web cracking equation is a function of the prestress force. As the web cracking equation controlled the ACI predicted capacity, the predicted shear capacity is greater for the longer shear span.

4.10 Summary and Conclusions

Two girders were constructed to replicate existing, in-service, Type IV bridge girders. The existing girders were strengthened using CFRP fabric to mitigate the effects of a problematic debonding pattern, in which fully bonded strands were placed at the edges of the bottom bulb. One end of each test girder was strengthened using the same CFRP strengthening scheme as was used on the in-service girders. Each end of each test girder was loaded to failure in three-point bending. One girder was tested using and a/d of 1, the other was tested using an a/d of 3. The experimental capacity of the strengthened ends was compared to the experimental capacity of the unstrengthened ends. Current design methods were compared to the experimental results. Following are the salient findings from the research:

1. The bonded CFRP reinforcement provided an increase in capacity of 9 and 21 percent for the 7 ft 2in. and 15 ft shear spans, respectively.
2. The CFRP reinforcement improved the distribution of cracking for the test at an a/d ratio of 3.
3. Capacity was not controlled by the typical shear failure mechanisms, but rather was due to the cracking and separation of the bottom bulb flange of the girder. This was a result of the unusual debonding pattern that placed the fully bond strands out in the bulb and the

debonded strands under the web. It is likely that the presence of confinement steel around the strands would have resisted this separation. It is not clear, however, if the strand slip would have still restricted the capacity of the girder if confinement steel were provided.

4. The improvement in capacity of the strengthened girders was likely due, in part, to partial confinement of the bottom bulb by the bonded CFRP reinforcement.
5. The observed failure mode did not match those assumed by any of the three models (ACI, S&T, MCFT).

5 AASHTO TYPE III GIRDERS

5.1 OBJECTIVES

Salvaged AASHTO Type III bridge girders that were in service for nearly 30 years were tested to evaluate behavior, capacity, and failure mode under varying a/d ratios. Development of strand was of particular interest for girders tested using smaller a/d (shear span) ratios, while mode of failure was of particular interest for girders tested using larger a/d ratios. In addition, the behavior of the precast deck system used with the girders was evaluated.

5.2 APPROACH

Four AASHTO Type III girders were salvaged and tested. Girders were tested in three-point bending. The a/d ratio ranged from 1.2 to 5.4 (Table 9). Where possible, each end of each girder was tested.

5.3 BACKGROUND

Fagundo and Lybas (1995) conducted sixteen tests on concrete girders with varying load points and spans. They found that the formation of diagonal cracks always preceded longitudinal strand slip. They also found that cracks forming directly under the load point would create a hinge effect cause the beam to act as two rigid bodies. This behavior is typical with under-reinforced beams.

Russell and Ramirez (2007) performed tests on the ends of 43 rectangular beams and 8 I-shaped beams. Loading geometry was varied to test different development lengths. Bond, shear and flexural failure modes were observed and a criterion was set to classify them. Bond failure was classified as excessive strand slip. Strand slipping occurred after the formation of flexural cracks. Shear failure was classified as sudden diagonal compression failure in the web. Flexural failure was classified as crushing of the compression zone.

Ramirez (1994) presents a full member strut-tie design of a precast pretensioned beam with depressed strands at midspan. He compares his results with the ACI code, which uses a sectional approach. At the time the article was presented there were no requirements considering the interaction of adjacent strands. A strut and tie model is presented which shows the detailing needed to prevent splitting. A strut and tie model of the forces in the compression flange is also

presented. Proper detailing of the web flange connection is necessary to insure that cracking does not occur. This could leave the flange ineffective in resisting longitudinal stresses.

Alshegeir and Ramirez (1992) performed testing of 3 full scale pretensioned AASHTO type I and II beams. Analysis of the tests led to the following conclusions. The use of higher strength concrete would improve ultimate capacities by strengthening the nodes and the struts. The size of the bearing plates at the load and support determine the dimensions of the nodal zones at those locations. Stresses in the nodal zone are a function of the size of the nodal zone. Because all of the elements near the load and support are in compression, the nodes at these locations can be modeled using the full uniaxial compressive strength of concrete. A reduced uniaxial compressive strength should be used when tension ties are present in the node.

5.4 GIRDER ACQUISITION AND CONDITION

Girders were salvaged from an I-75 overpass bridge on State Road 93 in Sarasota County, Florida. The bridge was built in 1979 and was made up of five AASHTO Type III prestressed concrete bridge girders, four of which were salvaged. The overpass had twin spans identified by FDOT bridge numbers 170079 or 170080. The bridge deck was saw-cut along the length of each girder to facilitate removal (Figure 32). The deck was carefully removed using a saw rather than the typical jack hammering and prying. This ensured that the girders were undamaged during removal. After removal, the girders were transported by truck to the FDOT Structures laboratory in Tallahassee, Florida (Figure 33). The rigging caused damage to the deck during lifting but was considered minor and did not appear to affect the results of the testing.

The latest inspection of the bridge was completed in February 2007. The overall ratings for the bridge deck and superstructure were very good. The bare concrete deck was described to "have a few repaired areas, there are few spalls/delaminations in the deck surface or underside and the only cracking is superficial or surface map cracking." The girders were found to have little or no visible deterioration, but did have minor cracking and some discoloration due to efflorescence. The report indicated that the cracking was not anticipated to affect strength or serviceability.

Figure 32 – Deck cutting operation in preparation for girder removal.

Figure 33 – Removal of Type III girders.

5.5 GIRDER DETAILS

Figure 35 shows the deck configuration and reinforcement. The figure shows average values since the deck dimensions varied slightly with location. The 7-in. thick deck was reinforced longitudinally with #7 bars. These bars were spaced at approximately 5 to 6 in. on center near the supports, but at midspan were spaced at 11 to 12 in on center. It is not known where the spacing changed along the span of the girder. The deck was cut such that 28-in. wide section remained with each girder. The deck consisted of a precast panel spanning between girders, with a cast-in-place topping. The precast section had shear keys to provide interlock between the two sections. The precast section was reinforced with 3/8-in. diameter strand,

placed transverse to the girder. The cast-in-place slab was reinforced with #5 bars spaced at approximately 5 to 6 in. on center, placed transverse to the length of the girder.

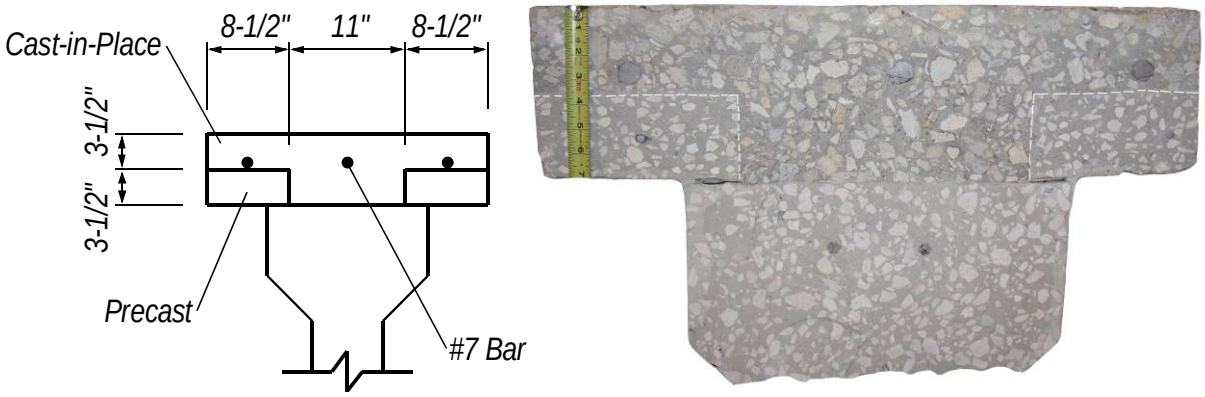

Figure 34 – Transverse deck section photograph and schematic.

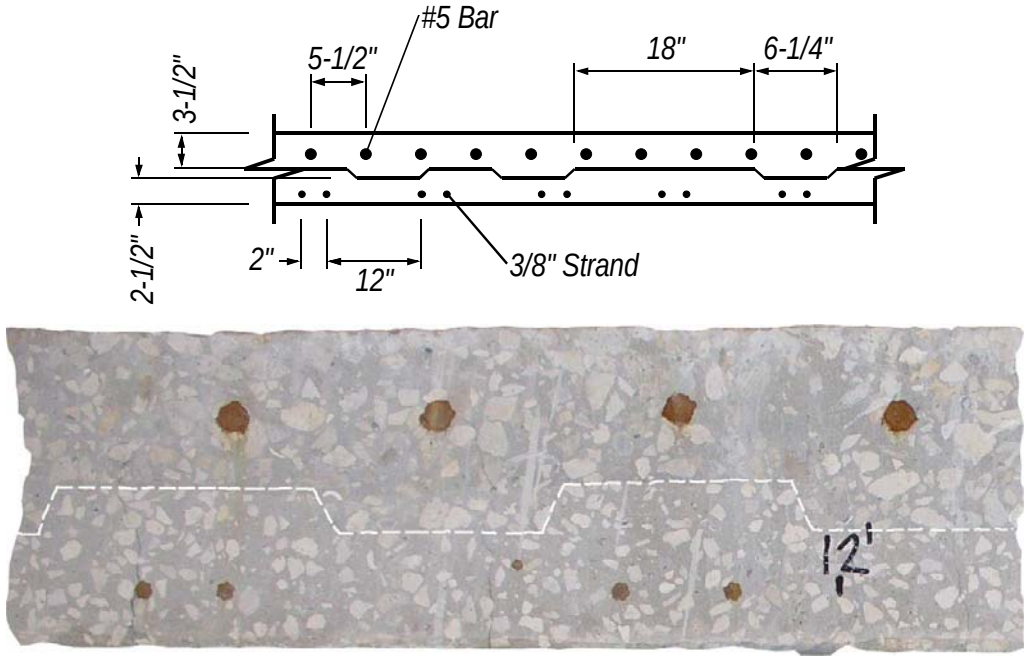

Figure 35 – Longitudinal deck section photograph and schematic.

Stirrup layout is shown in Figure 36. Twenty-four one-half inch diameter stress-relieved strands were tensioned to 28.9 kips. Six strands were draped at depression points approximately 30 ft from each end (Figure 37 and Figure 38). Ten strands were debonded at two varying lengths, 1 ft and 2 ft (Figure 39).

Samples of the concrete, stirrups and prestressing strands were taken after the girders were tested. These samples were tested to determine material properties. Cores were taken from girder B2 at mid-height of the section at approximate distances of 18, 25, and 25.5 ft from end where test B2U2 was conducted (Table 7). The deck cores were also taken from girder B2 centered in the top of the slab. These cores were taken at distances of 22, 30 and 31 ft from the end where test B2U2 was conducted (Table 8). Stirrup specimens were taken from girder B1 (Table 9), and strand specimens were taken from girder B3 (Table 10).

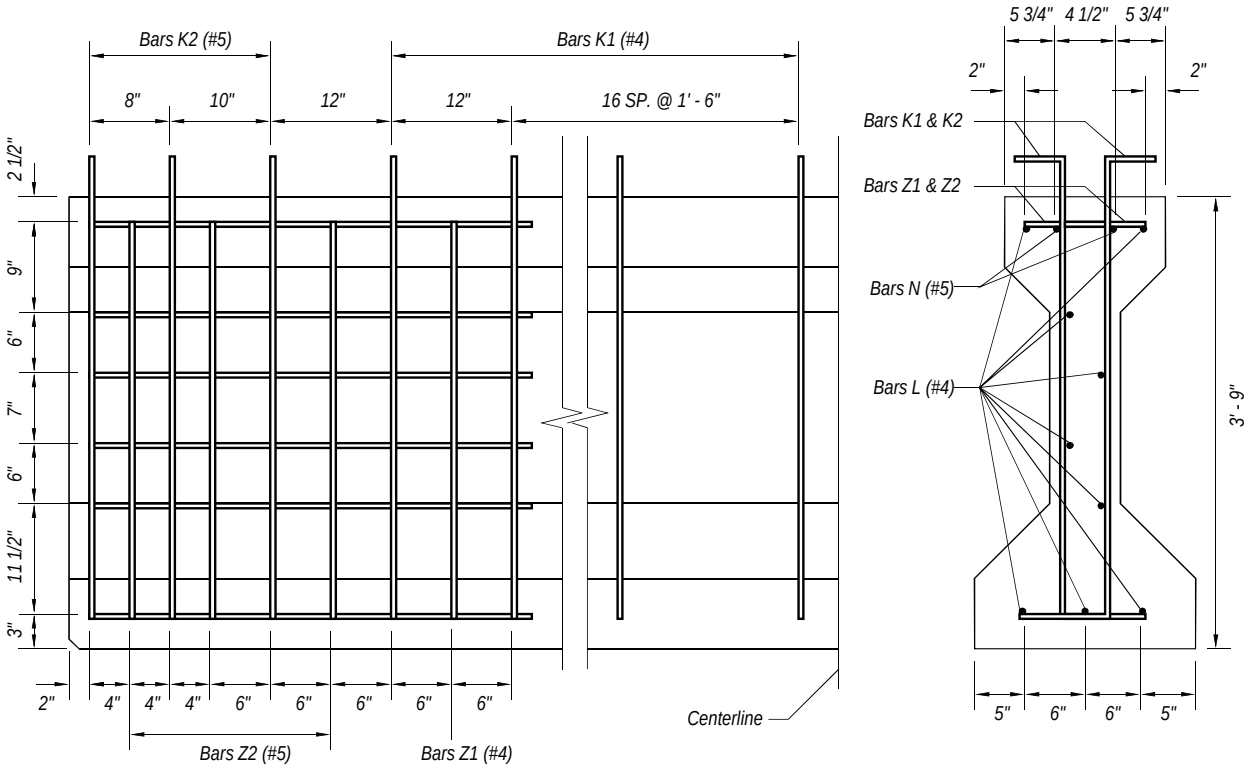

Figure 36 – Type III stirrup layout.

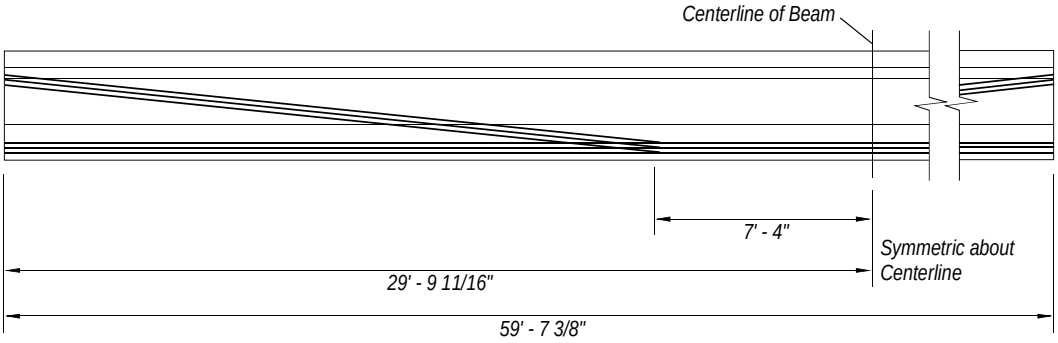

Figure 37 – Type III strand profile.

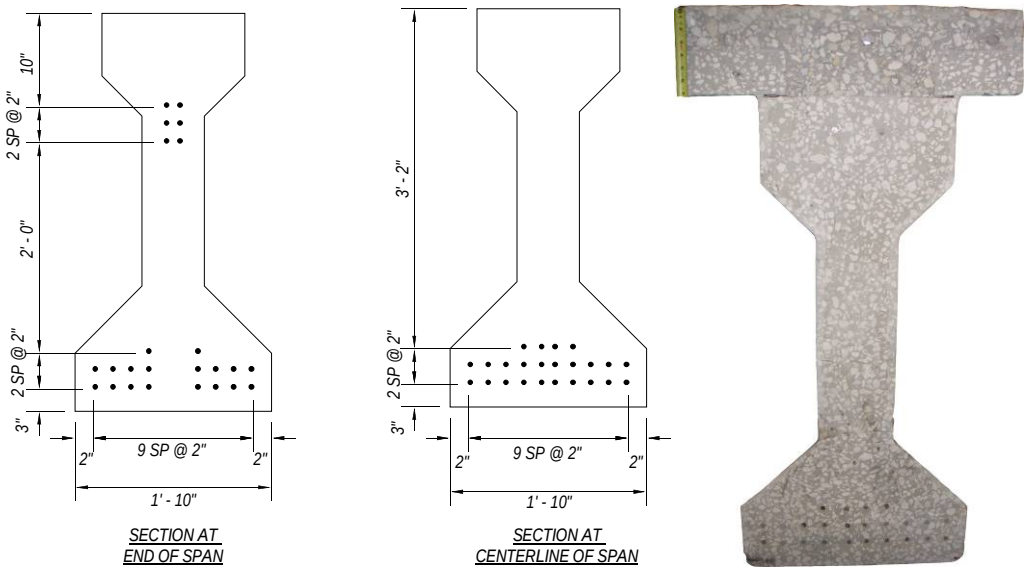

Figure 38 – Type III end and centerline cross sections.

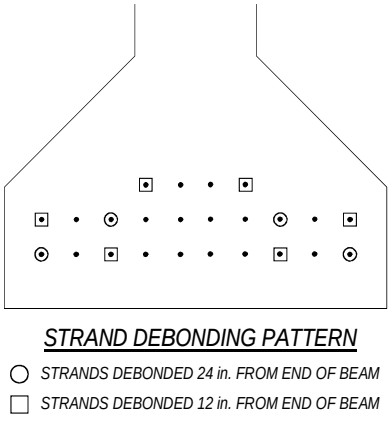

Figure 39 – Type III debonding pattern.

Table 7 – Concrete core test results for web.

Sample	Load (lbs)	Stress (psi)	Diameter (in)	Length (in)
1	45200	5690	3.18	6.08
2	44000	5540	3.18	6.12
3	45100	5670	3.18	6.14
	Average	5630		

Table 8 – Concrete core test results for deck.

Sample	Load (lbs)	Stress (psi)	Diameter (in)	Length (in)
1	38100	4830	3.17	6.09
2	36700	4650	3.17	6.13
3	42700	5410	3.17	6.20
	Average	4960		

Table 9 – Stirrup test results.

Sample	Tensile Strength (psi)	Yield Strength (psi)	Elongation (%)
1	90000	54700	14.5
2	95200	58700	11
Average	92600	56700	12.8

Table 10 – Steel strand strength and modulus.

Sample	1	2	3	4	AVG
Strength (ksi)	286	285	286	283	285
Stress at 1% EUL (ksi)	257	262	254	253	257
Total Elongation (%)	5.43	5.99	6.59	7.04	6.26

Initial tests using a short shear span ratio indicated that the primary failure mode was strand slip. B4S2 was strengthened with the intention of providing confinement at the support and preventing the strands from slipping. The confinement was provided by two 5-in. square, ¼-in. thick steel tubes that were clamped to each side of the bottom bulb (Figure 40 and Figure 41). Bearing plates were located at each end of each steel tube between the tube and the bottom bulb of the girder. The tubes were clamped using approximately 1.5-in. thick plates and two 1-in. diameter hand-tightened steel threaded rods. Tubes were instrumented with 60-mm strain gages as shown in Figure 42.

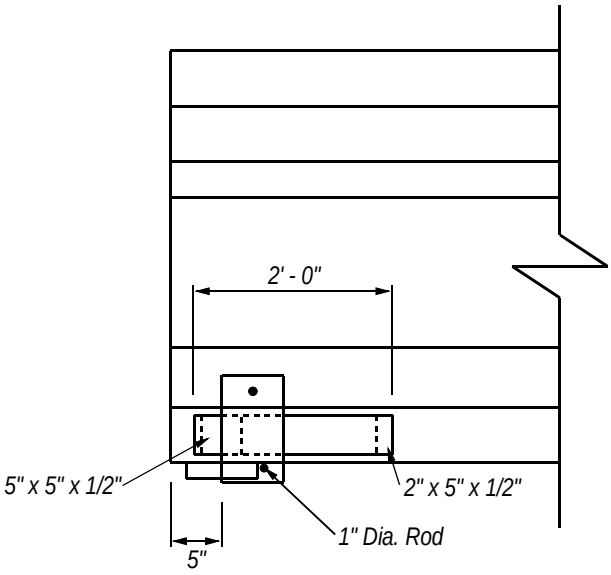

Figure 40 – B4S2 repair layout.

Figure 41 – B4S2 repair.

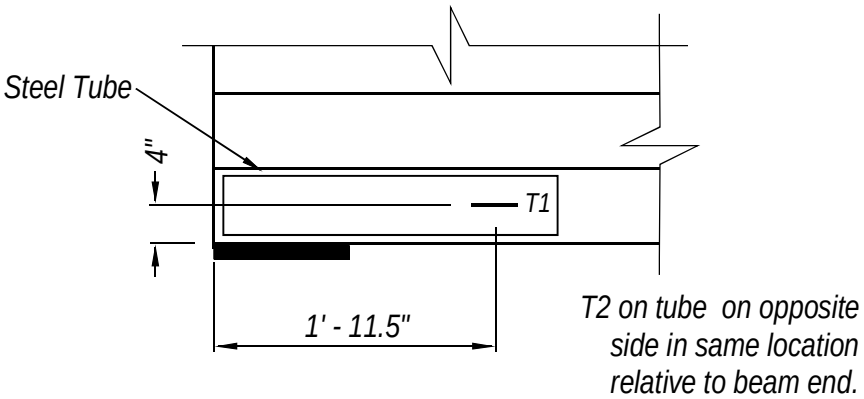

Figure 42 – Details of repair.

5.6 TEST SETUP AND PROCEDURES

Seven shear tests were conducted using a three-point loading scheme. Tests were conducting using five different shear span to depth (a/d) ratios ranging from 1.2 to 5.4. The general test configuration is shown in Figure 43 with specific dimensions given in Table 11. The load was applied by an actuator through a 1.5-in. thick x 10 in. x 20 in. (20-in. dimension perpendicular to girder length) reinforced neoprene bearing pad at a loading rate of 0.25 kips/second. Each end of each girder was supported by a 1.5-in. thick x 7 in. x 20 in. (20 in. dimension perpendicular to girder length) reinforced neoprene bearing pad. Load cells were used to measure the load applied by the actuator. Linear variable displacement transducers, LVDTs, were used to measure displacement at the load point and at each support. LVDTs were also used to measure strand slip (Figure 44).

Strain was measured at discrete locations using 60-mm strain gages and strain rosettes. Figure 45 through Figure 51 show the strain gage and strain rosette layouts for each test

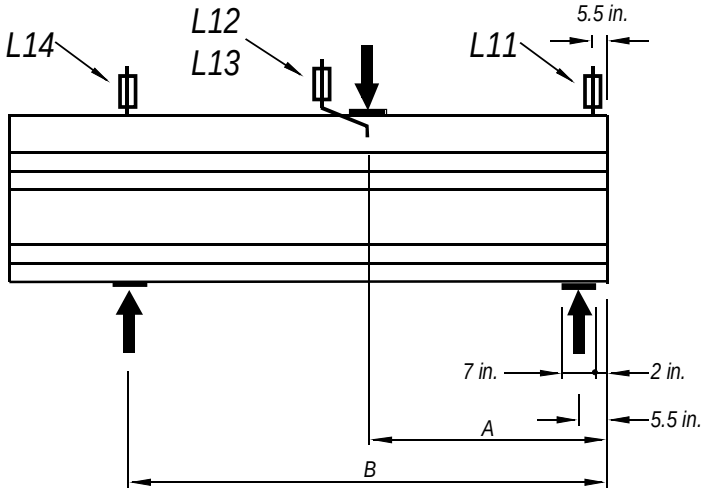

Figure 43 – Shear test setup.

Table 11 – Test setup geometry.

Test	A	B	a/d*
B1U1	4’ - 9”	44’ – 9”	1.2
B2U2	8’ - 3.5”	47’ - 0.5”	2.1
B4S2	8’ - 3.5”	44’ – 8”	2.1
B2U3	12’ - 5.5”	51’ – 0.5”	3.1
B1U4	16’ - 9”	56’ – 4”	4.2
B4U4	16’ - 9”	56’ – 9”	4.2
B3U5	21’ - 5.5”	59’ – 0.5”	5.4

*d = 48 in.

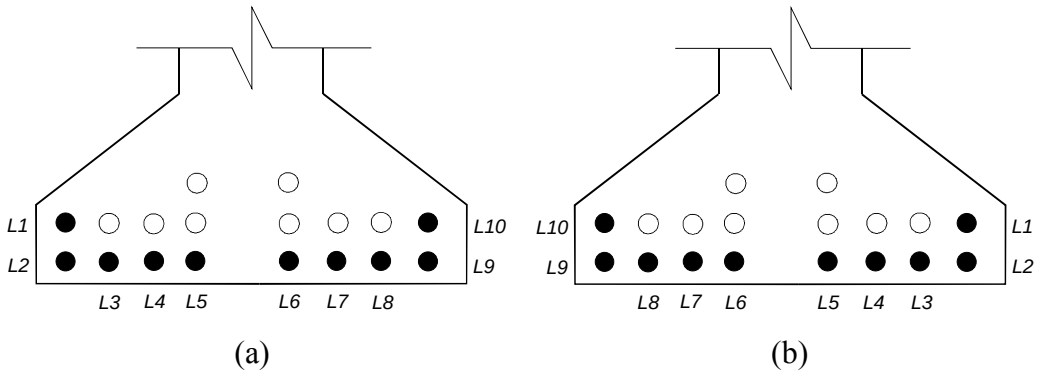

Figure 44 – Strands instrumented to measure slip on tests (a) B1U1, B2U3, and B4U4 (b) B1U4, B2U2, B3U5, and B4S2.

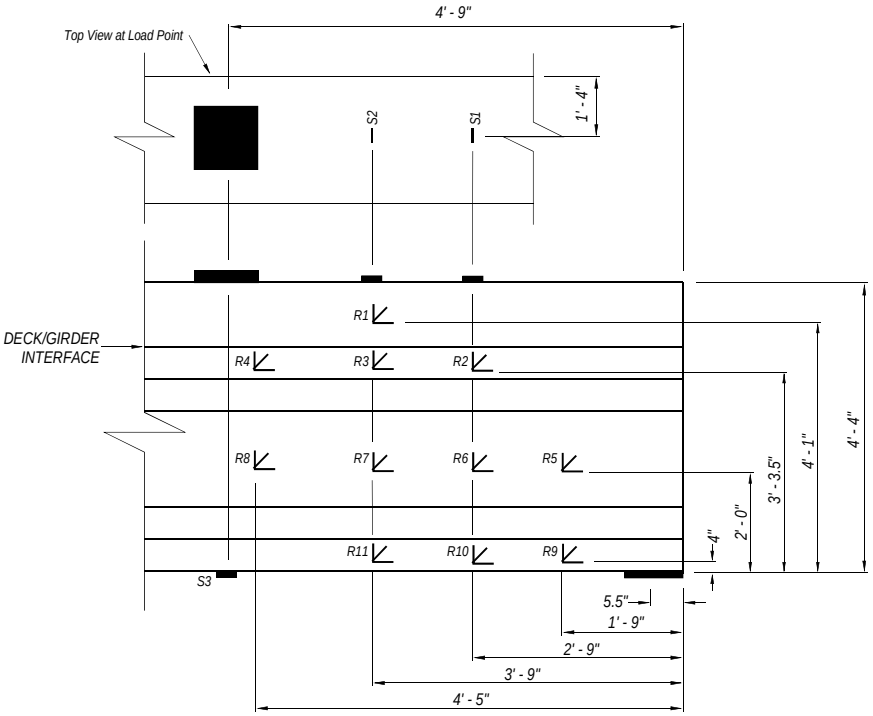

Figure 45 – B1U1 strain gage layout.

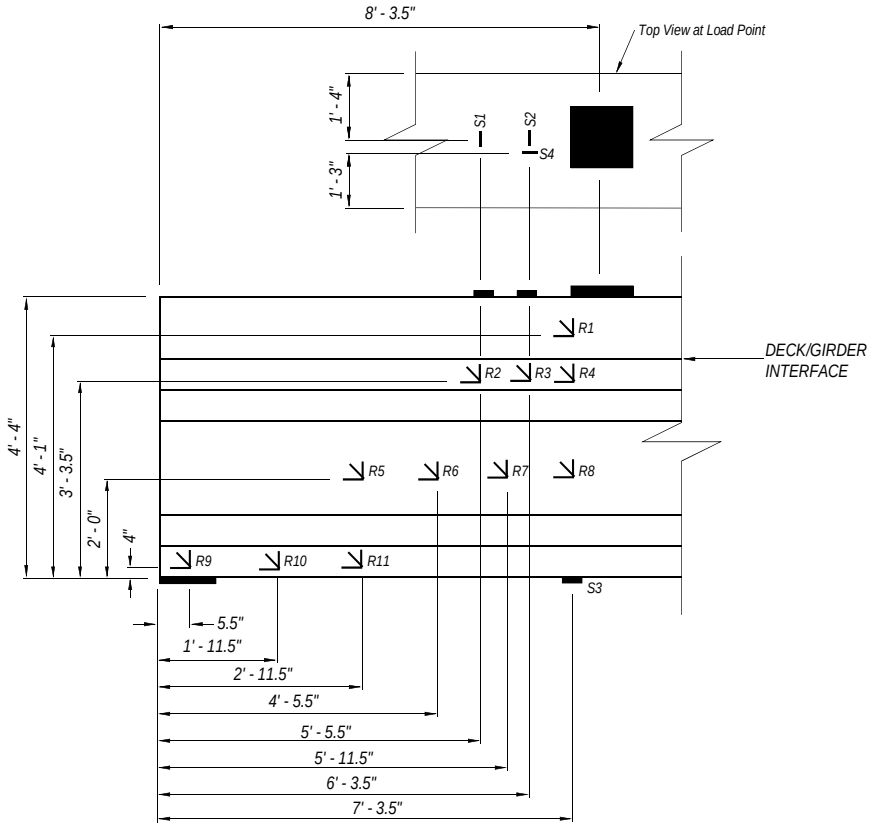

Figure 46 – B2U2 strain gage layout.

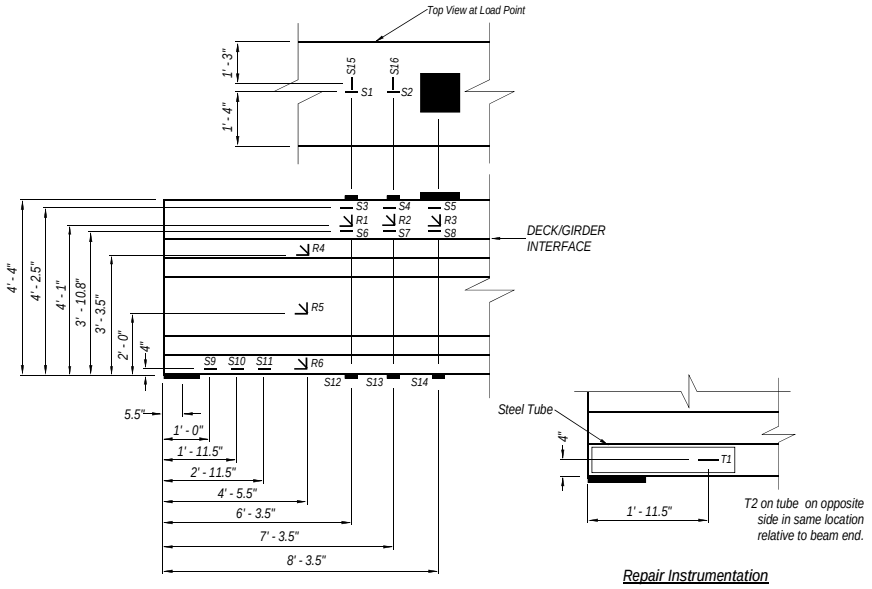

Figure 47 – B4S2 strain gage layout.

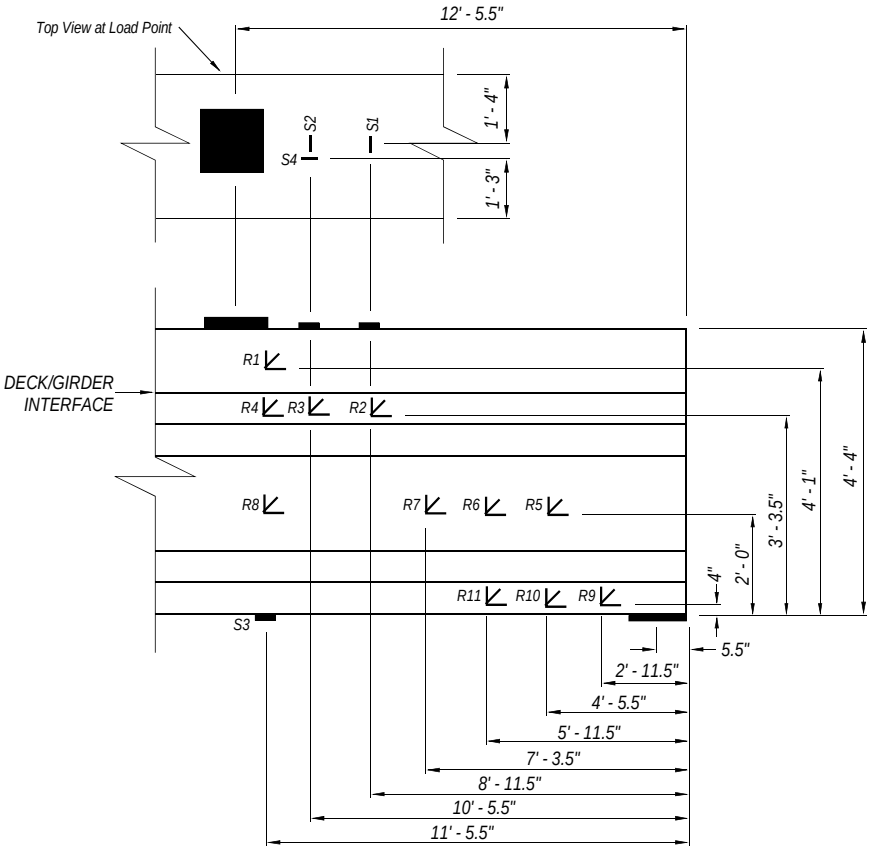

Figure 48 – B2U3 strain gage layout.

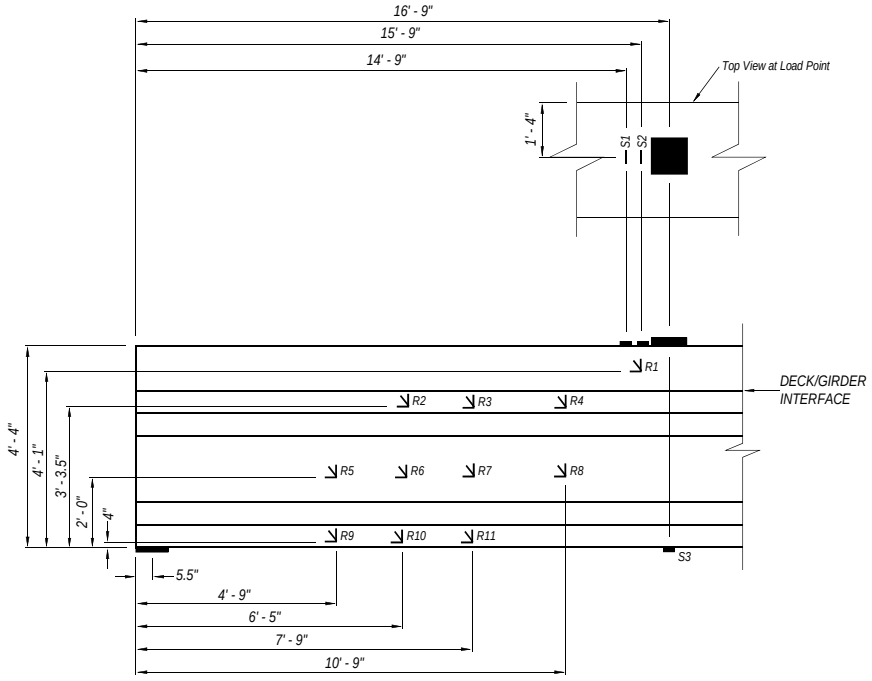

Figure 49 – B1U4 strain gage layout.

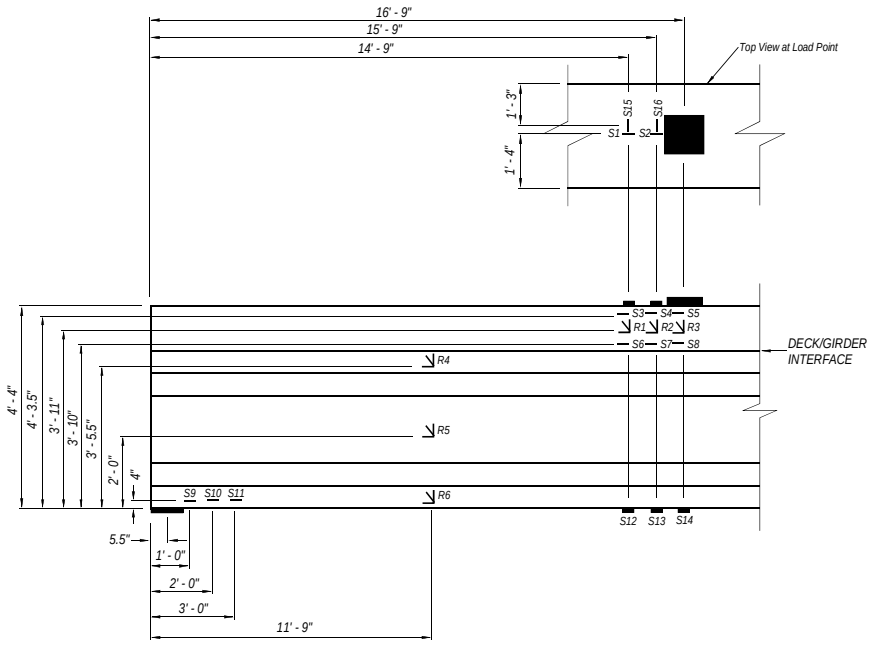

Figure 50 – B4U4 strain gage layout.

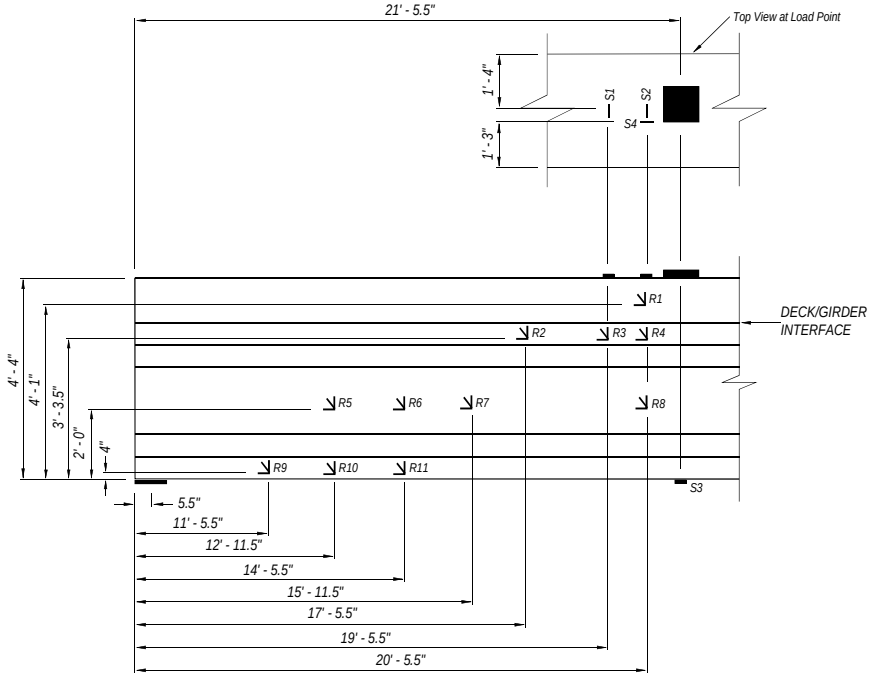

Figure 51 – B3U5 strain gage layout.

5.7 RESULTS AND DISCUSSION

Load, displacement, strain, and strand slip data are presented in this section. Load is presented in terms of *superimposed shear*. Superimposed shear is defined as the shear between the load point and the support as caused by the actuator. Note that girder self weight is not included in the superimposed shear. Furthermore, the displacements presented in the subsequent plots have been corrected for the rigid body movement using the measured support displacements and so reflect only the deformation of the girder caused by the superimposed load.

Test B1U1 was conducted using an a/d ratio of 1.2. Figure 52 shows the shear-displacement curve for B1U1. The girder behaved linear-elastically up until first cracking occurred at 182 kips. First and final cracking patterns are shown in Figure 53. Strain rosette R9 was the closest instrumentation to the initial crack. Data from this gage confirms the linear elastic behavior up to, and the cracking at, 182 kips (Figure 54).

The girder eventually reached a peak shear capacity of 331 kips.

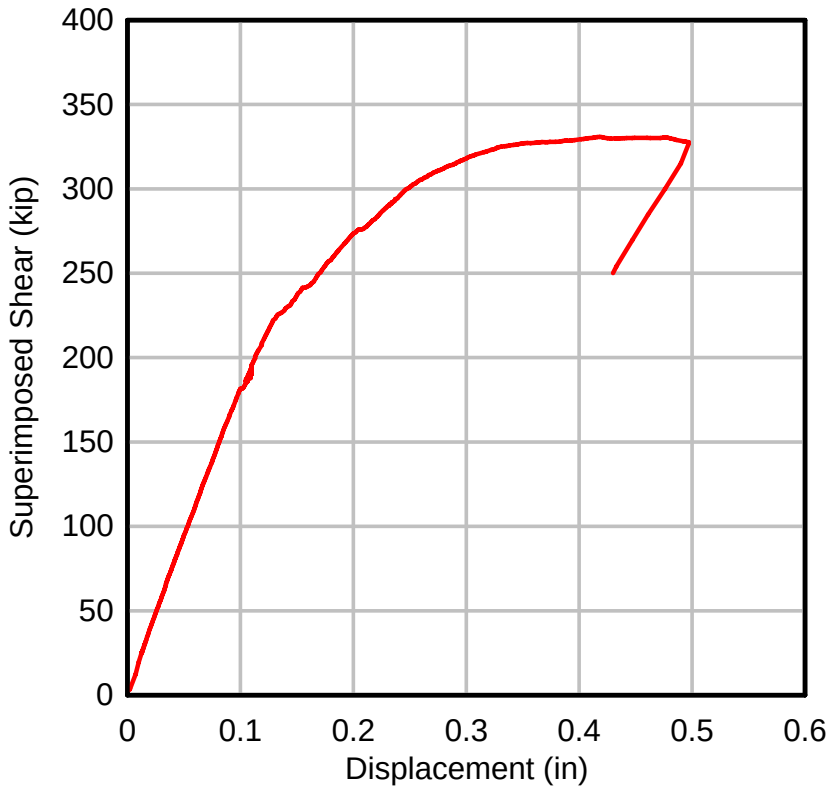

Figure 52 – Shear vs. displacement B1U1.

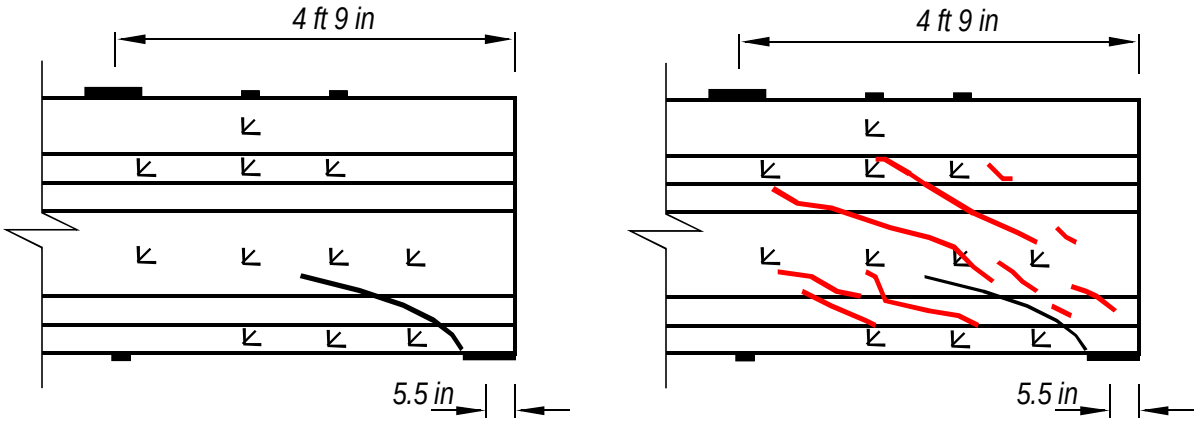

Figure 53 – B1U1 first and final crack pattern.

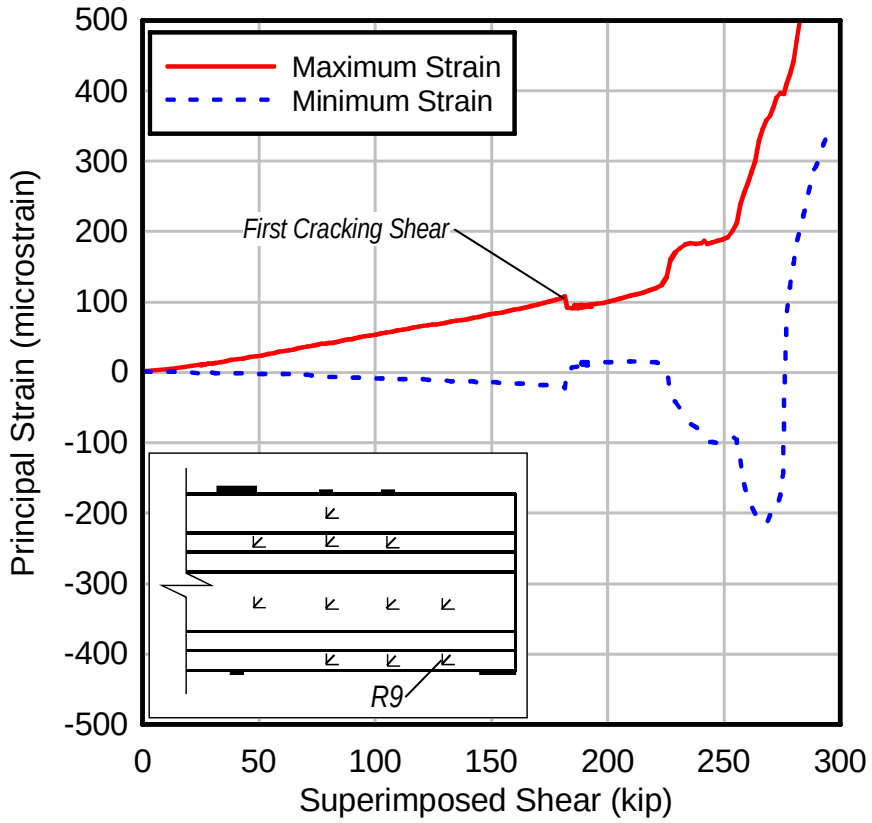

Figure 54 – Strain rosette R9.

Figure 55 shows a plot of shear vs. displacement and shear vs. strand slip for three selected strands. Recalling that the first crack formed at 182 kips, Figure 55 shows a slight slip in the strands at that load. The crack formed near the face of the bearing and likely shortened the available development length for the strands sufficiently to result in slip. Reserve load capacity,

however, was provided by the supplemental vertical and horizontal mild steel reinforcement included in the end region of the girder. If the girder was constructed without this end reinforcement, it is likely that a mechanism would have formed and the girder would have been unable to carry additional load. The capacity would have been dependent solely on the slip resistance of the strand between the crack and the girder end.

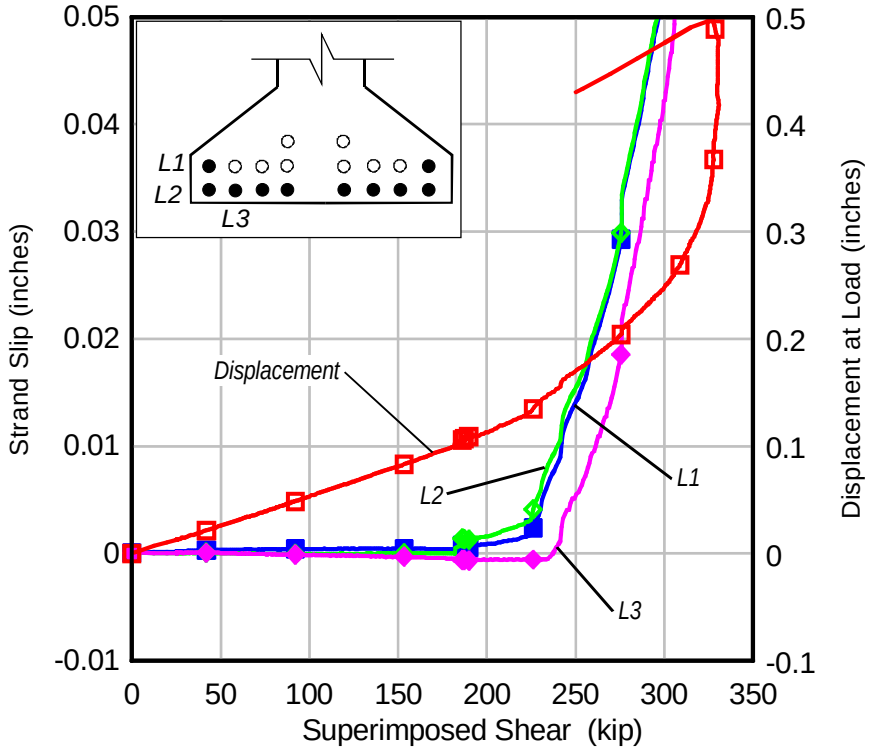

Figure 55 – B1U1 strand slip and displacement.

The photograph in Figure 56 shows the girder with the primary crack and the associated free body diagram with the forces generated when the flexure-shear crack formed. As shown in the free body diagram, the mild steel reinforcement in the end of the beam is activated when the crack forms and the strands slip. As the load was increased, however, the steel eventually either yielded or failed in bond or both. Figure 54 and Figure 55 both exhibit a range between 182 kips and 230 kips where the strand continues to slip and there is a slight loss in stiffness. After 230 kips, though, the strand slip increases markedly and the stiffness begins to decrease rapidly. This is thought to be where the mild steel reinforcement yielded. Due to the gradual reduction in stiffness exhibited in the load-displacement plot, it is believed that some of the bars reached

yield. If some or all of the bars had experienced a bond failure, the load displacement would have indicated a sudden decrease in load.

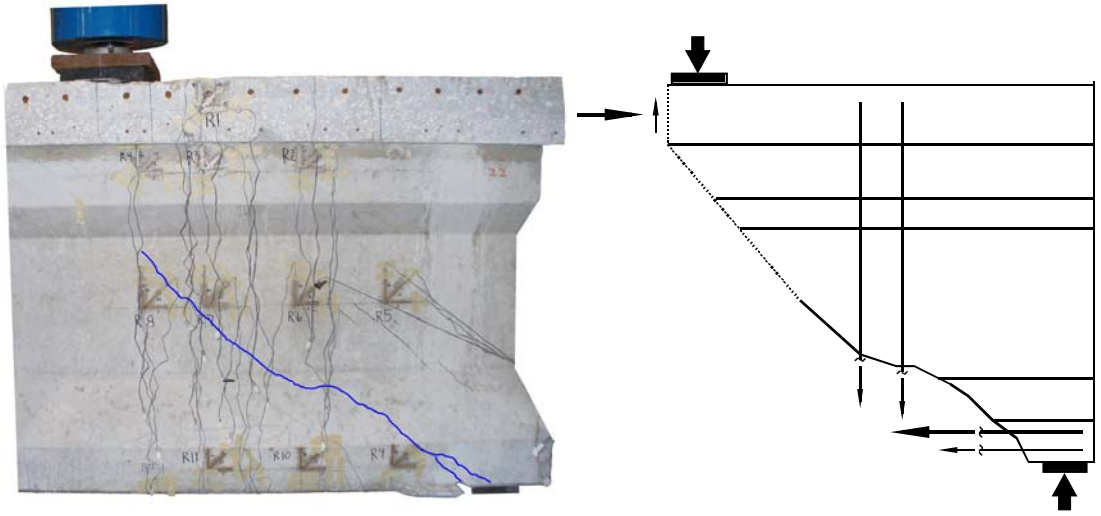

(a) (b)

Figure 56 – Girder B1U1 (a) photo with the primary crack enhanced and (b) free body diagram including contribution of vertical and horizontal reinforcement

Test B2U2 was conducted using an a/d ratio of 2.1. Figure 57 shows the shear vs. displacement curve for B2U2. The girder behaved linear-elastically up until first cracking, which occurred at 182 kips as indicated by strain rosette R10 (Figure 58). This was the closest instrumentation to the initial crack. The girder reached a peak shear of 244 kips.

Figure 59 shows that strand slip was detected at the same load as initial cracking. The formation of cracks near the support reduced the available development length of the strands, leading to bond failure between the strands and the concrete. The girder was able to sustain additional load in a manner similar to that of girder B1U1 due to the mild steel located at the end of the girders. Cracking patterns are shown in Figure 60.

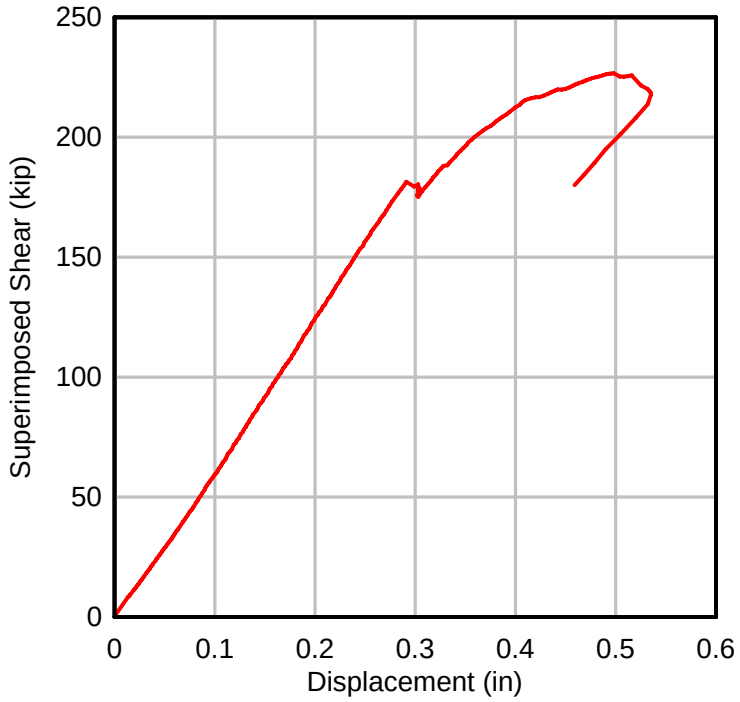

Figure 57 – Load vs. displacement B2U2.

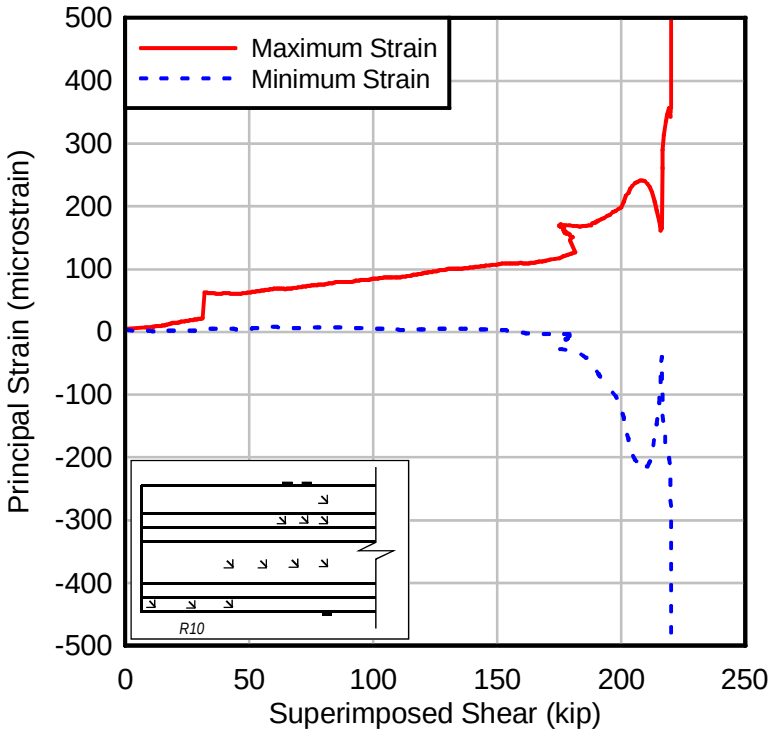

Figure 58 – B2U2 strain rosette plot R10.

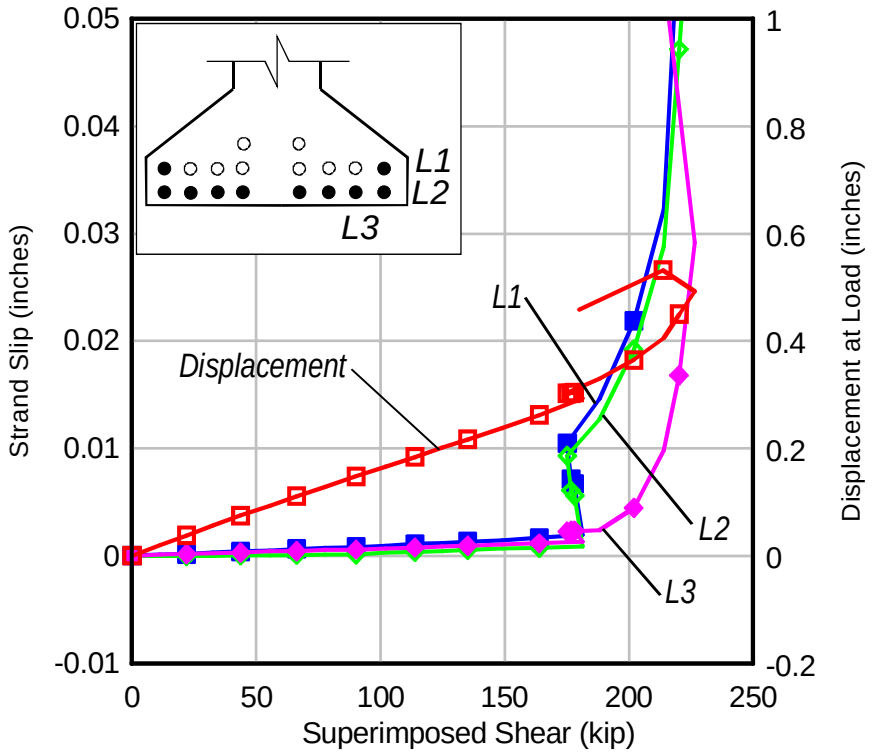

Figure 59 – B2U2 strand slip and displacement.

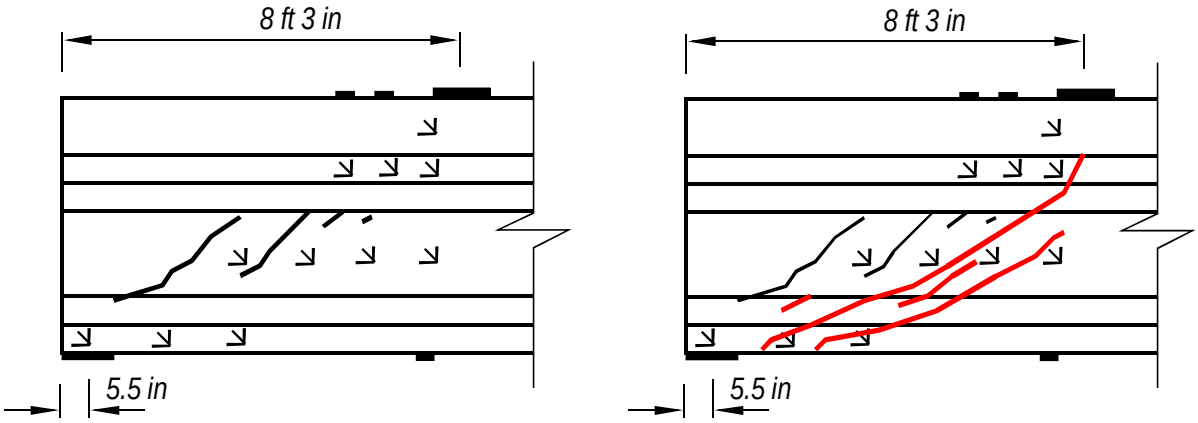

Figure 60 – First and final crack pattern for B2U2.

The shear vs. displacement curve for test B4S2 is shown in Figure 61. The change in slope at 40 kips is likely an anomaly caused by the data acquisition and does not indicate a change in behavior. Beyond this load the slopes of both plots remain relatively stable until a shear of 162 kips is reached, at which point initial cracking occurs. This is about 10% less than the initial cracking shear for B2U2. Furthermore, strands L1 and L2 appear to begin to slip at a

faster rate after this crack formed (Figure 63), indicating that the mild steel reinforcement at the end of the girder was engaged.

Loading continued, with additional cracks forming at a shear of 198 kips. The strain reported by strain rosette R5 increased sharply at this load, indicating the formation of additional cracks (Figure 62). Accelerated strand slip was noted at a shear of 198 kips (Figure 63). The girder reached a maximum shear of 232 kips. At this shear, the strands lost bond resulting in failure of the girder. Final crack patterns are shown in Figure 64.

Comparing Figure 59 and Figure 63, it appears that the repair scheme provided a small improvement in the bond between the strands and the concrete. During test B2U2 (unrepaired, a/d=2.1, Figure 59) sharp increases in strand slipped occurred at 182 kips compared to 198 kips for test B4S2 (repaired, a/d-2.1, Figure 63). Even with the repair, however, the failure mode for test B4S2 was strand slip.

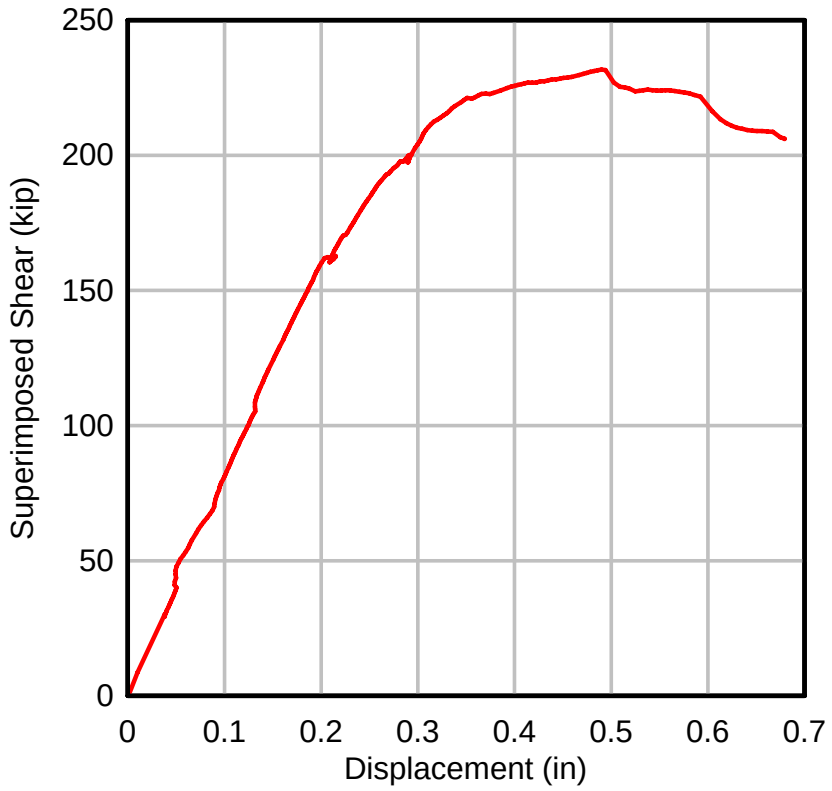

Figure 61 - Load vs. displacement B4S2.

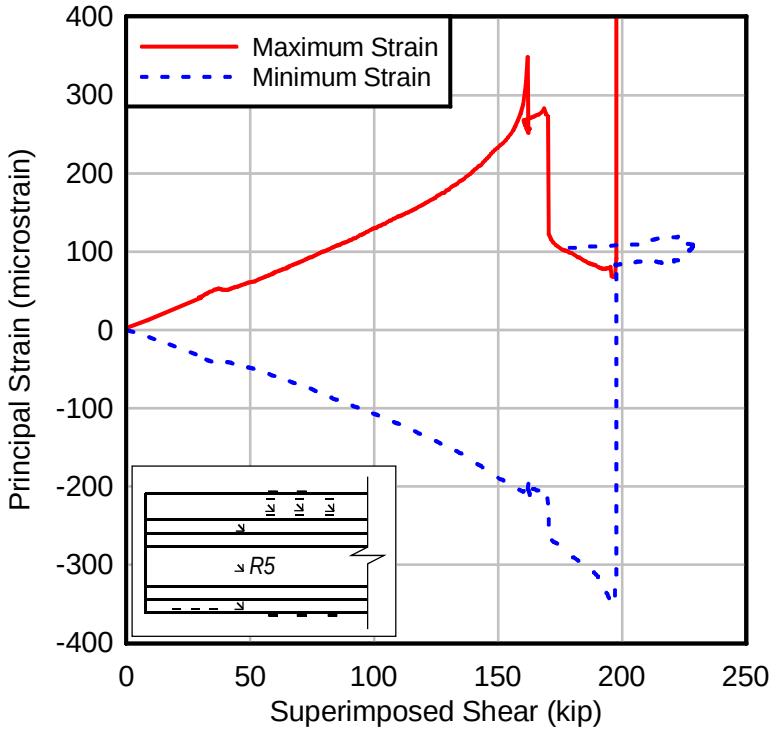

Figure 62 – Strain rosette plot R5.

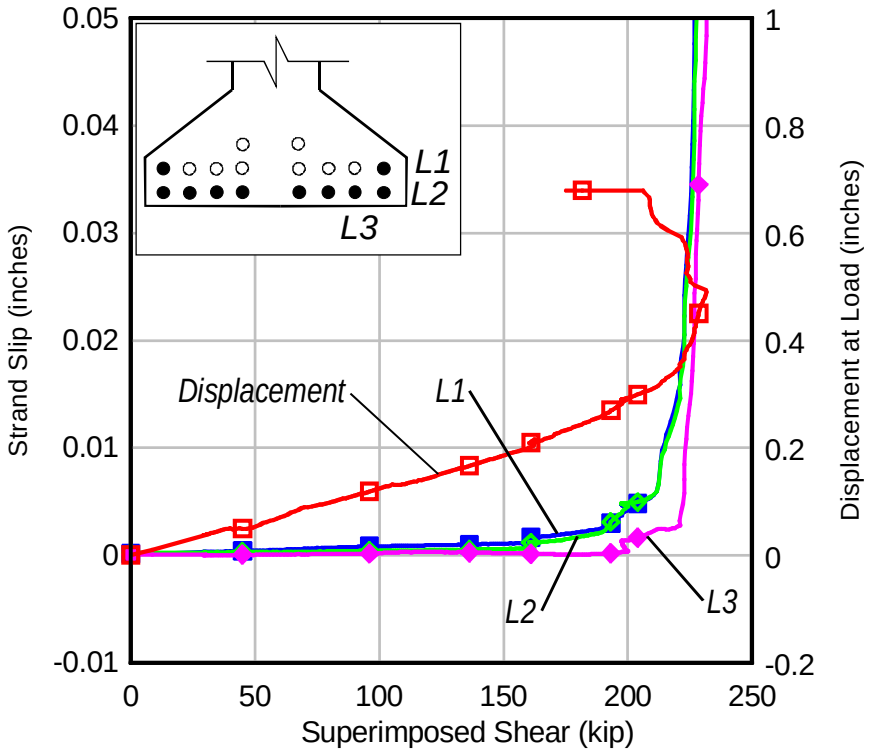

Figure 63 – B4S2 strand slip and displacement.

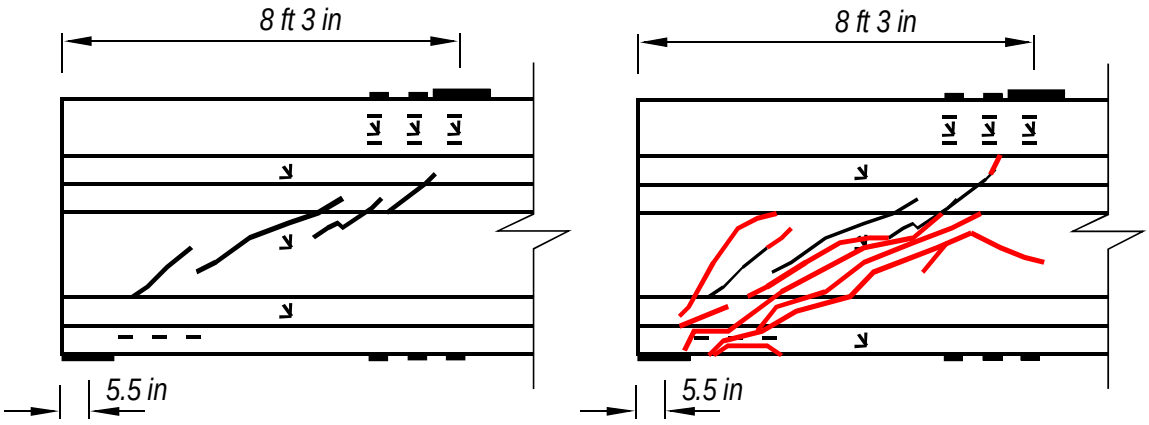

Figure 64 – First and final crack pattern for B4S2.

The shear vs. displacement curve for test B2U3 is shown in Figure 65. As demonstrated by this figure, the girder behaved linear elastically until the shear reached 159 kips (Figure 66), where the first cracks were detected. Figure 67 shows shear vs. strand displacement. The strands began to slip moderately from 159 kips up to a shear of approximately to 174 kips indicating that the end reinforcement had been engaged. The strand slip increased sharply at 174 kips, indicating that the mild steel had yielded. The girder's stiffness dropped rapidly as shear was increased beyond 174 kips. The maximum shear supported by the girder was 197 kips. Initial and final crack patterns are shown in Figure 68.

Similar to tests B1U1, B2U2, and B4S2, the mode of failure for test B2U3 was bond failure between the strand and the concrete. Initial cracks reduced the length available for strand development. The loss in development length led to the initial strand slip. After the initial strand slip, the tensile force in the strands began to transfer to the horizontal reinforcement. Although the horizontal reinforcement improved the girder's ductility, it was insufficient to develop the full moment capacity of the girder.

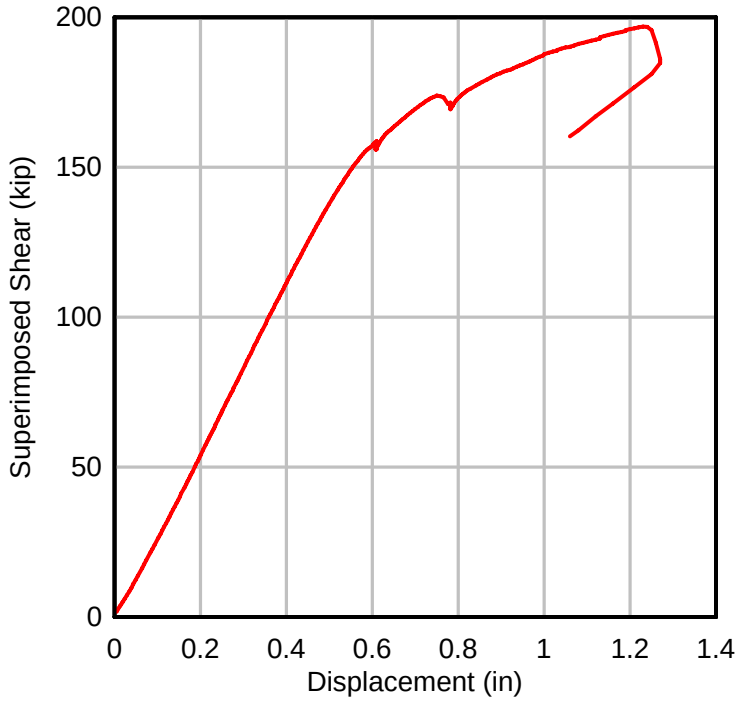

Figure 65 – Load vs. displacement B2U3.

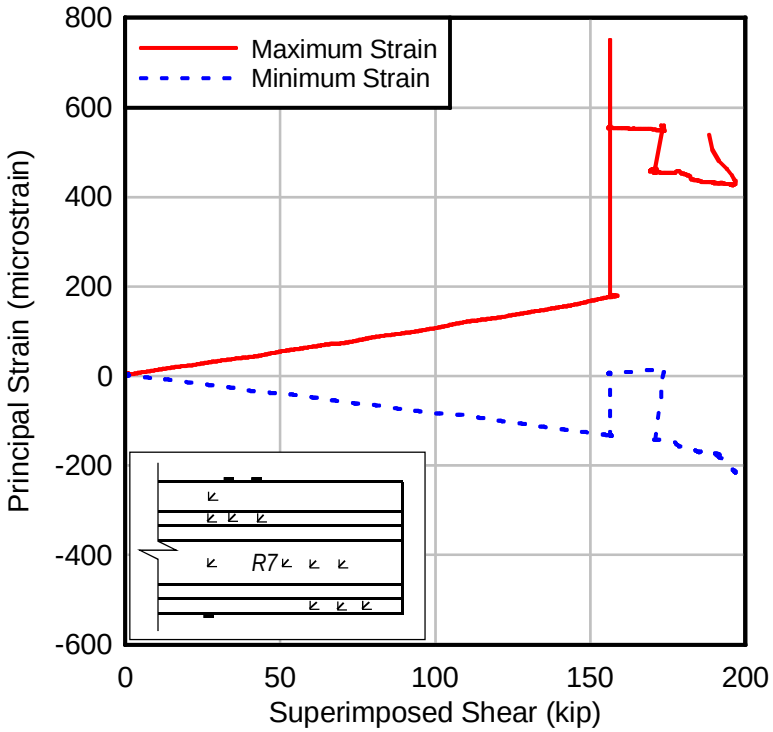

Figure 66 – Strain rosette plot R7.

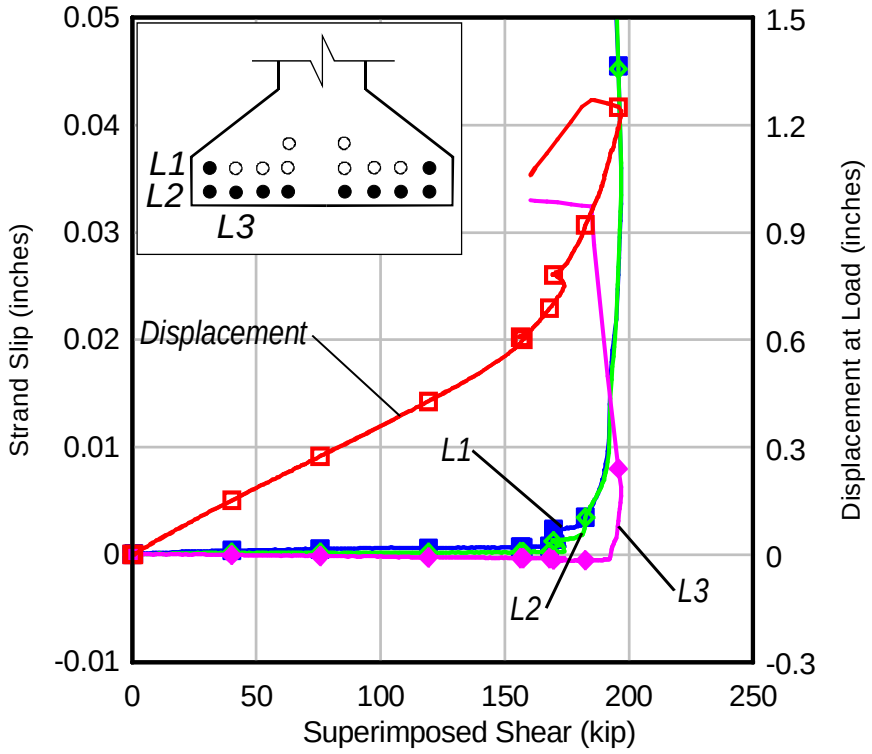

Figure 67 – B2U3 strand slip and displacement.

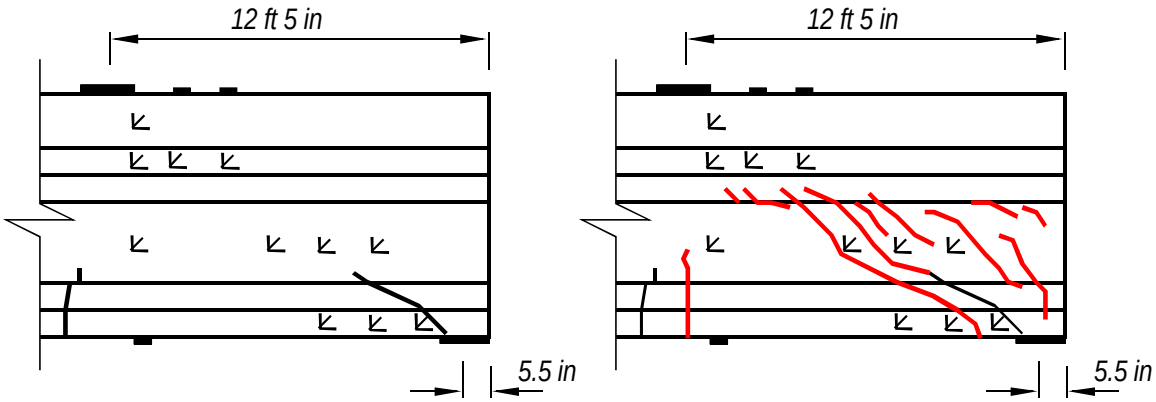

Figure 68 – First and final crack pattern for B2U3.

The shear vs. displacement curve for test B1U4 is shown in Figure 69. The girder behaved linear-elastically until the shear reached 104 kips. At this load, the slope of the shear-displacement curve begins to change to a more gradual slope. The slope continued to change until the shear reached 125 kips, beyond which the slope and was approximately constant for the remainder of the test. The reduction of stiffness (change of slope) resulted from the formation of

cracks and yielding of the prestressing steel. Strain rosette R5 (Figure 70) was the instrument closest to the initial diagonal crack. The data show a sharp increase in strain at a shear of 148 kips, indicating the formation of a web crack. In addition, moderate strand slip was noted (Figure 71) at this same load indicating that the mild steel at the beam end had been engaged. The web cracks propagated into the bottom flange and compression zone as the load was increased. The girder failed at a shear of 171 kips due to crushing of the compression zone (Figure 72a), which was accompanied by the bottom face of the bulb delaminating from the girder (Figure 72b). The crack in the compression zone propagated through the joint between the precast panels and ultimately caused the longitudinal bars in the deck to buckle. Failure mode of test B1U4 is categorized as a shear-compression failure. Although the strand did slip moderately, resulting in the mild steel being engaged, the mild steel had sufficient strength to ensure that the capacity was not controlled by strand slip.

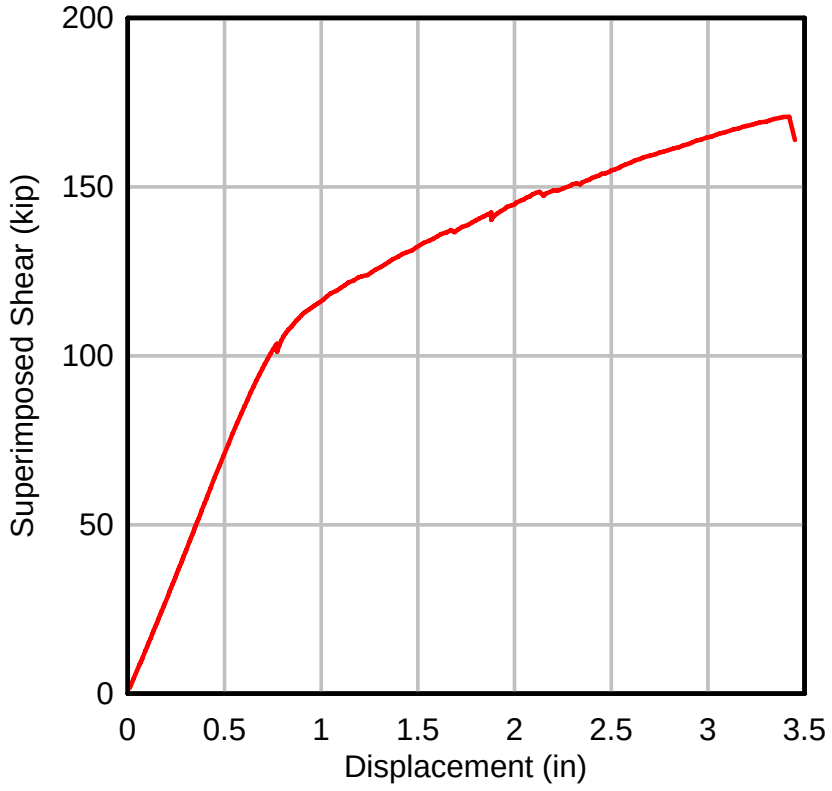

Figure 69 – Load vs. displacement B1U4.

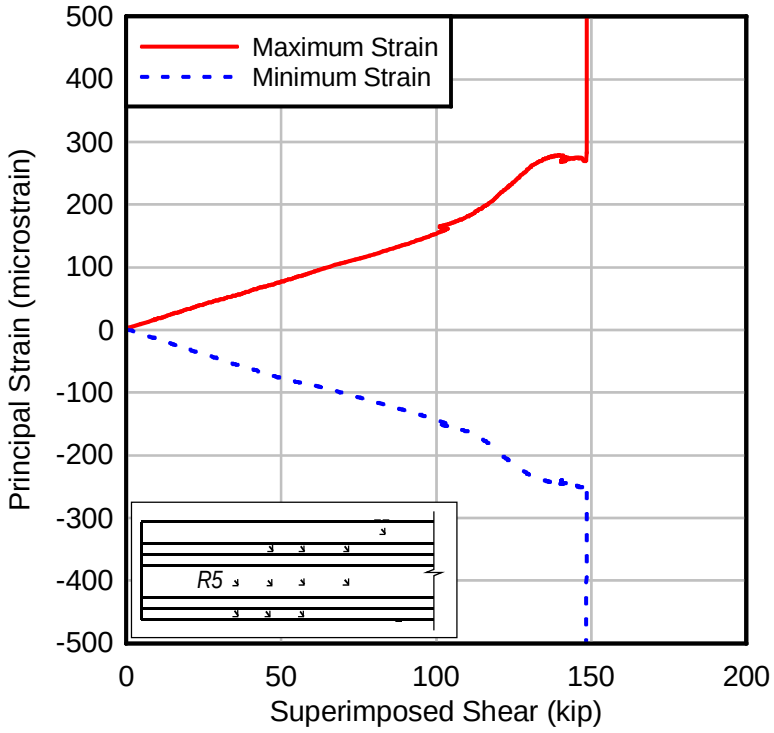

Figure 70 – Strain rosette plot R5.

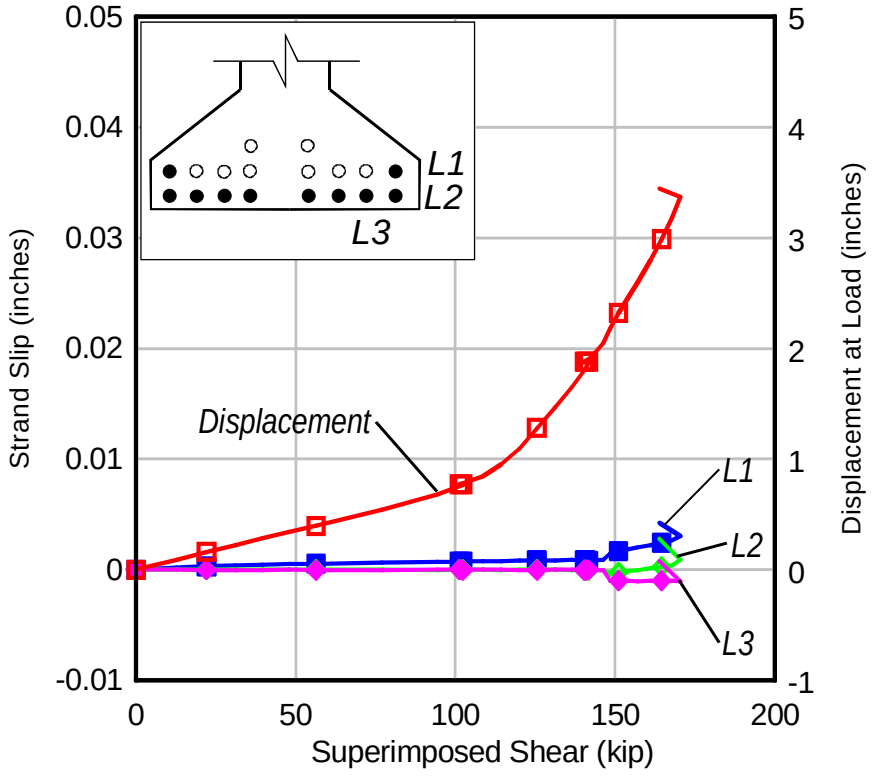

Figure 71 – B1U4 strand slip and displacement.

(a) (b)

Figure 72 – B1U4 failure (a) crushed compression zone and (b) separation of bottom bulb.

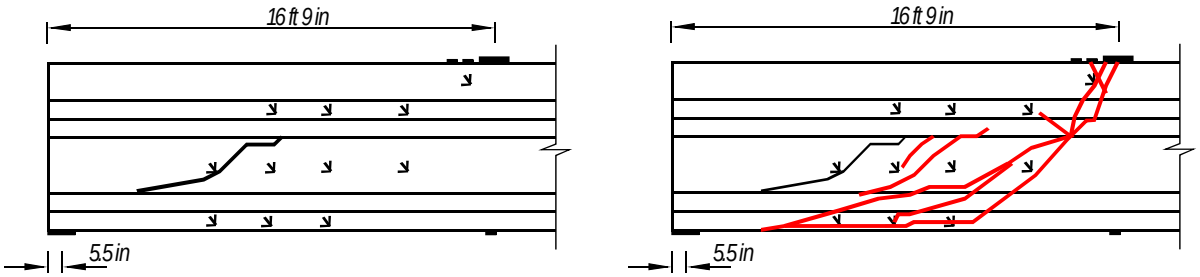

Figure 73 – First and final crack patterns of B1U4 (flexural cracks not shown).

The shear vs. displacement plot for test B4U4 is shown in Figure 74. The girder behaved linear-elastically until the shear reached 100 kips, at which point the girder begins to lose stiffness due to flexural cracking and yielding of the prestressing steel. This behavior was observed at approximately the same shear as the previous test conducted at an a/d of 4, B1U4.

Based on the data from strain gages S12, S13, and S14 (Figure 75) the initial flexural cracks formed at a shear of approximately 92 kips. These gages were located on the bottom of the girder below the load point and reported steady growth in strain until the shear reached approximately 92 kips. At this point the gages report a loss of tension, indicative of crack formation. The slope of the shear-displacement plot continued to decrease as the shear increased from 100 to 120 kips. The slope remained approximately constant at shears beyond 120 kips.

Additional cracking occurred at 120 kips, as indicated by the abrupt changes in strain as shown in Figure 76 and Figure 77. Figure 77 shows the strains registered by gages S6, S7, and

S8. These gages were located on the underside of the deck near the load point. They registered constant growth of compression strain until the shear reached 120 kips, at which point they began to lose compressive strain. The load was held at 137 kips to mark the cracks. Loading was resumed until the beam reached its maximum capacity of 188 kips. Failure was sudden and resulted in the loss of a portion of the bottom flange.

Moderate strand slip appears to begin at approximately 130 kips. This moderate change occurs until shortly before failure (See Figure 77). First and final cracks can be seen in Figure 79.

Although the damage in the compression zone near the load point was not as extreme as that of the B1U4, this failure mode is categorized as shear-compression. For this test, the cracks initially started as flexure cracks. As the girder was loaded, cracks began to form in the web and grow towards the support. The concentration of cracks near the support is what caused the strands eventually to slip.

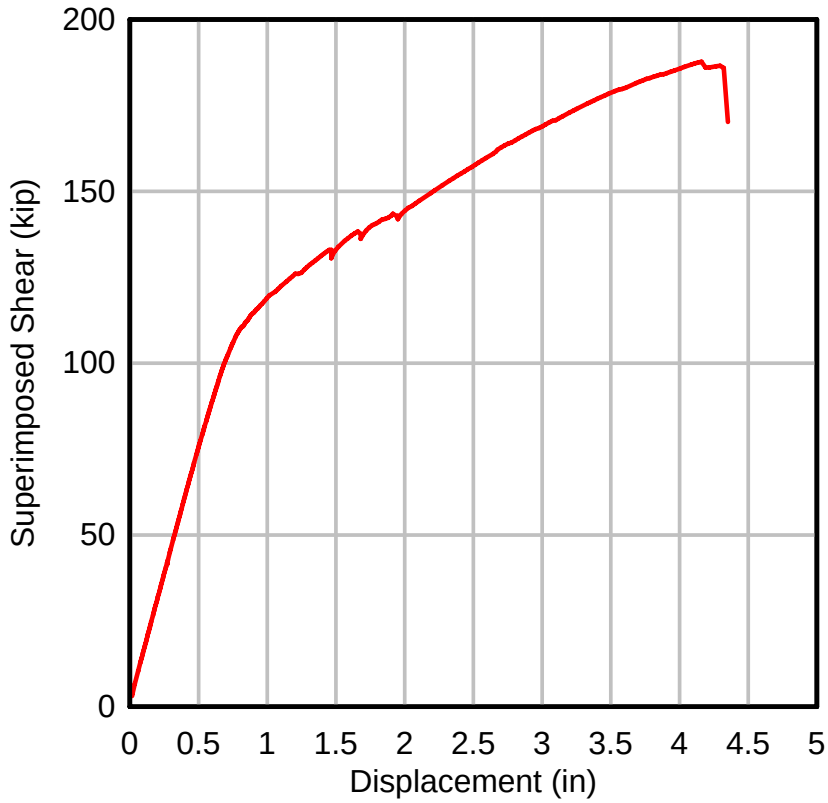

Figure 74 – Load vs. displacement B4U4.

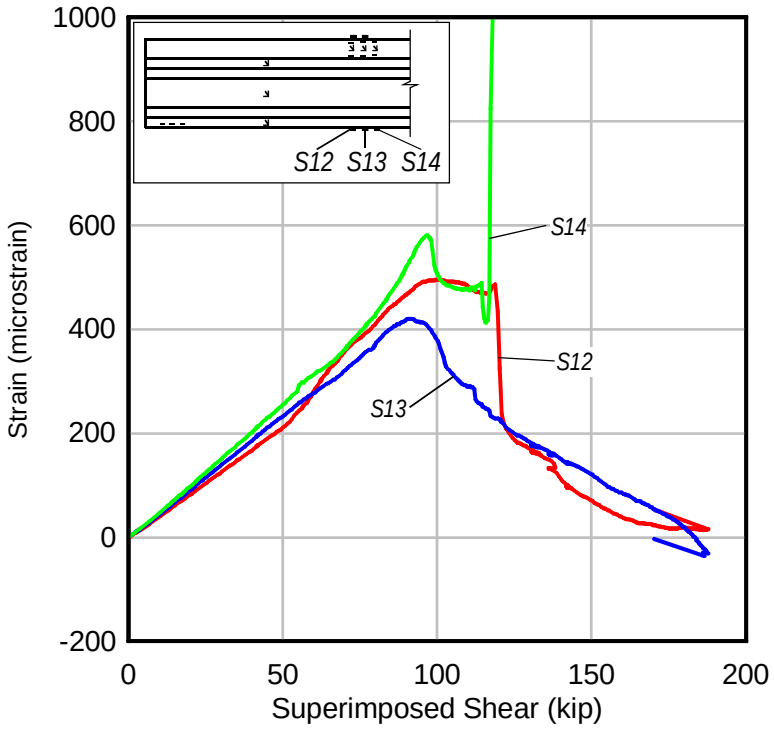

Figure 75 – Strain gages S12, S13, and S14.

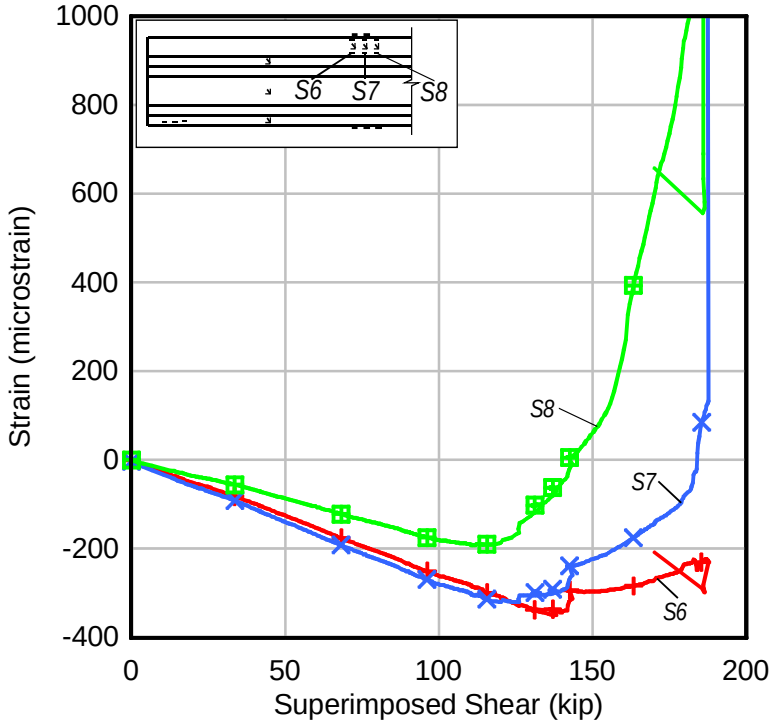

Figure 76 – Strain gages S6, S7, and S8.

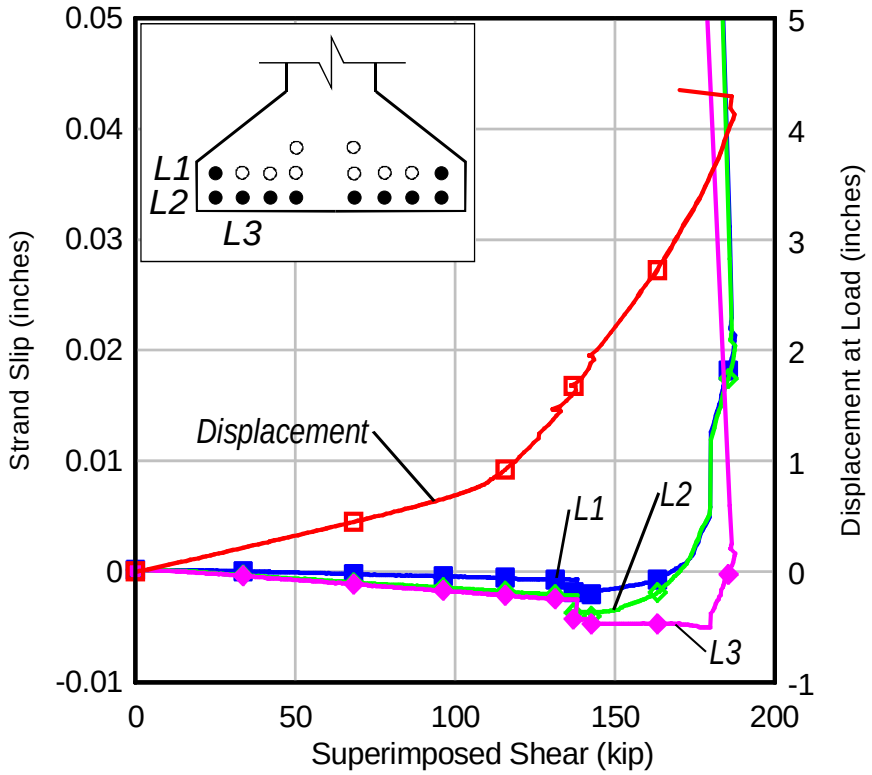

Figure 77 – B4U4 strand slip and displacement.

(a) (b)

Figure 78 – Girder B4U4 after testing (a) shear span and (b) load point.

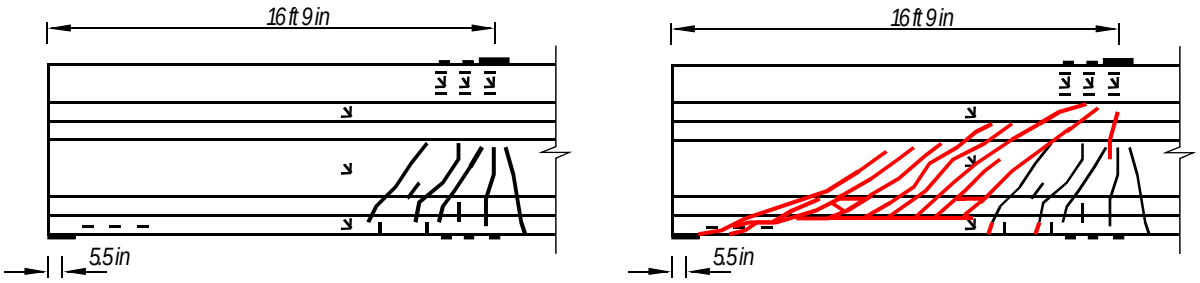

Figure 79 – First and final crack pattern for B4U4.

The shear vs. displacement plot for test B3U5 is shown in Figure 80. The girder behaved linear-elastically until the shear reached 81 kips. Strain from gage S3 (Figure 81) indicated that cracking occurred at a lower shear (72 kips) than indicated by the load-displacement. Strain from rosette R8 (Figure 82), however, indicated that the crack had not entered the web until the shear was 89 kips. The girder reached a peak shear of 151 kips when compression zone failed. The failure was categorized as flexure.

Moderate strand slip occurred at approximately 120 kips as shown in Figure 84. The girder reached flexural capacity, however, before the strands showed significant slip indicating that sufficient development length was available to develop the full flexural capacity of the section.

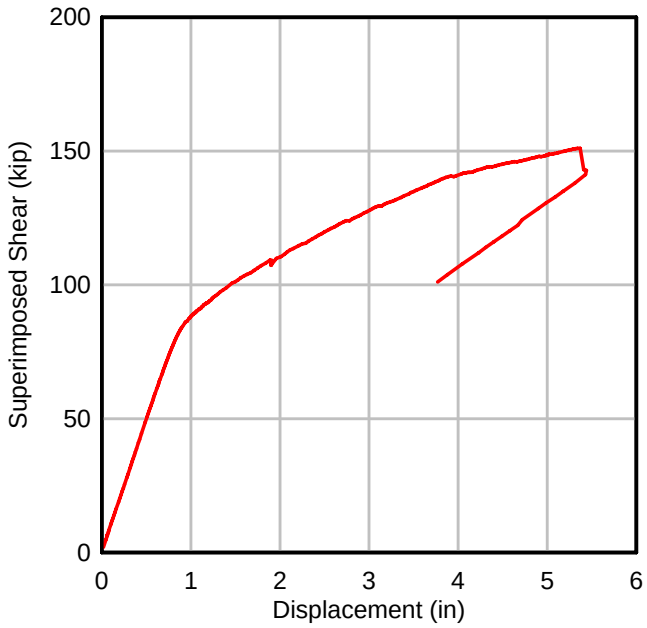

Figure 80 – Load vs. displacement B3U5.

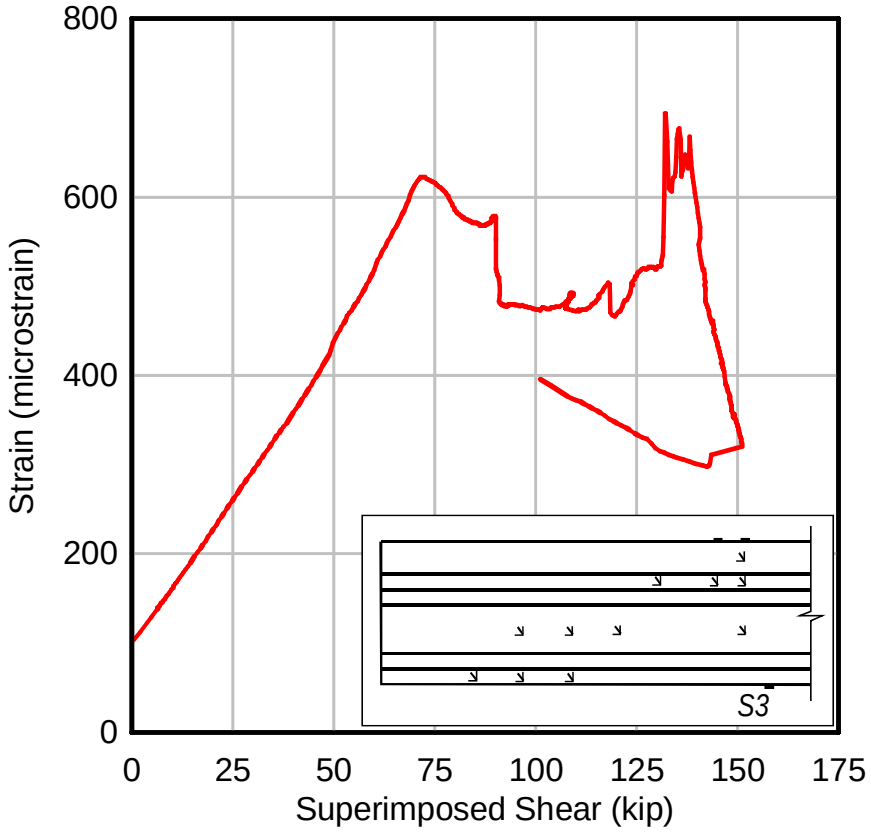

Figure 81 – B3U5 strain gage S3.

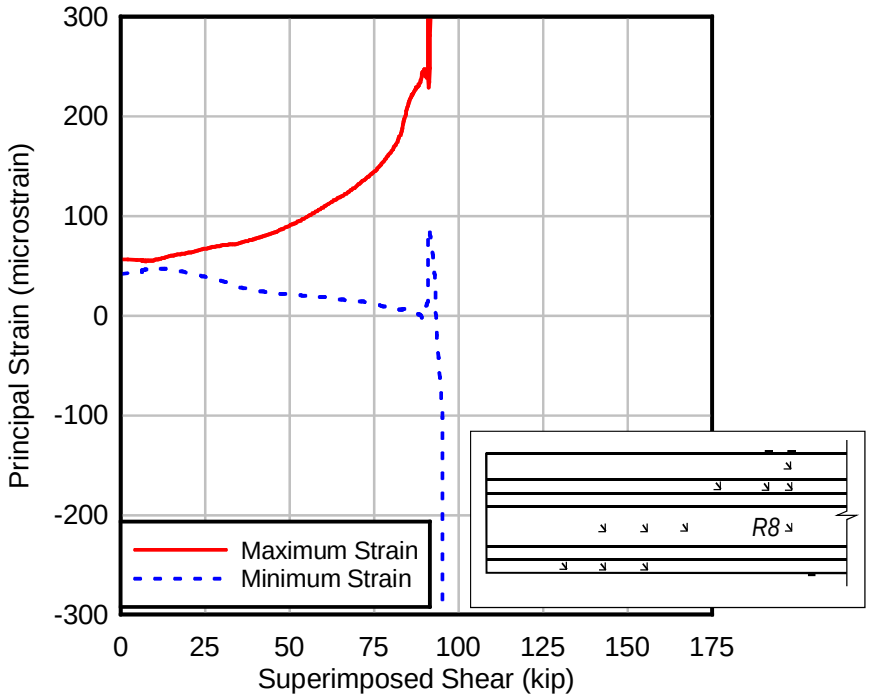

Figure 82 – B3U5 strain rosette plot R8.

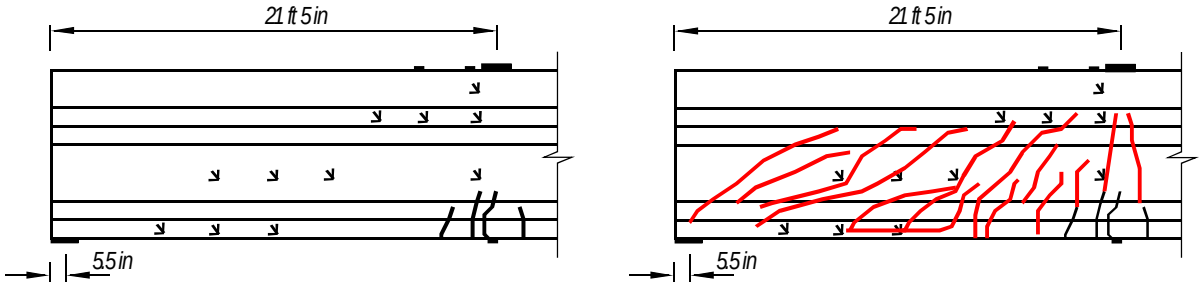

Figure 83 – First and final crack pattern for B3U5.

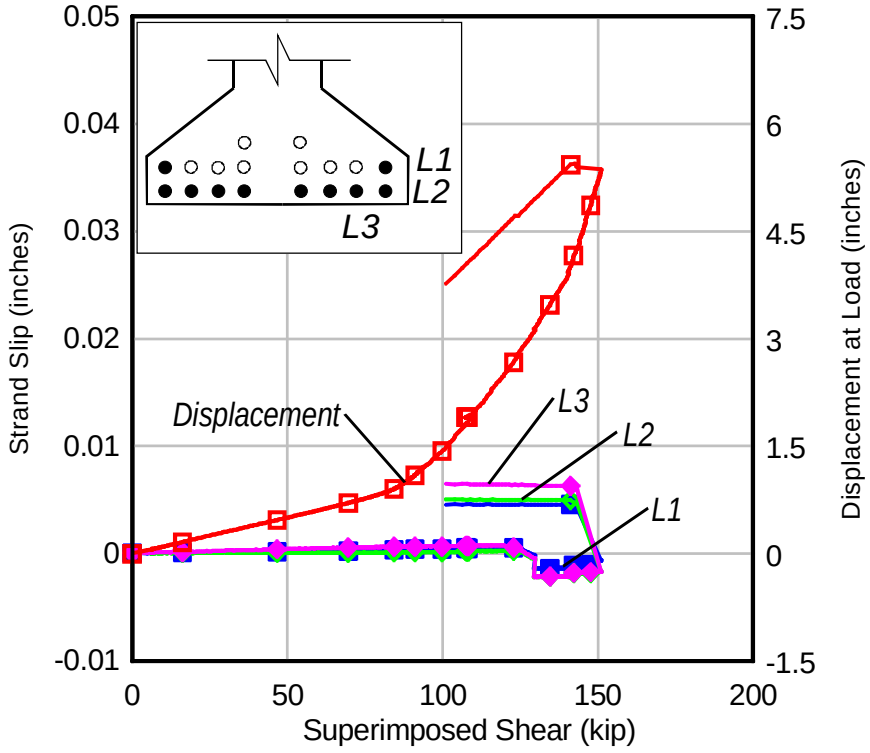

Figure 84 – B3U5 strand slip and displacement.

5.8 Summary of Results

Seven tests were conducted using shear span to depth ratios ranging from 1 to 5. Table 12 summarizes the mode of failure for each test.

Tests conducted with an a/d ratio of 3 or less all resulted in a bond failure. The characteristics used to categorize a bond failure included: excessive strand slip (greater than 0.03 in.) and failure to reach the predicted moment capacity. Strand slip occurred due to the formation of cracks in the bottom bulb near the support (Table 11). These cracks reduced the development length such that the strands could not fully develop. After these cracks formed, the

mild steel reinforcement crossing the crack in the end region of the girder was engaged and began carrying load. The engagement of this mild steel delayed the formation of a collapse mechanism, increased the ultimate capacity, and improved the ductility of the post-cracking behavior. Without this end reinforcement, the girders tested with a/d < 3.0 would likely have failed at lower capacities.

For tests with an a/d = 4, the failure mode was shear-compression and bond. The characteristics used to define this failure mode were: a high concentration of shear cracks in the web and flexural cracking under the load point, complete loss of bond through delamination of the bottom bulb in the shear span, and failure of the compression zone near the load point. Although present, strand slip did not affect the failure mode until failure was imminent. Failure was precipitated, at least partially, by the complete loss of bond in the shear span. For both tests, however, girders either were near or exceeded their calculated moment capacity.

For tests with an a/d = 5, the failure mode was flexure. Flexural failure was denoted by the even distribution of flexure and flexure-shear cracks that formed at or near the load point.

Table 12 – Failure modes.

Test	Failure Mode
B1U1	Bond
B2U2	Bond
B4S2	Bond
B2U3	Bond
B1U4	Shear-compression and bond
B4U4	Shear-compression and bond
B3U5	Flexure

Table 13 – Distance from end of girder to closest crack.

Test	Distance from end of girder to closest crack (in.)
B1U1	10.5
B2U2	14.0
B4S2	7.5
B2U3	16.0
B1U4	34.0
B4U4	12.0
B3U5	41.0

5.9 Comparison of Results with Calculated Shear Capacity

Table 14 shows a comparison of the experimental girder capacity with calculated capacities using the following methods:

1. Modified compression field theory (MCFT) from AASHTO LRFD Bridge Design Specification (2007).
2. Strut and Tie method (STM) from AASHTO LRFD Bridge Design Specification (2007).
3. Detailed method (ACI) from American Concrete Institute ACI 318 (2008)

The failure modes assumed by these methods do not necessarily match those observed in the tests. The comparison, however, gives perspective regarding the predicted vs. actual capacities. The experimental shear capacity shown in the table includes the measured superimposed shear and the calculated shear from self weight at the load point. STM was calculated for short shear spans only to reflect the applicability of the model.

MCFT provided conservative predictions for all a/d ratios. The accuracy of the MCFT predictions increased as the a/d ratio increased.

Calculated capacities using the strut and tie method were only for tests with a/d ratios of 1 and 2 since other failure modes were likely to control with higher ratios. STM significantly underestimated the girder capacity (Figure 85, Figure 86). Only the fully bonded strands and lowest layer of mild steel were considered as ties. The forces in the ties were limited by the lack of development length, and were the controlling factor for the STM prediction. The models did not account for the enhanced strength caused by the mild steel bars detailed in the girder end.

The ACI method produced the most accurate predictions. The ACI method was the only method that over-estimated the shear capacity. This occurred at a/d ratio of 3.

Nominal moment capacity, M_n, was calculated using the principles of strain compatibility. Table 15 summarizes the applied moment at failure for each test, along with the corresponding nominal moment capacity. The applied moment includes the self weight of the girder. The following material properties were used to calculate moment capacity: compressive strength of concrete was 5.6 ksi, prestress in the strands was 190 ksi, ultimate tensile strength was assumed to be 270 ksi, and Young's modulus for the strands was 28,500 ksi.

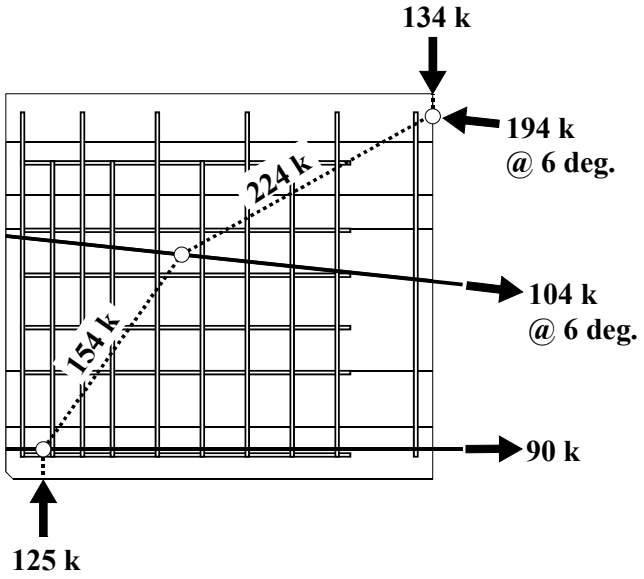

Figure 85 – STM a/d=1

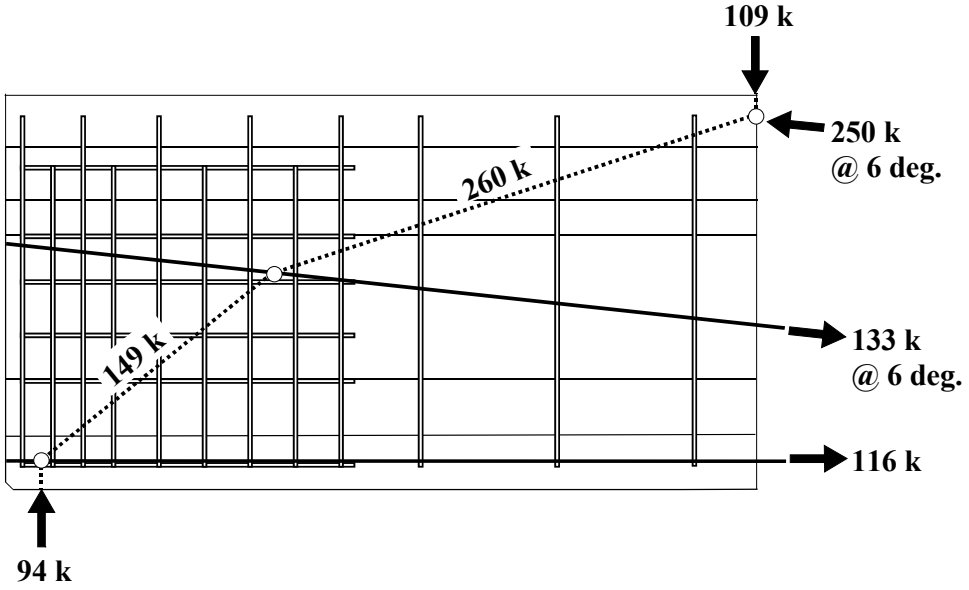

Figure 86 – STM a/d=2

Table 14 – Comparison of calculated shear capacity with experimental results.

a/d	Test	V_{EXP} (kip)	MCFT		STM		ACI	
			V_n (kip)	$\frac{V_{EXP}}{V_n}$	V_n (kip)	$\frac{V_{EXP}}{V_n}$	V_n (kip)	$\frac{V_{EXP}}{V_n}$
1	B1U1	344	211	1.63	125	2.75	268	1.28
2	B2U2	255	231	1.10	94	2.71	243	1.05
2	B4S2	242	231	1.05	94	2.57	243	0.99
3	B2U3	207	193	1.07	---	---	227	0.91
4	B1U4	180	181	0.99	---	---	181	0.99
4	B4U4	198	181	1.09	---	---	181	1.09
5	B3U5	158	167	0.95	---	---	160	0.99

Table 15 – Comparison of calculated moment capacity with experimental results.

a/d	Test	M_{EXP} (kip-ft)	M_n (kip-ft)	$\frac{M_{EXP}}{M_n}$
1	B1U1	1641	3072	0.53
2	B2U2	2144	3168	0.68
2	B4S2	2031	3168	0.64
3	B2U3	2644	3277	0.81
4	B1U4	3133	3389	0.92
4	B4U4	3420	3389	1.01
5	B3U5	3568	3511	1.02

5.10 Summary and Conclusions

Four existing 30-year old Type III bridge girders were removed from service and load tested. An approximately 28-in. wide section of the bridge deck was retained with each test girder. The bridge deck consisted of precast planks spanning between girders covered by a cast-in-place concrete topping slab.

Items of interest included the performance of the bridge deck as the compression flange, and the mode of failure corresponding to varying shear span-to-depth ratios (a/d). Tests were conducted using a/d ratios that ranged from 1.2 to 5.4.

After testing, concrete and steel samples were taken and tested to confirm material properties. These properties were used to calculate girder capacities as predicted by MCFT, Strut & Tie, and ACI models. Predictions were compared with the test results.

A strengthening scheme was applied to one test girder to increase the confinement of the strand development zone. The scheme consisted of steel tubes placed on each side of the bulb near the bearing, the tubes being compressed against the bottom bulb via two hand-tightened through bolts. Following are the salient findings from the research:

1. For a/d ratios of 3 or less, the failure mode was bond failure between the strands and the concrete, which was precipitated by the formation of cracks in the strand development zone.
2. For tests conducted with short a/d ratios, the formation of cracks in the strand development length caused the strands to slip, but also engaged the transverse and longitudinal mild steel reinforcement at the girder end. This provided a mild improvement in capacity and ductility beyond first strand slip.
3. Both tests conducted at an a/d ratio of 4 resulted in shear-compression failure. The change in failure mode between bond failure and shear-compression failure occurred at an a/d ratio between 3 and 4.
4. Flexural failure occurred in the single test conducted at an a/d ratio of 5. The transition to flexural controlled behavior occurred at an a/d ratio between 4 and 5.
5. The girder strengthened with the bolted tube steel apparatus exhibited better behavior than its unstrengthened counterpart did, but its capacity was not increased beyond that of the unstrengthened girder.
6. One of the a/d = 4 tests resulted in extensive crushing of the deck, which included buckling of the longitudinal bars. The crack aligned with one of the joints between the precast panels. The data, however, indicated that the panel system did not produce any negative effects compared to that of a cast-in-place deck.
7. For tests conducted with short a/d ratios, the actual failure mode (bond failure) was different from the mode assumed by the MCFT, Strut & Tie, and ACI models. The capacities predicted by the models, however, were still conservative for almost all cases when compared with the experimental results.

6 POST-TENSIONED GIRDERS

6.1 OBJECTIVE

Tests were conducted to determine the behavior and capacity of early (circa 1950's) post-tensioned concrete girders subjected to shear loading. The effects of different bearing conditions were also evaluated.

6.2 APPROACH

Three test girders were constructed using existing bridge plans. These girders were tested in three-point bending. Two of the girders were tested using a shear span-to-depth (a/d) ratio of 3.0. The final girder was tested using a shear span-to-depth (a/d) ratio of 2.0. The first two girders (a/d equal to 3.0) were tested with and without neoprene bearing pads to determine the effects of different bearing conditions on behavior and shear capacity.

6.3 BACKGROUND

The test girders were constructed to replicate an early form of prestressed girder used in Florida. These girders were precast, post-tensioned, I-girders with end blocks, used in simply supported short-span bridges. Each end of the girder would bear directly on the concrete pier cap with only a layer of tar paper separating the two. These girders are of particular interest because they have both parabolic and straight post-tensioning bars, and because they have no shear reinforcement. Mild steel reinforcement was provided only at the end blocks for approximately 3 ft from each end, presumably to protect against anchorage failure.

Jaeger and Bakht (1988) studied the bearing restraint in slab-on-girder bridges. Analytical models were created for steel-on-steel and steel-on-concrete bearings. The results indicated that the horizontal restraint provided by relatively new bearing pads reduced the total beam moments by 9%. It was also suggested that bearings permitting free movement of the girder not be provided for short spans bridges that can be designed for thermal effects and bearing restraint forces. Appropriate bearing restraints can provide a single span bridge with a substantial increase in capacity.

6.4 GIRDER DESIGN

The test girders were constructed to replicate a type of post-tensioned girder used in Florida bridge construction in the 1950's. The nearly 47-ft long test girders had four 1-in. diameter post-tensioning bars (Figure 87). This was a slight alteration from the existing plans, which called for 1.125-in. diameter bars. The post-tensioned steel bars used to construct the original bridge were not available, so commercially available Grade 150 bars (f_{pu} = 170ksi) were used to construct the test girders. Following the original girder plans, two PT bars were placed in a parabolic configuration with the other two PT bars placed at the bottom of the girder in a straight configuration (Figure 88). Each bar had a cross-sectional area of 0.85 square inches. Mild steel was placed in the end block for 34 in. at each end of the girder (Figure 89). The longitudinal steel in the end block extended just beyond the last stirrup. U-shaped bars were placed along the top of the girder to ensure composite action between the deck and the girder, but did not extend a sufficient distance into the girder to provide additional shear capacity. A 2-ft 4-in. wide by 7-in. thick deck was cast on the girder to simulate the 7-in. thick bridge deck used in the original design (Figure 90). The deck was reinforced with two layers of transverse #5 bars and longitudinal #4 bars.

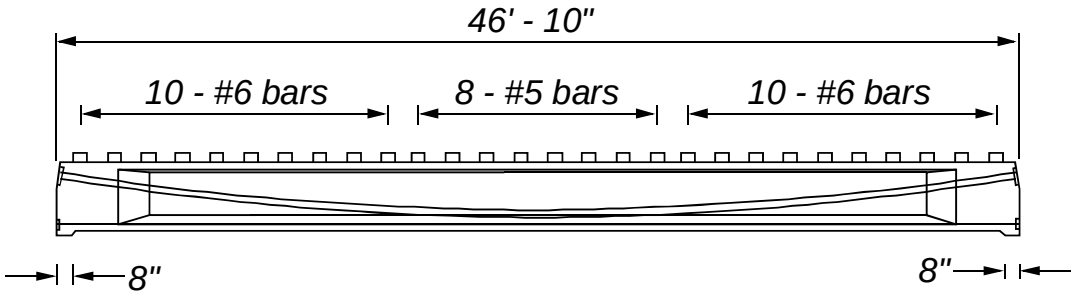

Figure 87 – Girder elevation

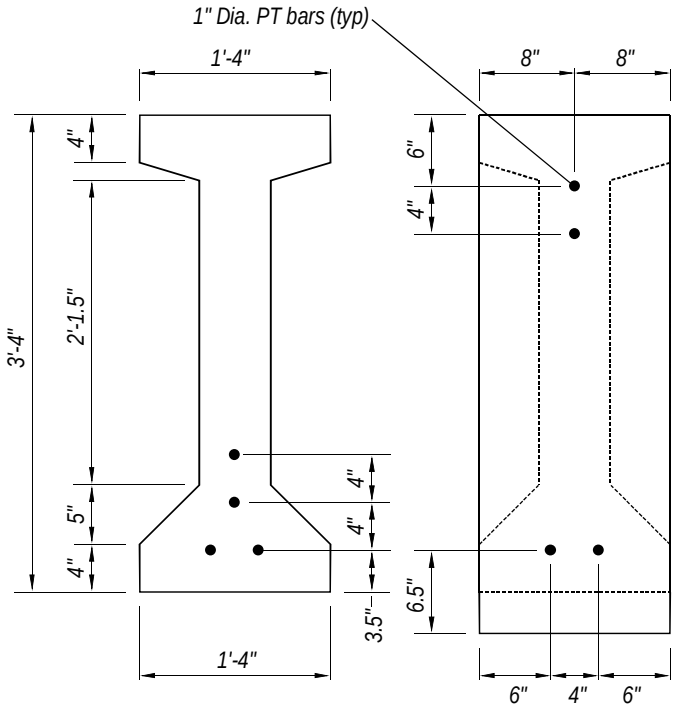

Figure 88 – Cross section and post-tensioning bars details at midspan (left) and end.

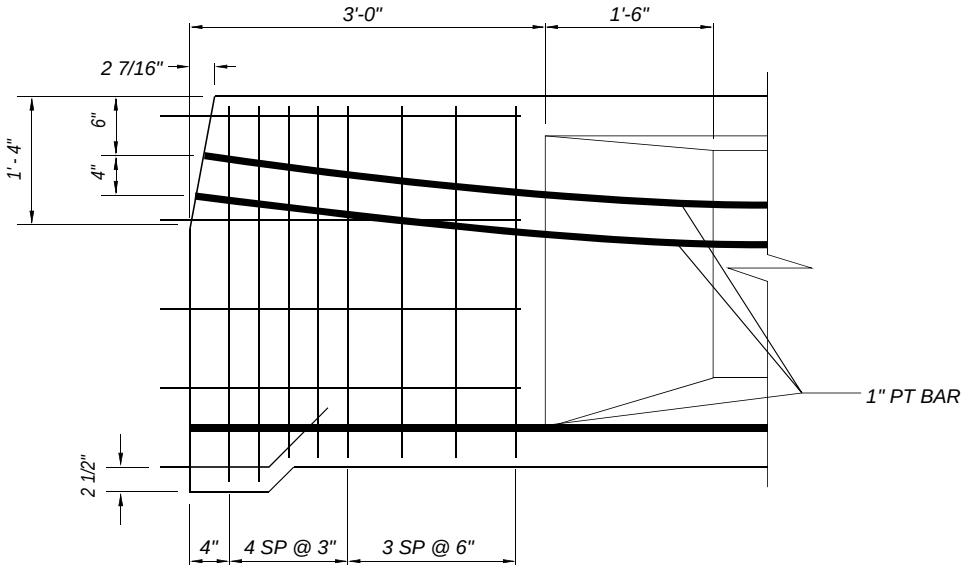

Figure 89 – End block geometry, reinforcement, and PT bar configuration

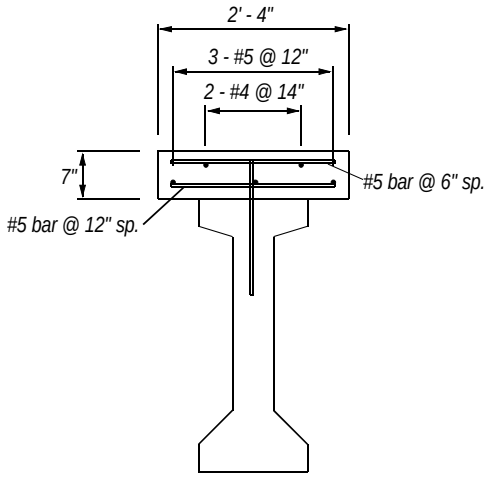

Figure 90 – Deck geometry and reinforcement.

6.5 GIRDER CONSTRUCTION

Girder construction was performed at the Florida Department of Transportation Structures laboratory in Tallahassee, Florida. Figure 91 shows the formwork that was fabricated using welded steel panels. The bottom form was placed on the top flange of a steel I-beam, which served as a base during construction. After erecting one side of the formwork, mild steel cages (Figure 92) were placed in the end block at each end of the girder. The cages were fastened to the formwork and rested on chairs to keep them in place while concrete was placed (Figure 93). Single post-tensioning bars were placed in 40-mm diameter galvanized steel duct (Figure 94). The ducts were fastened to the formwork and strapped to chairs at incremental points along the girder length to maintain the parabolic or straight configuration during casting. Plywood bulkheads were positioned to enclose the ends of the forms.

Figure 91 – Welded steel girder formwork

Figure 92 – End block reinforcement cage.

Figure 93 – End block reinforcement resting against a chair.

Figure 94 – Galvanized steel duct, HDPE duct at anchor plate, and HDPE grout tubes.

Anchorage bearing plates consisted of 1.75 in. x 6 in. x 10 in. steel plates with countersunk, conical-shaped holes (Figure 94). The PT bars were anchored with coarse threaded, dome-shaped nuts to maintain bar alignment relative to the anchor plate (Figure 95). After installing bulkheads and anchorages at each end of the girder, ducts were installed from anchorage to anchorage along with tubes and vents necessary to facilitate grouting. Strain gages were applied to the prestressing bars as detailed in the instrumentation section. Holes were cut into the duct near the gages to allow connecting wires to pass through and the bars were inserted into the duct. The holes were sealed and the wires were arranged to exit formwork (Figure 96). U-bars were tied to a longitudinal bar placed near the top of the girder (Figure 97). The opposite form was then installed with all-thread rod used as form ties. Final adjustments in duct and reinforcement were made after the form ties were in place.

Figure 95 – Bottom anchorage including anchor plate, conical nuts, PT bar, and grouting tubes.

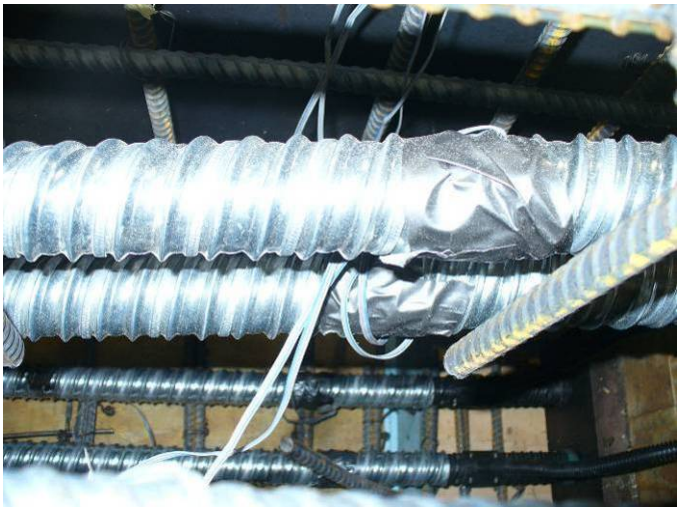

Figure 96 – Strain gages leads exiting duct.

Figure 97 – U-bar positioning.

Table 16 – Construction chronology.

Girder	Cast Girder	Post-Tension	Grout	Cast Deck	Load Test
C1	12-5-07	12-10-07	12-10-07	1-15-08	2-20-08
C2	1-30-08	2-5-08	2-5-08	3-26-08	4-30-08
C3	4-11-08	4-16-08	4-16-08	6-2-08	7-25-08

The girders were cast using ready mix concrete that was bucketed to the form using the laboratory crane (Figure 98). The water cement ratio was 0.41 and the aggregate was ¾ in. Florida Limestone. One truckload of concrete was needed for each girder. Twelve cylinders were taken to test concrete compressive strength. PT bars were stressed after cylinders tested at

3600 psi or greater, which was typically in 3 to 5 days. Stressing of PT bars is described in the following section.

The PT ducts were grouted immediately after stressing using a portland cement and water mixture with a water-to-cement ratio of 0.45. Mixing was done in a 5-gallon bucket and injected into the duct using a hand pump (Figure 99). Grout was injected from one end of the girder and was continuously pumped until the discharge at the opposite end indicated that air and water had been removed.

Figure 98 – Girder concrete placement.

Figure 99 – Grout injection using hand pump.

After grouting, the deck formwork and mild steel reinforcement were placed (Figure 100). As with the girder, concrete for the deck was delivered using the laboratory crane. The finished girder is shown in Figure 101.

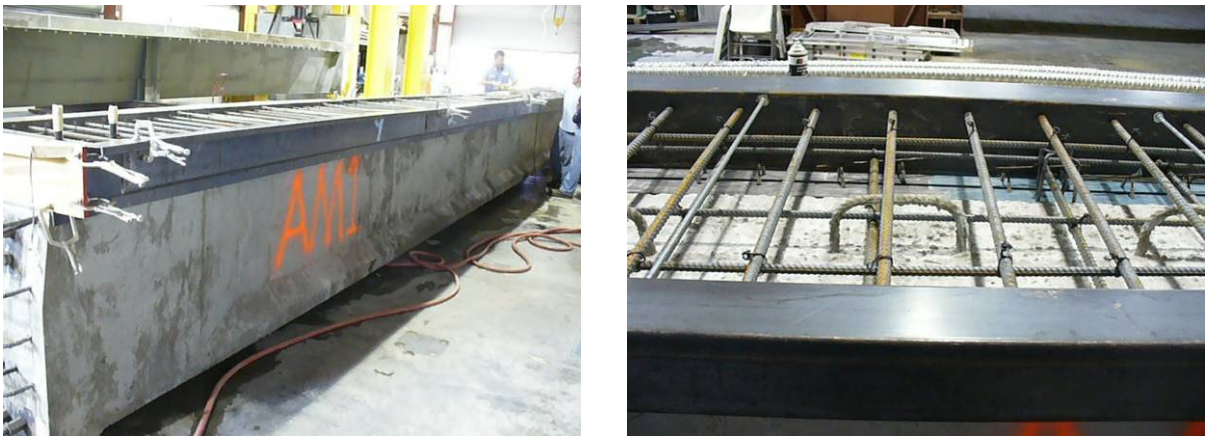

Figure 100 – Deck formwork and mild steel reinforcement.

Figure 101 – Finished girder and deck.

6.6 PRESTRESSING

6.6.1 PRESTRESSING APPLICATION

A 60 Mp Series 04 hydraulic jack was used to stress the PT bars (Figure 102). This jack is a 80 ton hydraulic actuator designed to stress a single threadbar. The jack was fitted with a

socket at the nose that fits the PT bar nut and can tighten just prior to release. The target prestress force for each bar was 93 kips and was measured with a load cell placed between the PT nut and jack. The PT bars were stressed with the jack located at the North end of the girder.

To avoid exceeding allowable concrete stresses, the bars were stressed in two stages in the following order: 2,3,1,4 (Figure 103). The first stage consisted of stressing each PT bar to 50% of the desired final stress in the order indicated. The stressing sequence was then repeated to reach the final desired stress. Table 17 shows the jacking force at each stage for each girder as measured by the load cell.

Figure 102 – Hydraulic jack used to stress PT bars.

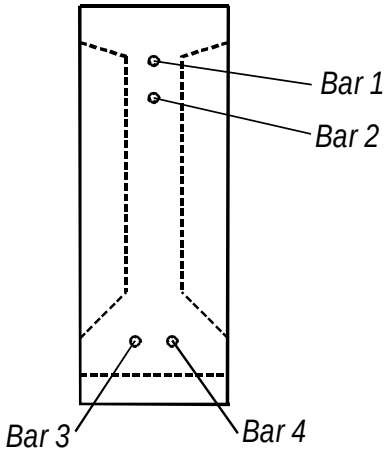

Figure 103 – PT bar designation for C girders.

Table 17 – Jacking force measured with load cell.

Stage	Jacking Force (kip)		
	C1	C2	C3
1	46.7	45.7	46.7
2	94.5	93.4	93.5

6.6.2 INSTRUMENTATION

Strain gages were applied to the PT bars to measure prestress losses during and after stressing, and stresses in the bars during load testing. Tandem gages were placed on the bars near each end of the girder (Figure 104). The gages were placed in diametrically opposed positions on the bar to account for possible bending stresses in the bar. Stresses were calculated by multiplying the measured strains by Young's modulus. Some of the gages were damaged during installation and prestressing of the PT bars. Table 18 shows the surviving strain gages for C1 and C2. None of the gages in C3 survived or provided data that could be used to measure stresses.

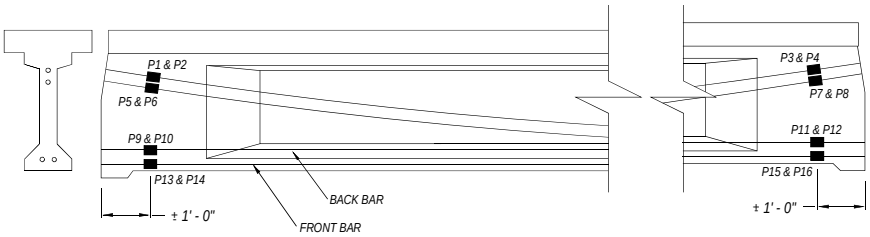

Figure 104 – Location of gages for C girders.

Table 18 – Working P-gages for each C girder.

C1	C2
P11	P3
P12	P9
P14	P10
P15	P13
P16	P14

6.6.3 RESULTS – ANCHORAGE SET

Measurements were taken during post-tensioning to determine anchorage set, elastic losses, friction losses and early creep losses. Anchorage set in prestressing bar anchorages occur when the bar is released and the anchor nut settles against the anchor plate. Further set occurs as

the anchorage components deform during transfer. As the PT bar was being stressed, the anchor nut was tightened to minimize the take up when the bar was released.

Anchorage set can be measured by observing the change in strain as the prestress is transferred. Strain data from the gages located nearest the stressing end of the girder will more accurately show anchorage set because the strain gages at the dead end will be affected by friction losses from wobble or drape. Figure 105 and Figure 106 show a time trace of the stress in each PT bar during prestressing of girder C1. The stress was calculated from strain data using a Young's modulus of 29,700 ksi (as recommended by the bar manufacturer). The plots display only the data from strain gages that were operating properly and include the average of each tandem pair of strain gages when both were operating correctly and single readings when only one of the gages was working properly. The plots illustrate the staging used to stress the PT bars. Each PT bar was initially stressed to approximately half of the target prestress, followed by another round of prestressing to reach the target prestress.

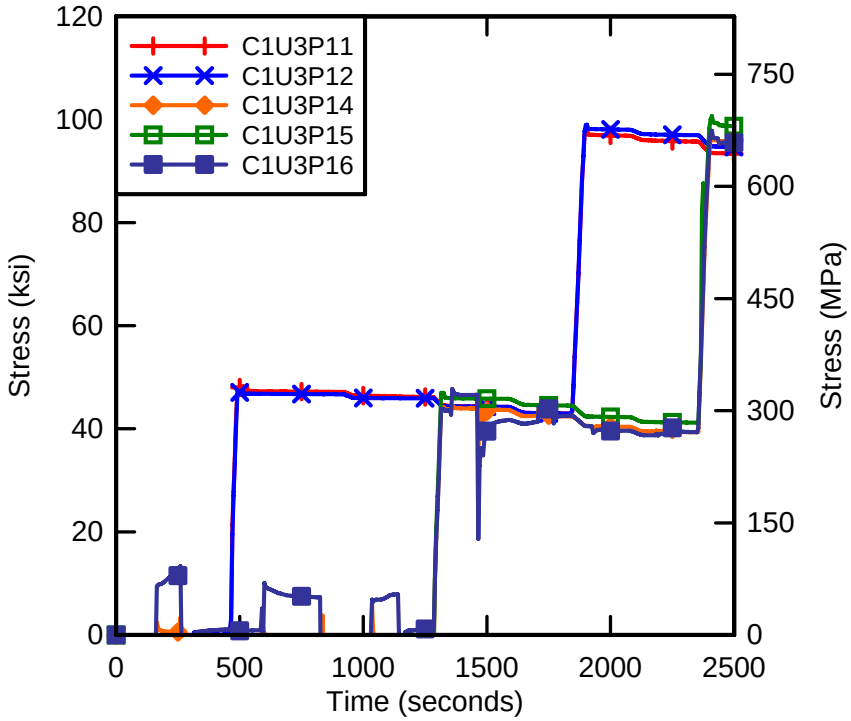

Figure 105 – PT bar stress during post-tensioning of girder C1.

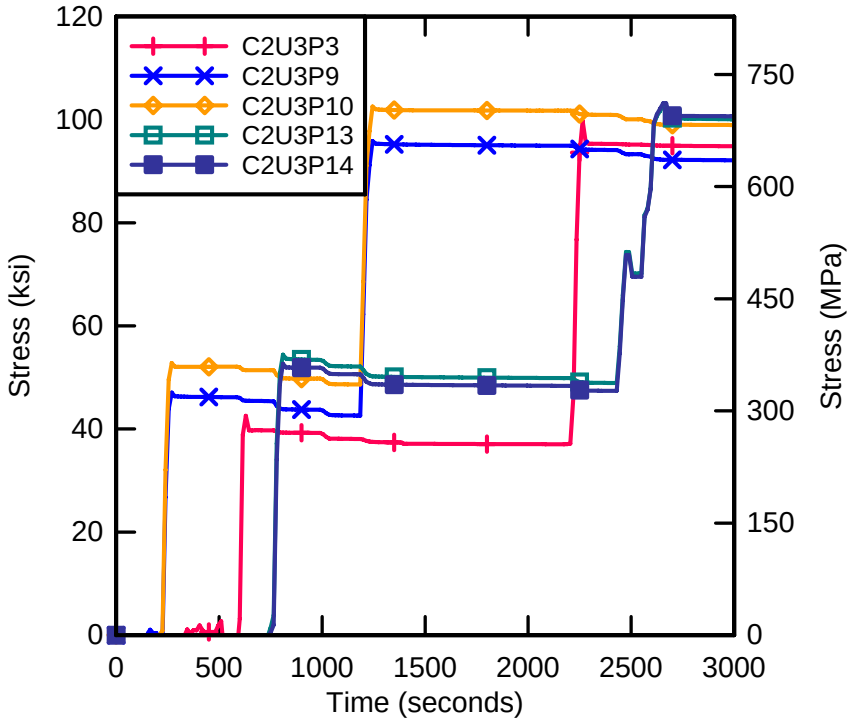

Figure 106 – PT bar stress during post-tensioning of girder C2.

Figure 107 illustrates how elastic losses and anchorage set were determined from the strains measured in the bars during post-tensioning. The graph shows the plot of the average strains from two tandem strain gages converted to stress. As noted on the plot, anchorage set was the immediate reduction in stress as the prestress force was transferred from the jack to the anchorage. The three subsequent sharp drops in stress are the elastic losses caused by stressing each of the adjacent PT bars. The shallower downward trends indicate initial creep losses.

The jacking stresses and loss in stress due to anchorage set are summarized in Table 19. The anchorage sets for girder C1 bars 3 and 4, and girder C2 bar 1 were measured using strain gages at the stressing end of the girder. Anchorage set losses for bars 3 and 4 in girder C2 were measured using the strain gages at the dead end. In addition, Table 17 also shows the prestress loss as a percentage of the jacking stress for both stages. Anchorage set losses for the straight PT bars (3 and 4) were consistently in the range of 2% regardless of the jacking stress. The parabolic PT bar, however, had anchorage set losses 2 to 3 times this value. This may be due to the difficulty in maintaining proper alignment of the bar and nut with the anchor plate when the anchor plate is not perpendicular to the girder axis.

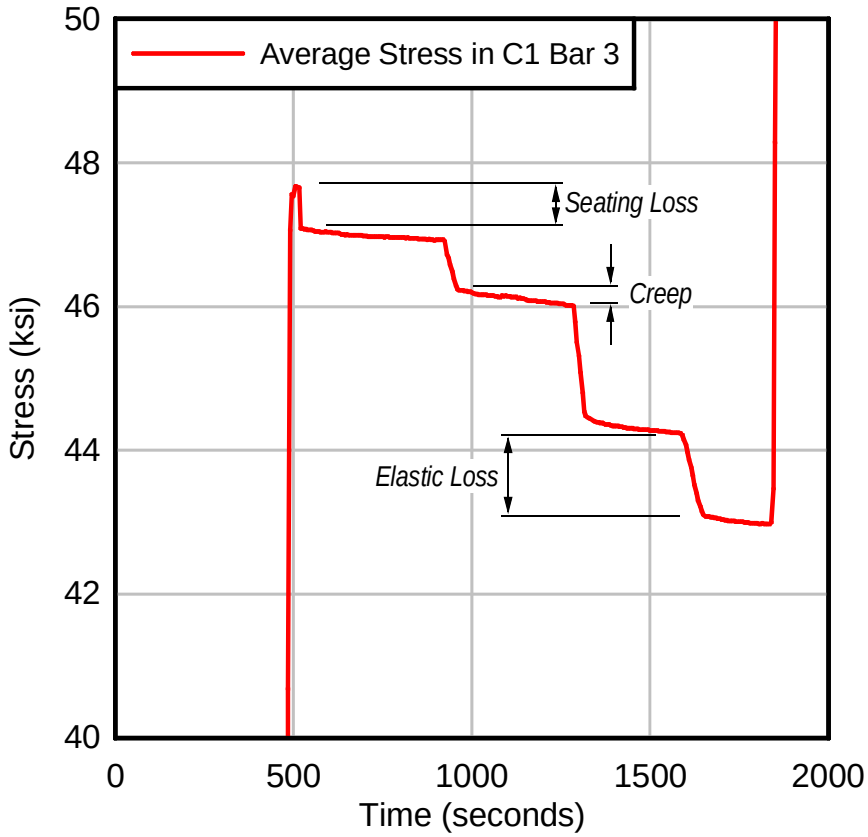

Figure 107 – Measurement of anchorage set, short term creep, and elastic loss.

Table 19 – Measured changes in stress due to anchorage set.

Bar	Stage	Jacking Stress (ksi)		Anchorage Set Loss (ksi)		Prestress Loss (%)	
		C1	C2	C1	C2	C1	C2
1	1	---	44.6	---	3.13	---	7.3
	2	---	103.9	---	4.46	---	4.5
3	1	50.6	52.0	1.0	0.74	2.1	1.5
	2	104	103	1.3	0.47	1.3	0.5
4	1	50.0	55.8	1.4	1.50	2.4	2.8
	2	107	107	2.2	2.46	2.1	2.4

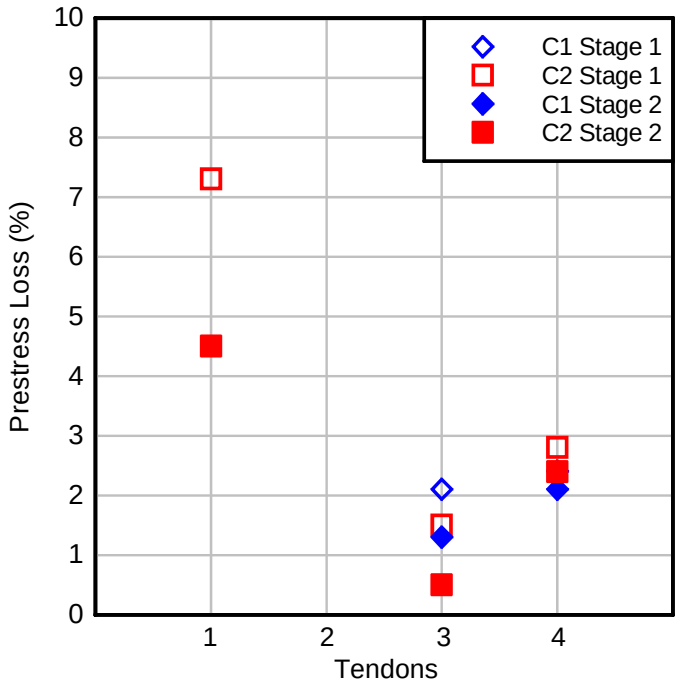

Figure 108 – Summary of anchorage sets.

The anchorage set at the stressing end anchorage was calculated using this sudden change in strain and multiplying it by the length of the PT bars, 46 ft-10 in. and are presented in Table 20. Typical anchorage set can be about 0.03 in. but varies depending on the type of anchorage (Lin and Burns 1981).

Table 20 – Measured anchorage set.

PT bar	Stage 1 (in.)		Stage 2 (in.)	
	C1	C2	C1	C2
1	---	0.06	---	0.09
3	0.02	0.02	0.02	0.01
4	0.03	0.03	0.04	0.05

Table 21 shows the elastic losses due to stressing of adjacent PT bars. The change in strain for each PT bar was measured as each of the following bars in the sequence was stressed. For example, during stage 1 stressing of bar 4 in girder C1, the measured decrease in stress of bar 3 was 1.8 ksi. The attendant loss of prestress was 3.9% based on the stress in bar three just prior to stressing bar four. In general, the highest losses were observed during the stressing (jacking)

of immediately adjacent PT bars. For instance, the loss in stress in bar 3 was greatest when bar 4 was being jacked.

Using the LRFD method for calculating losses due to elastic shortening, a loss of 2.6 ksi was predicted for the first and second stage. A comparison could not be made due to a lack of data.

Table 21 – Elastic losses for C girders.

PT bar	Jacking PT bar	Stage 1				Stage 2			
		C1		C2		C1		C2	
		Δf (ksi)	Loss (%)	Δf (ksi)	Loss (%)	Δf (ksi)	Loss (%)	Δf (ksi)	Loss (%)
1	4	---	---	0.51	1.3	---	---	0.46	0.5
3	1	0.9	2.0	0.81	1.7	1.1	1.1	1.21	1.2
3	4	1.8	3.9	1.75	3.4	2.4	2.4	1.91	2.0

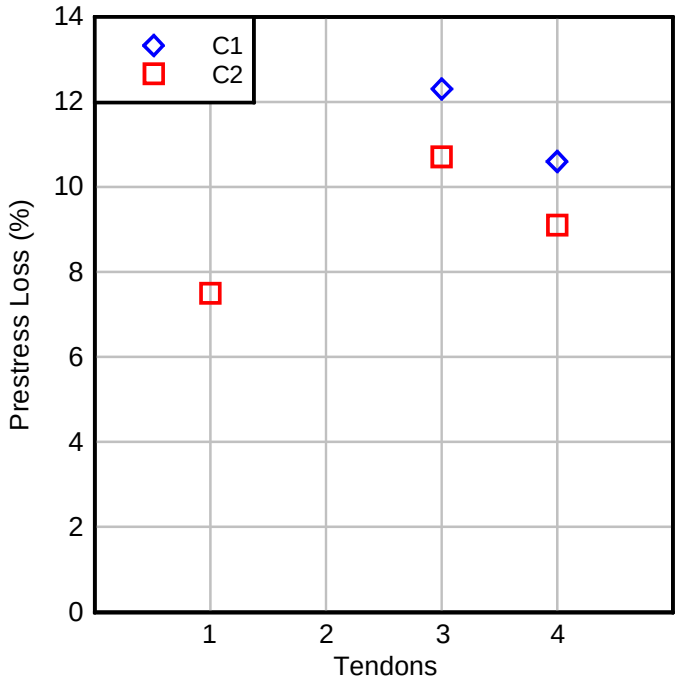

Figure 109 – Summary of elastic losses.

Wobble in a straight duct will generate friction, which will cause a reduction in the post-tensioning force as the distance from the jacking location increases. The wobble coefficient was calculated for PT bar 4 in C1 by determining the difference between the bar stress (using the strain gages) at the jacking end and dead end of the PT bar. A wobble coefficient of 0.0007 per

ft was then back-calculated. ACI gives a range for the wobble coefficient of 0.0001 to 0.0006 for high-strength bars grouted in metal sheathing.

To observe time-dependent losses, PT bar stresses in C2 were measured for approximately 2.5 days after stressing (Figure 110). The losses due to creep and shrinkage effects were 6.3 and 5.6 percent (See Table 22) for this short period of measurement. For comparison, a loss of 1.7% was obtained using the LRFD method for calculating shrinkage and creep losses.

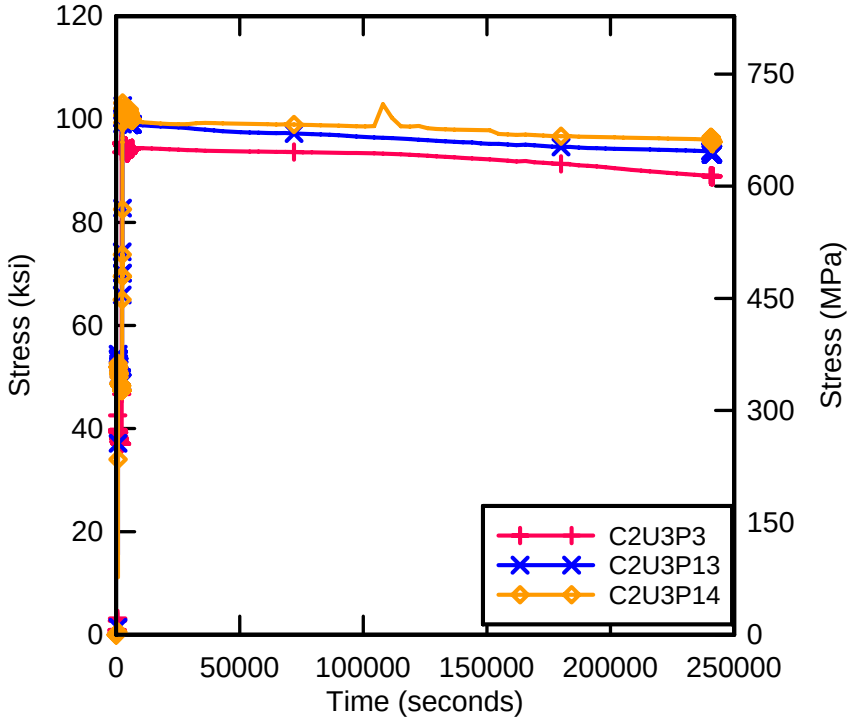

Figure 110 – Time dependent strains in girder C2.

Table 22 – Time-dependent losses in C2.

PT bar	Δf (ksi)	$\%_{loss}$
1	5.99	6.3
4	5.52	5.6

6.7 MATERIAL PROPERTIES

Cylinder tests were conducted to determine the concrete compressive strength of the girder and the deck. The average strengths for the girder and deck are presented in Table 23. Samples of the post-tensioning bars were also taken and tested, their average material properties are presented in Table 24.

Table 23 – Average cylinder strength (ksi).

Girder	Girder	Deck
C1	7.96	3.34
C2	8.64	5.47
C3	8.64	4.89

Table 24 – PT bar material properties.

EUL @ 0.50% Stress (ksi)	140.2
Tensile Strength (ksi)	169.9
Elongation (%)	7.8

6.8 TEST SETUP AND PROCEDURES

Three tests were conducted using a three point loading scheme shown in Figure 111. Two tests were conducted using a shear span to depth (a/d) ratio of 3.0. One of these tests (C1U3) was set up with the girder bearing directly on the concrete pedestal support (Figure 112). The second test (C2U3) was set up with the girder bearing on 2-in. thick neoprene pads. Bearing conditions were varied to observe their effects on girder behavior. The third girder (C3U2) was loaded at a/d = 2.0 and was supported on neoprene pads. This test was conducted to evaluate the girder shear behavior with a short shear span and with no shear reinforcement.

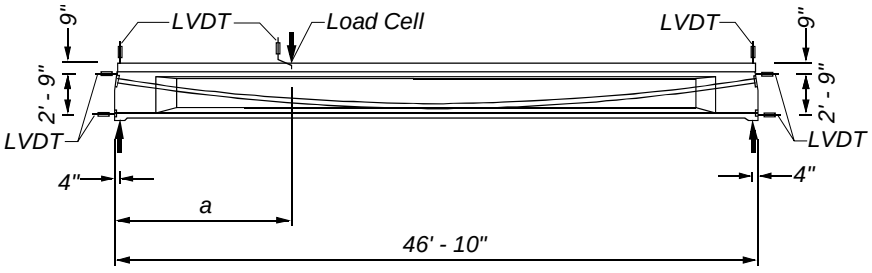

Figure 111 – Test setup and instrumentation for C girders.

Figure 112 – Support Conditions, C1U3 (Left) and C2U3 (Right)

The load was applied by an actuator through a 1.5-in. thick x 10 in. x 20 in. (20 in. dimension perpendicular to length of girder) reinforced neoprene bearing pad at a loading rate of 0.25 kips/second. For tests with neoprene bearing pads at the supports, the pad dimensions were: 2 in. x 8 in. x 16 in. (16-in. dimension perpendicular to length of girder). A load cell was used to measure load under the actuator. Displacements were measured at the load point and each of the supports. Horizontal movement of the girder was measured at the top and bottom. The detailed instrumentation for each test is shown in Figure 113 through Figure 115. Strain was measured with 60-mm strain rosettes and strain gages. For test C2U3, five 30-mm strain gages were used in the deck and top flange of the girder in addition to the 60-mm gages. Test C3U2 used sixteen 30-mm strain gages in the top flange and deck of the girder in addition to the 60-mm gages.

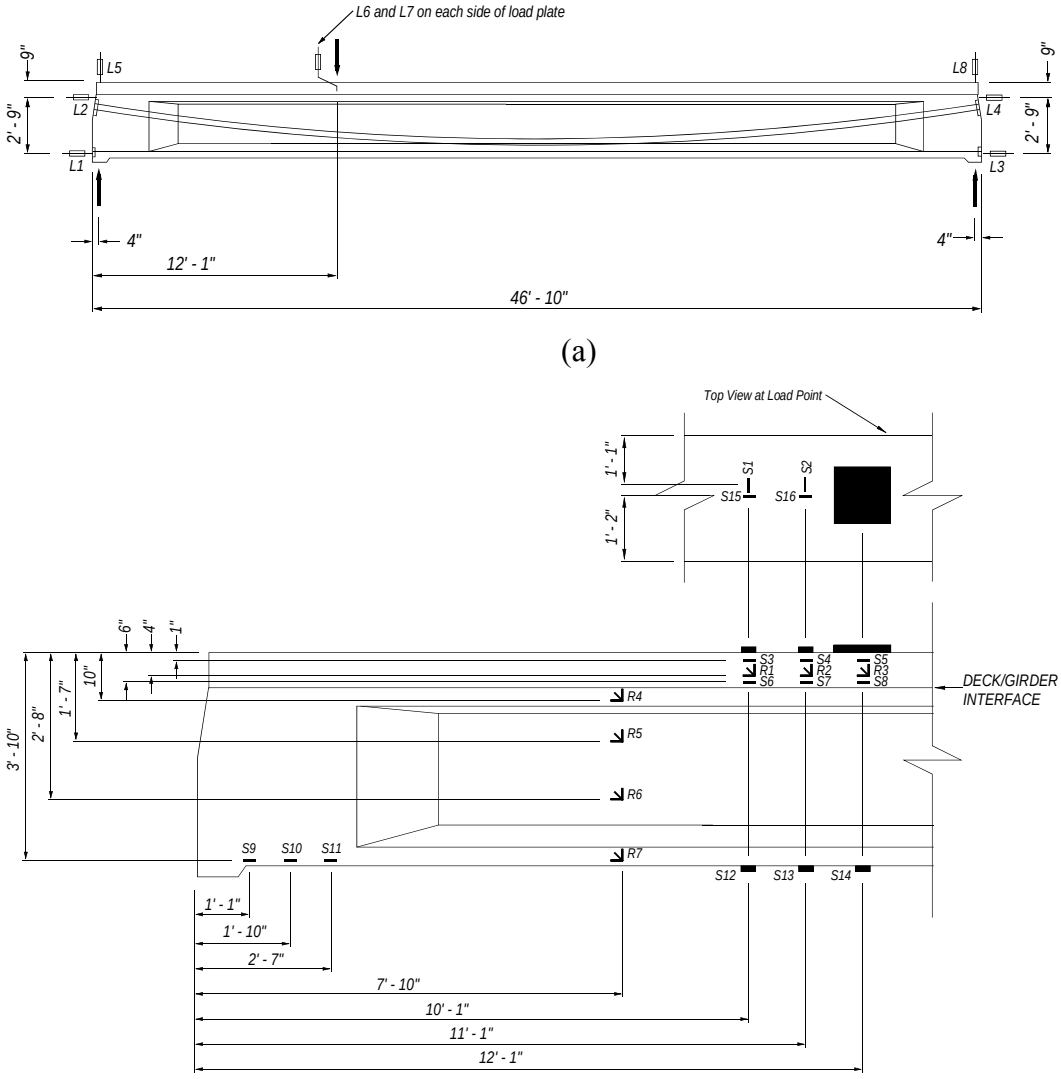

Figure 113 – Test C1U3 (a) setup (b) instrumentation.

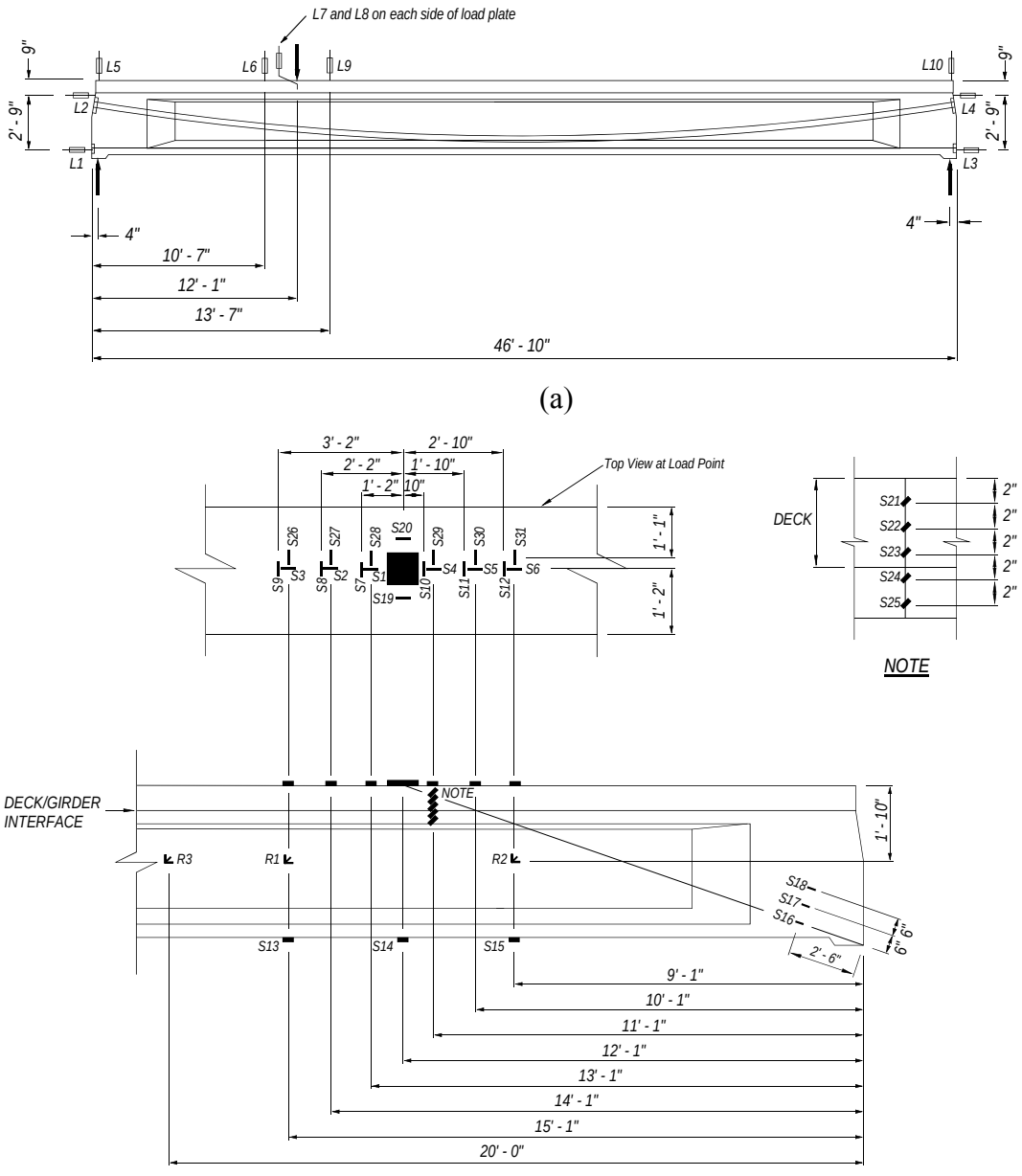

Figure 114 – Test C2U3 (a) setup (b) instrumentation.

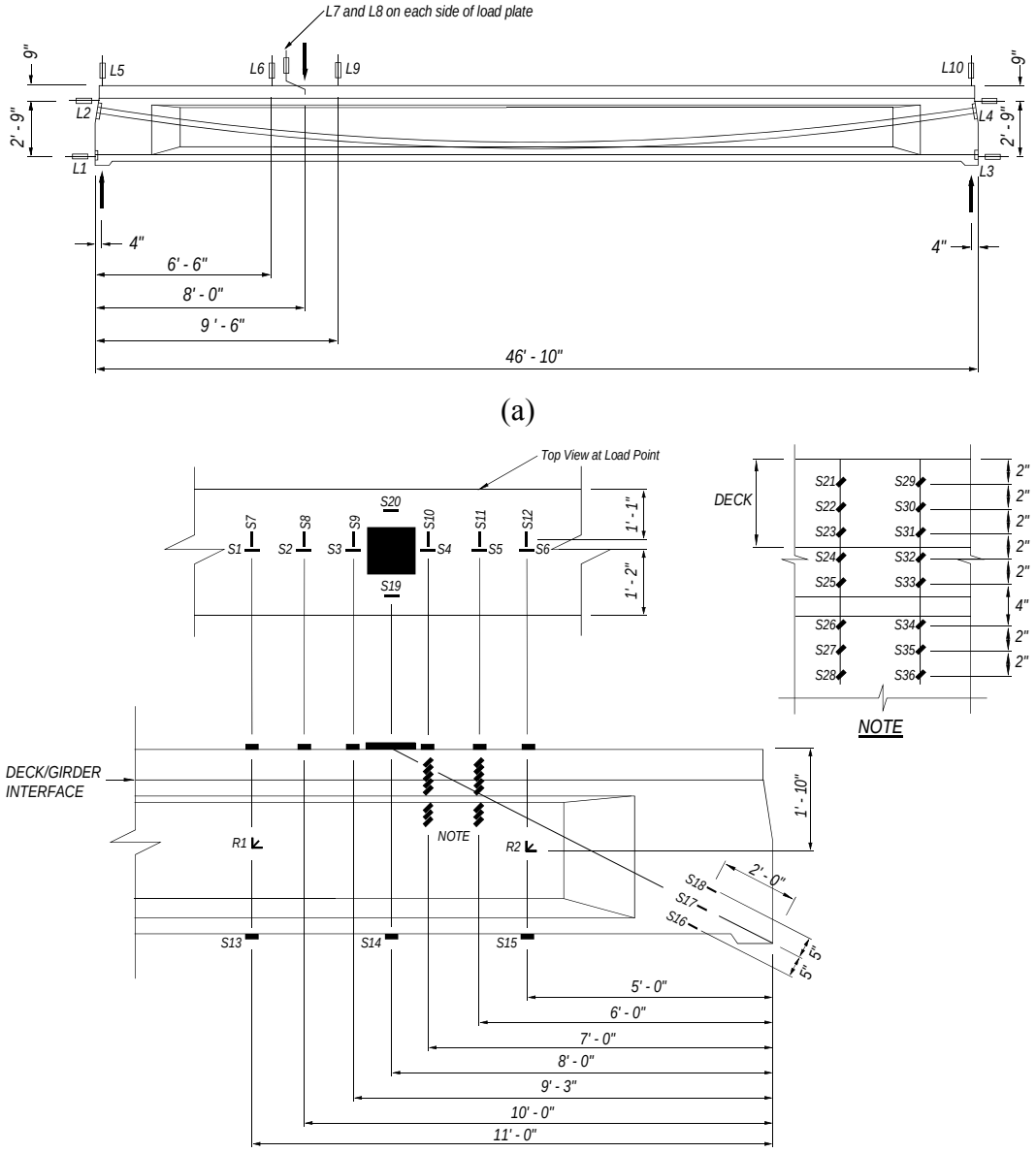

Figure 115 – Test C3U2 (a) setup (b) instrumentation.

6.9 RESULTS AND DISCUSSION – SHEAR TESTS

6.9.1 C1U3

Figure 116 shows the superimposed shear vs. displacement plot for C1U3. This plot indicates linear-elastic behavior of the girder up to a shear of 74 kips, the shear at which the first flexural crack occurred. Data from gage S14, which was located on the bottom of the girder at the load point, indicates cracking at a shear of 74 kips (Figure 117). Figure 117 shows that the

flexural crack formed at a tensile strain of nearly 400 microstrain. Figure 118 shows the location of the first crack. As loading continued, further flexure cracks formed under the load point, resulting in a decrease in stiffness. The girder reached its maximum capacity at a shear of 135 kips where a flexure-compression failure occurred in the deck under the load point. Figure 118 shows the final crack pattern.

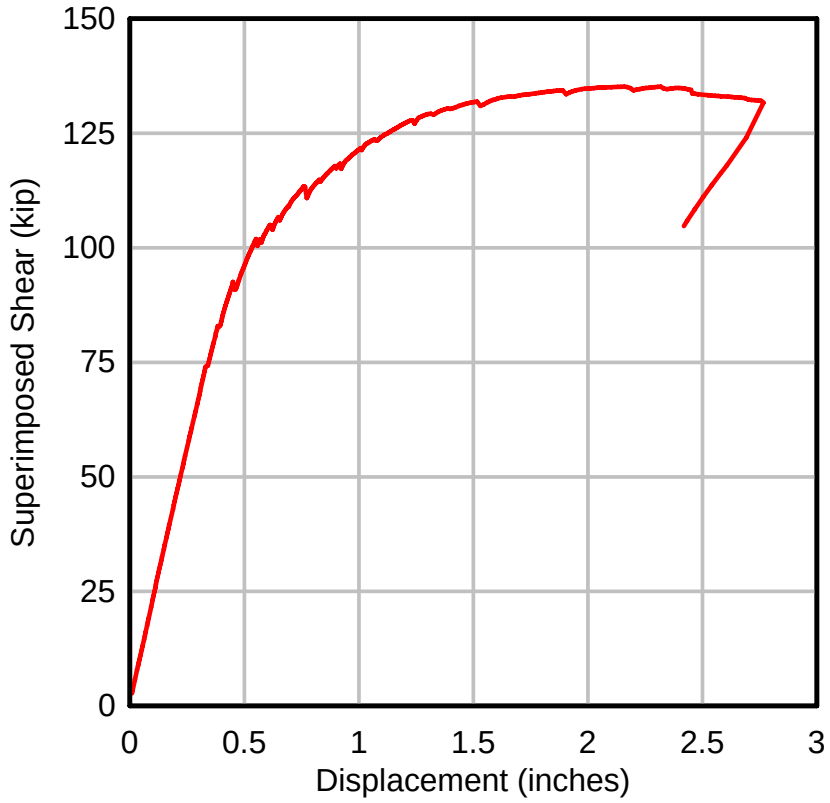

Figure 116 – Superimposed shear vs. displacement for C1U3.

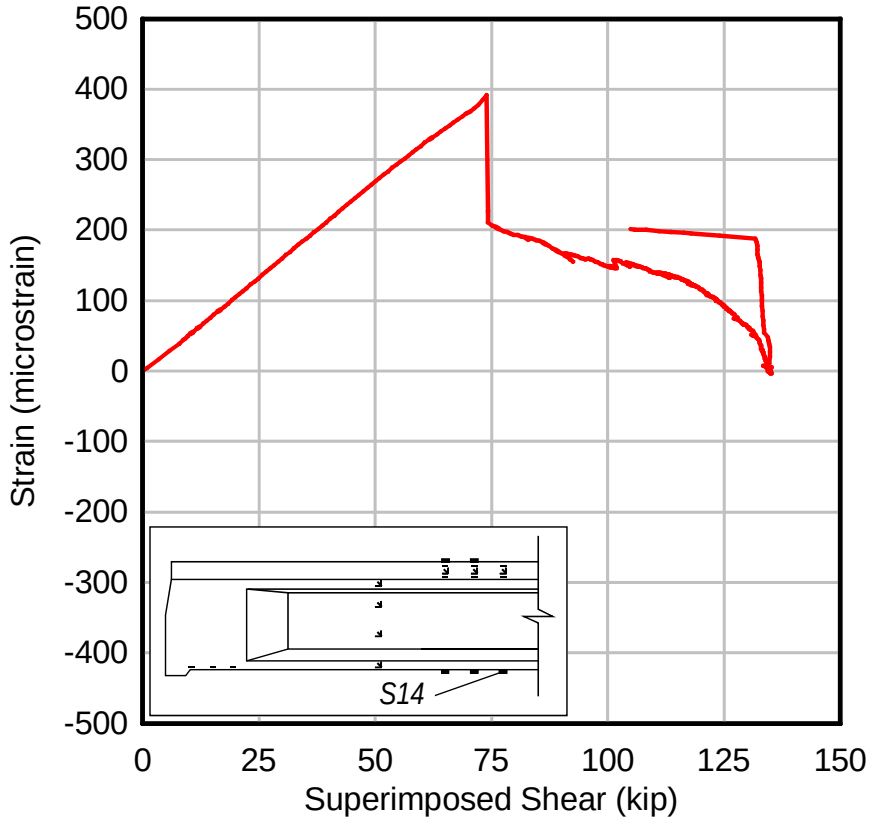

Figure 117 – C1U3S14 plot.

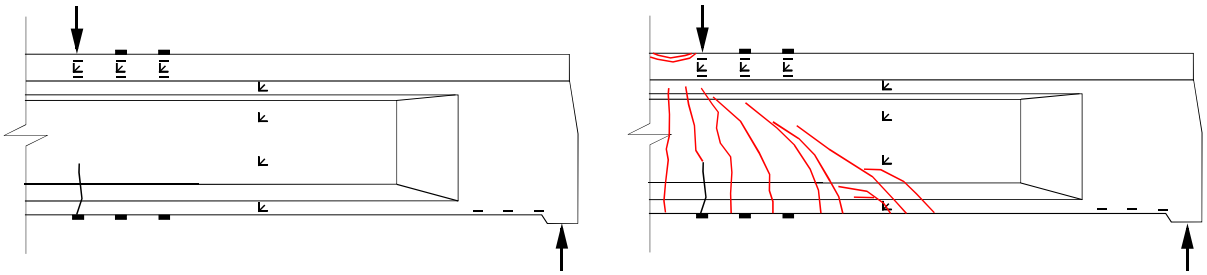

Figure 118 – First and final crack pattern for C1U3.

6.9.2 C2U3

The initial behavior of C2U3 was similar to C1U3 up to and including cracking. Figure 119 shows linear elastic behavior up to a load of 74 kips where the first flexural crack occurred. The crack was detected by gage S14, which was located on the girder bottom under the load point (Figure 120). Although the initial strain at S14 was linear, a soften behavior occurred as the shear approach the cracking shear of 74 kips. At this shear, S14 reported a spike in strain. Figure 121 shows the location of the first crack.

Figure 119 shows a decrease in stiffness at a shear of approximately 92 kips as indicated by the decrease in the slope of the load displacement curve. As loading continued, the curve eventually reached a plateau, indicating yielding of the PT bars. The girder reached its maximum capacity at a shear of 127 kips where a flexure-compression failure occurred in the deck under the load point. Figure 121 shows the final crack pattern.

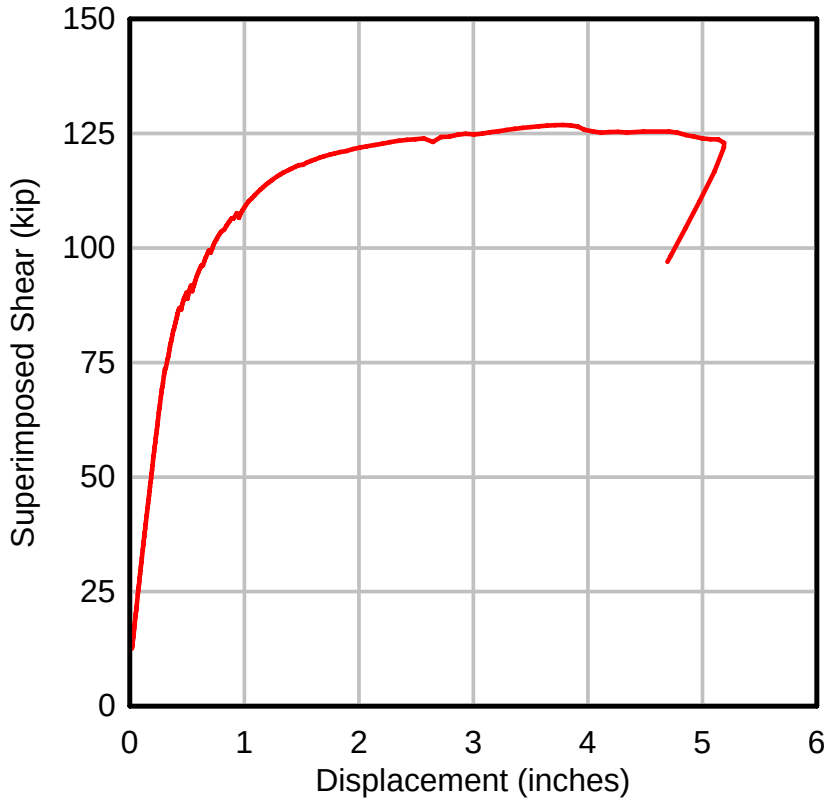

Figure 119 – Superimposed shear vs. displacement for C2U3.

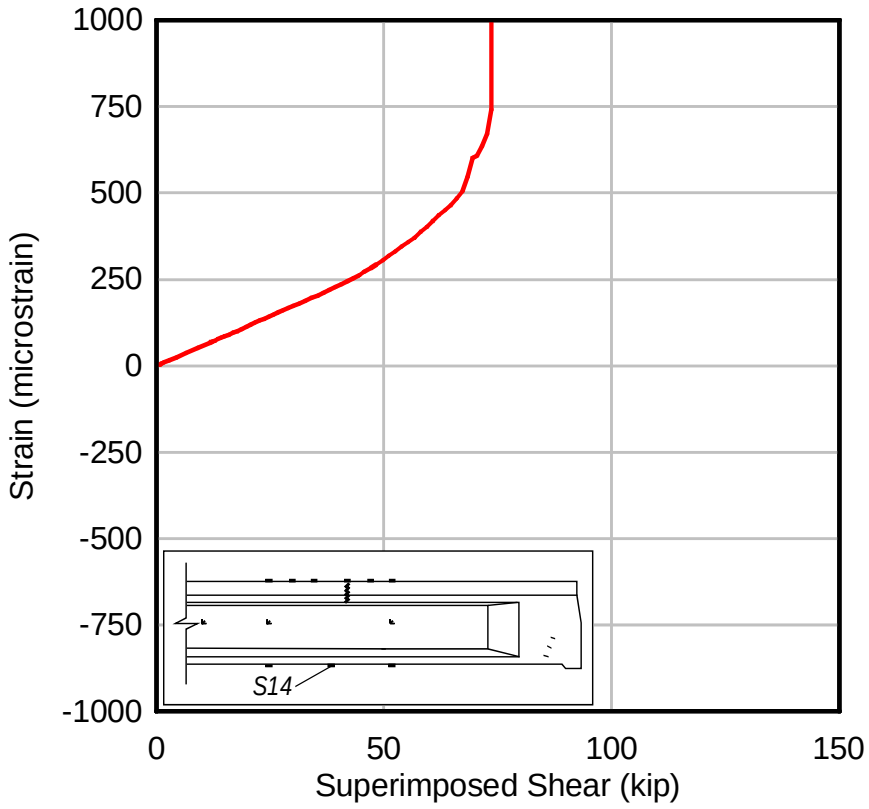

Figure 120 – C2U3S14 plot.

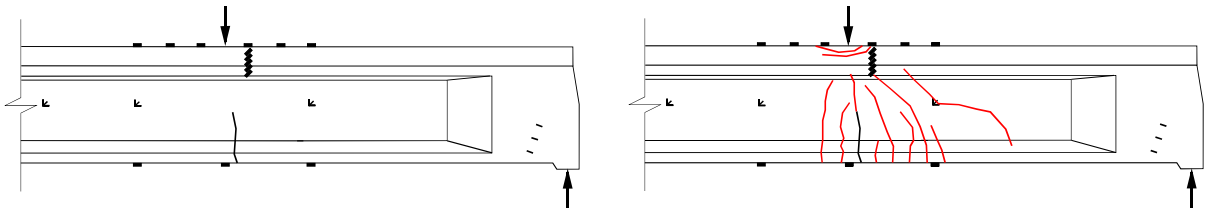

Figure 121 – First and final crack pattern for C2U3.

6.9.3 C3U2

Figure 122 shows the superimposed shear vs. displacement plot for test C3U2. The plot indicates linear elastic behavior up to a shear of 87 kips. The initial crack (Figure 123) was visually observed at this load and was confirmed by data from strain gage S14 (Figure 124). As demonstrated by the abrupt changes in strain shown in Figure 124, additional cracks formed at 109 kips (S13) and at 156 kips (S15). The shear displacement curve (Figure 122) shows a reduction in stiffness over this same range of loads. At a shear of 156 kips, a large crack was observed to have formed, which extended from the tension face below the end block up into the

web (Figure 125). At a displacement of approximately 1.5 in., the curve had reached a plateau with little increase in shear relative to displacement, indicating that the PT bars had yielded.

Cracks were observed around the anchor plate of the parabolic PT bars at a shear of 187 kips (Figure 126). The test was terminated at this point to avoid an explosive failure. The final crack pattern can be seen in Figure 123. The peak load measured during testing was 187 kips. The final failure mode, however, was not determined because the test was terminated prior to reaching the peak capacity.

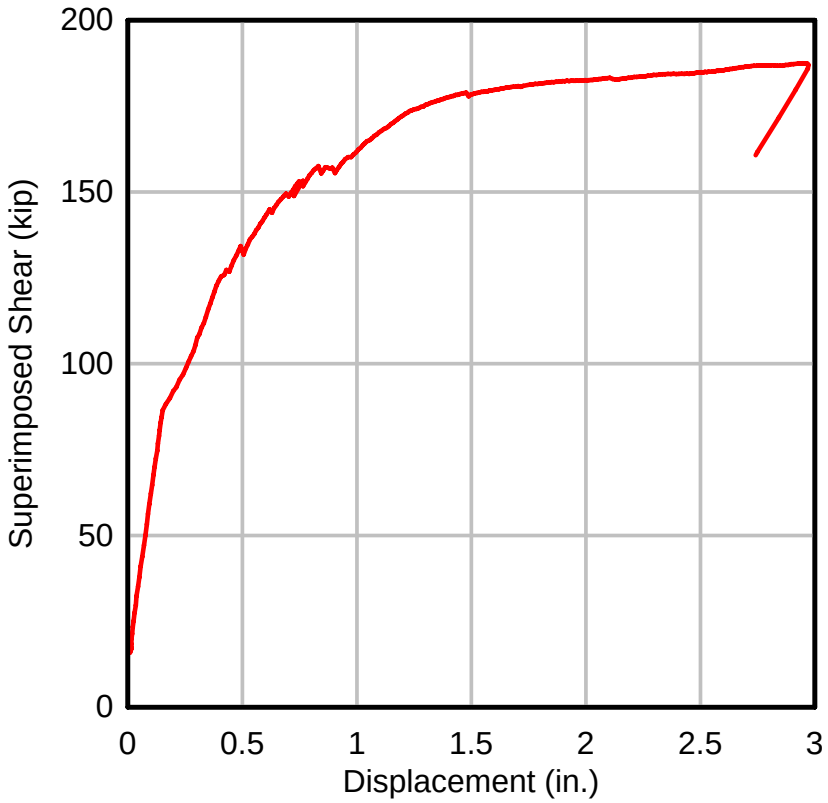

Figure 122 – Superimposed shear vs. displacement for C3U2.

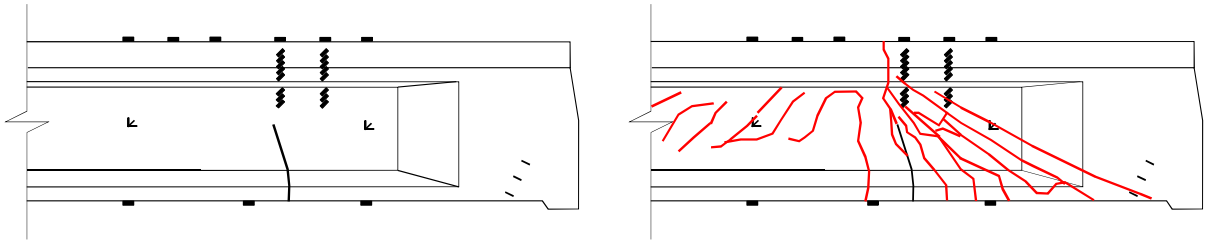

Figure 123 – First and final crack pattern for C3U2.

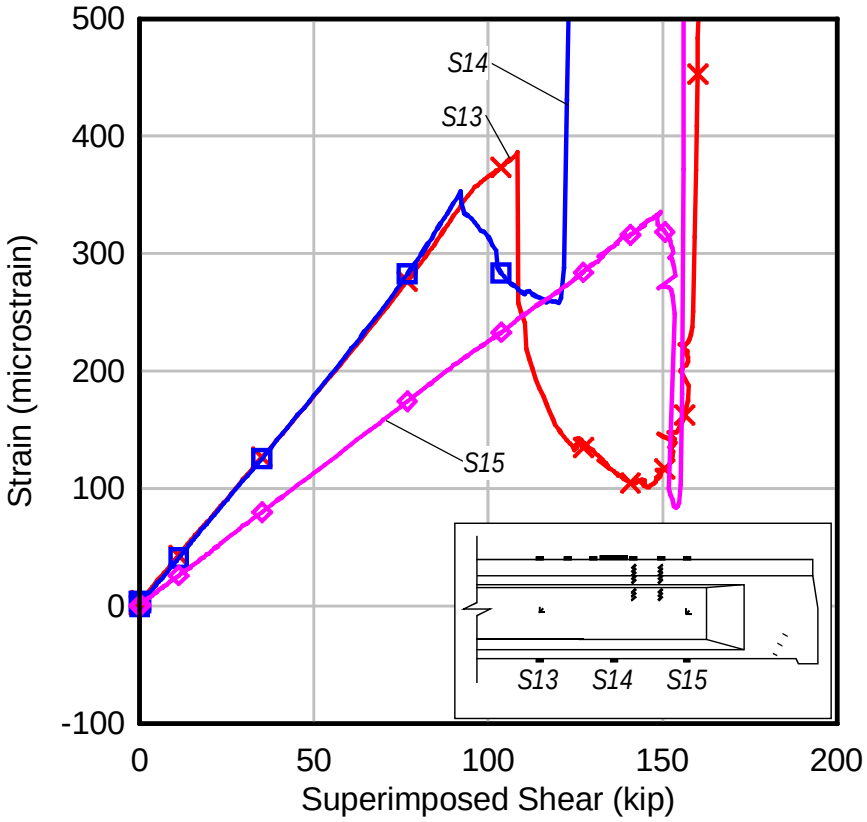

Figure 124 – Strain gages S13, S14, and S15.

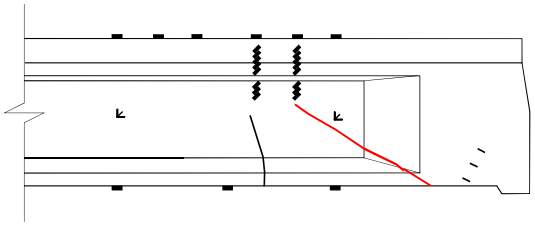

Figure 125 – First crack and crack occurring at 156 kips

Figure 126 – Cracks around PT anchorage.

6.10 Effect of Support Conditions on Behavior

Tests C1U3 and C2U3 were conducted with a shear span to depth ratio (a/d) of 3.0. The first test, C1U3, used support conditions shown in Figure 127 in which the girder was bearing directly on concrete. The second test, C2U3, used neoprene pads under each of the supports (Figure 128). Both tests had the same loading scheme and loading rate, the support conditions were the only variable between the two tests. The intent of the test was to explore the difference in behavior between the two support conditions. This information will be useful in the interpretation of data from future bridge tests.

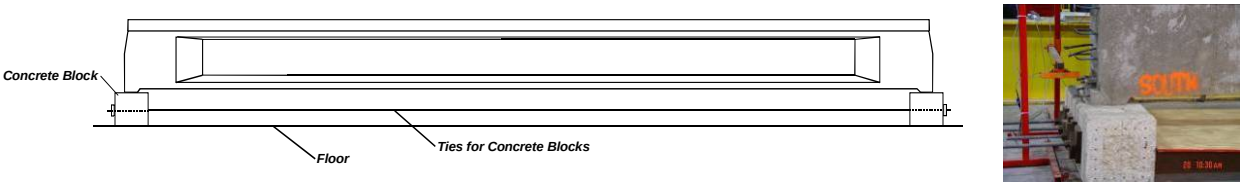

(a) (b)

Figure 127 – Support condition for C1U3.

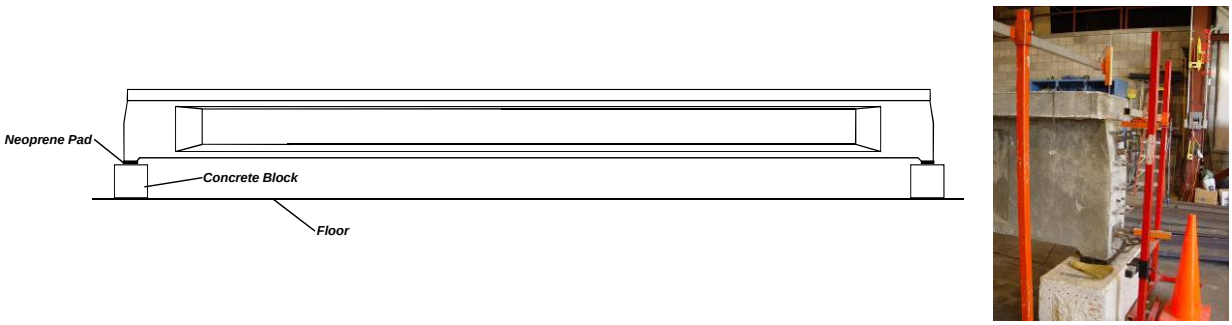

(a) (b)

Figure 128 – Support condition for C2U3.

Beams are typically modeled assuming that the beam is supported by a pin and roller, which offers no resistance to elongation of the bottom of the beam. Conversely, arches are modeled with pinned supports, which provide an infinitely stiff support and ensure pure arching action. These modeling choices are made with the understanding that the actual conditions are situated somewhere between these bounds. Shallow arches require very stiff support conditions to ensure pure compression. Furthermore, very small transverse movements at the support will shift the behavior from arching to flexure.

To estimate the magnitude of load that must be resisted by the supports in the laboratory, the girder specimen was modeled using membrane elements as shown in Figure 129. A rectangular cross-section was used with a thickness of 17 in., which is the average thickness of the specimen. Each element was 5.8-ft long by 3.92-ft deep. A modulus of elasticity of 4030 ksi was used, which corresponds to a compressive strength of 5 ksi. The transverse and vertical reactions for a unit load required to maintain pure arching are shown in Figure 129.

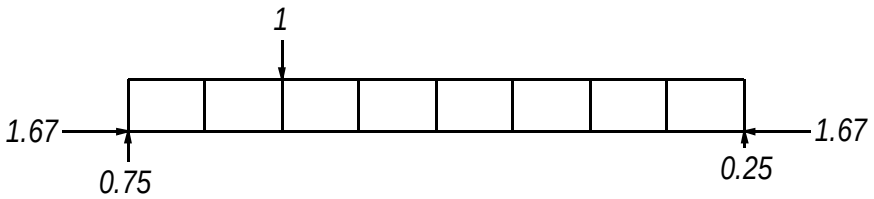

Figure 129 – Computer model of girder C at an a/d ratio of 3.0.

While pure arching was not expected to occur using the tested support conditions, some arching effect was anticipated. Figure 130 shows the expected restraint provided by the supports used in the testing. For the direct bearing condition, the transverse reaction is expected to be a

function of the frictional force generated by the direct concrete contact. For the condition with neoprene bearing pads, the reaction is expected to be a function of the neoprene shear stiffness and the transverse displacement of the bottom of the girder. Figure 131 defines the transverse support displacement.

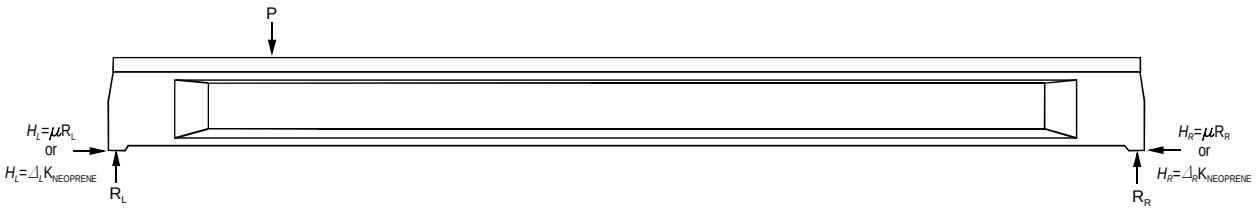

Figure 130 – Horizontal reactions generated by the varying support conditions.

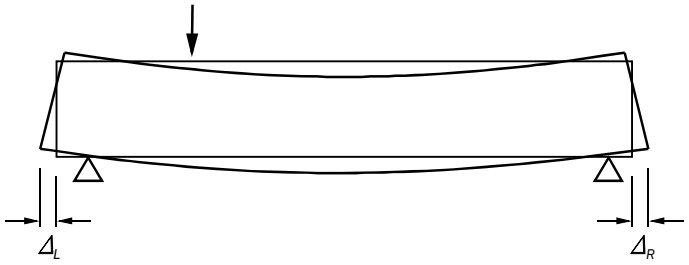

Figure 131 – Definition of transverse support displacements

Figure 132 shows the effect of the transverse reactions on the internal forces. The tension force (T) required to maintain equilibrium is reduced as the reaction (H_L) increases. T will go to zero if the horizontal stiffness of the reaction is sufficiently high.

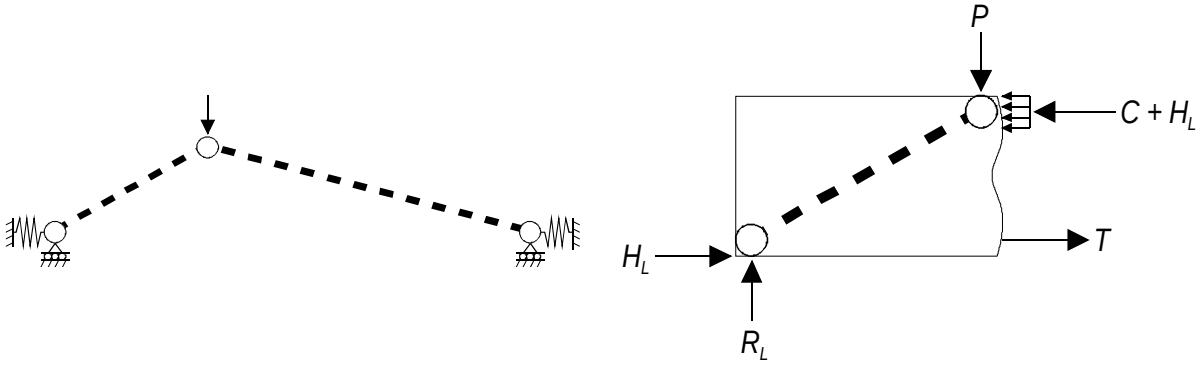

Figure 132 – Effect of support restraint on the girder capacity.

The overall behavior of tests C1U3 and C2U3 are illustrated in Figure 133. As discussed previously, the shear at which cracking occurred was approximately 74 kips for both tests. Furthermore, the behavior up to cracking appears similar between the two girders, indicating that the different support conditions had little effect before the girder cracked. This lack of difference is likely due to the relatively small amount of support movement needed to relieve arching action before cracking occurs.

Figure 134 shows the flexural tensile strain under the load point and the total lateral displacement of the girder bearing (Δ_T) defined as:

$$\Delta_T=\Delta_L+\Delta_R \qquad \text{Eqn. 4}$$

where the variables are defined in Figure 131. The total transverse movement of the bearings on both girders was nearly identical up to cracking. The total movement measured for C1U3 and C2U3 at a superimposed shear of 70 kips was 0.080 and 0.085 inches respectively.

For comparison, one of the transverse support restraints was removed from the model shown in Figure 129 to determine the total transverse movement expected. The resulting total movement was 0.108 in., which is comparable with the experimental values. For the direct concrete bearing condition, it is suspected that support blocks settled as load was applied, which relieved the arching action prior to cracking. Furthermore, the movement was so small that the neoprene bearing pad generated little transverse reaction. In conclusion, the bearing conditions used in these tests appear to have had little effect on the behavior of the girders under service level loads (before cracking). This behavior is expected from girders in the field with similar bearing conditions.

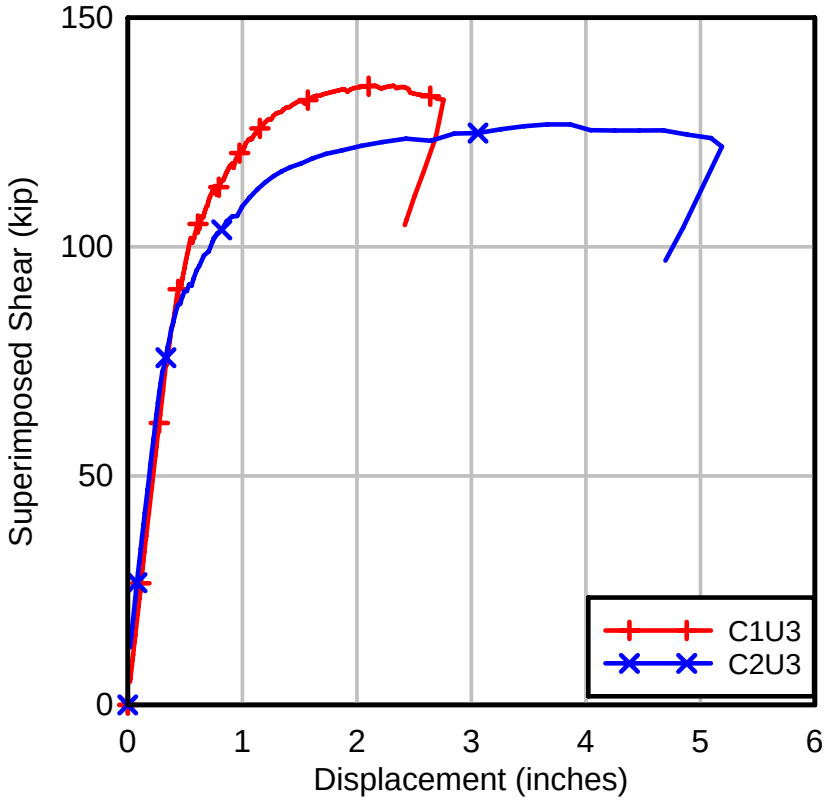

Figure 133 – Load vs. displacement for C1U3 and C2U3.

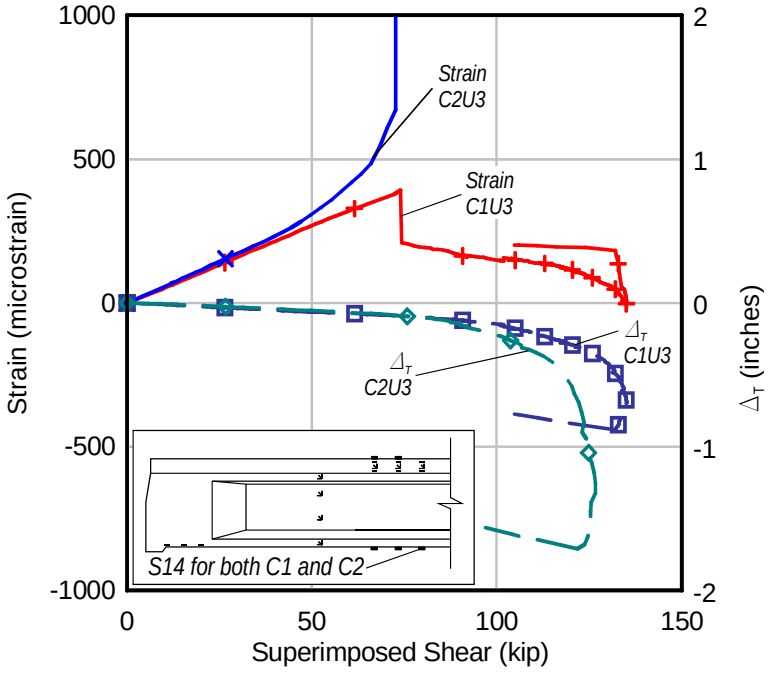

Figure 134 – Plot of C1U3S14, C2U3S14, total bottom displacement for C1U3 and C2U3.

Girder behavior began to diverge at loads beyond cracking (Figure 133). The direct bearing test (C1U3) had a higher post-cracking stiffness and had a 6.8% higher capacity than that of the neoprene bearing test (C2U3). The ultimate displacement, however, was approximately 59.0% of the neoprene bearing test.

Evidence of post-cracking bearing restraint is seen in the divergence of Δ_T as ultimate capacity is approached (Figure 134). After cracking, the total outward support movement of C2U3 was greater than that of C1U3 indicating that the transverse force generated at the support for C1U3 was beginning to affect the behavior. This difference is an indication that the frictional force generated was greater than that provided by the neoprene bearing pads. In conclusion, the direct contact bearing provided more restraint than that of the neoprene bearing pad, thus resulting in higher capacity and less ductility.

6.11 STRUT AND TIE ANALYSIS - C3U2

Figure 122 is the superimposed shear vs. displacement plot for test C3U2. This plot demonstrates that the girder behaved linear-elastically until a shear of 86 kips. Flexural cracks were observed at loads greater than 86 kips. Strain gages S13, S14, and S15 were located on the bottom of the girder and provide information on the initial flexure cracks (Figure 124). A large crack was observed running through the web and into the transition zone between the web and the end block at a shear of 153 kips (Figure 125). After this crack occurred, the girder ceased flexural behavior and commenced strut and tie behavior.

Because the region under examination is a disturbed region, strain profiles at increasing loads were plotted in Figure 135 to evaluate the effect. The plot shows that the overall strain profile is unaffected by the flexural cracking that occurred at lower loads under the load point and by the proximity of the load and reaction points. As the shear increases, the strain profiles appear to be unaffected until a shear of 153 kips is reached where the strain profile is then distorted due to the nearby cracks that formed.

This is also confirmation that the girder had full composite action between the deck and girder, that beam theory applies, and the section behaved as a B-region. B-regions typically begin at a distance of one member-depth away from a discontinuity. This distance is used as a guideline and is not precise. The load point for this test lies at approximately one member – depth away from the transition between the end block and the I-shape in the section.

Figure 136 shows a proposed strut and tie model to describe the behavior of the girder as it reaches ultimate capacity. Strut and tie models are only valid for concrete that has cracked and is on the verge of ultimate capacity. As indicated above, the strain profile became nonlinear with the formation of a significant crack at a shear of 153 kips. Figure 137 shows strain vs. shear data from gages S5 and S6, which were located on the top of the deck. Strain at S5 and S6 grew constantly in compression until a shear of 153 kips, where the strain suddenly dropped. Data from S18, which is aligned with the proposed strut near the support is also shown in Figure 137. The sudden drop in strain at gages S5 and S6, is coincident with a jump in compressive strain at gage S18, which is believed to indicate the change from beam behavior to strut and tie behavior.

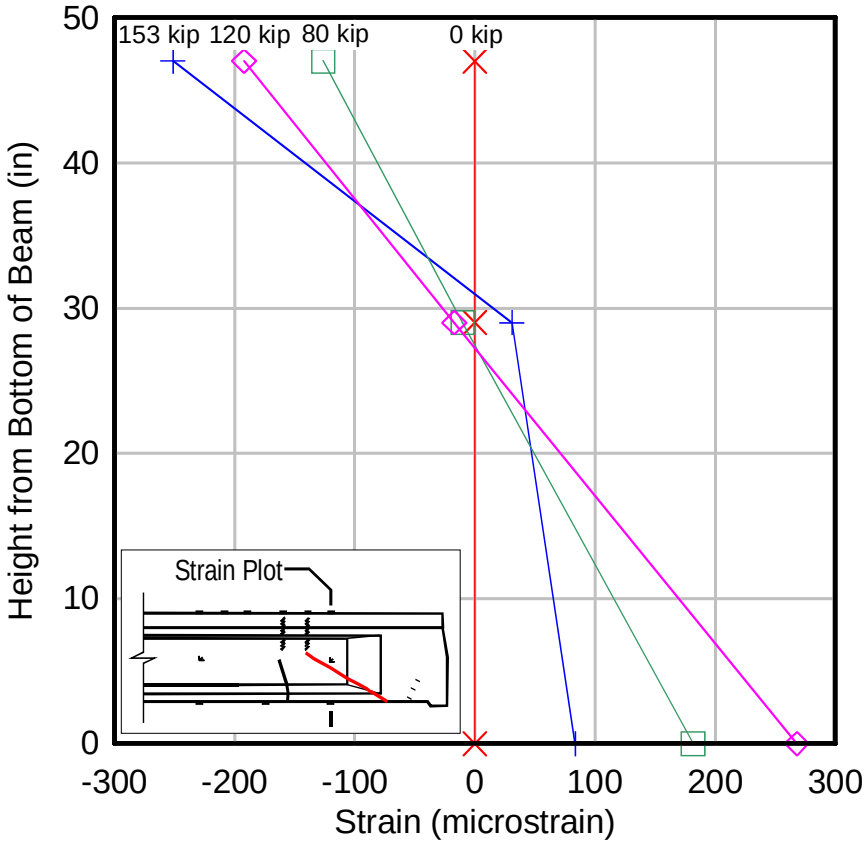

Figure 135 – Change in strain as loading.

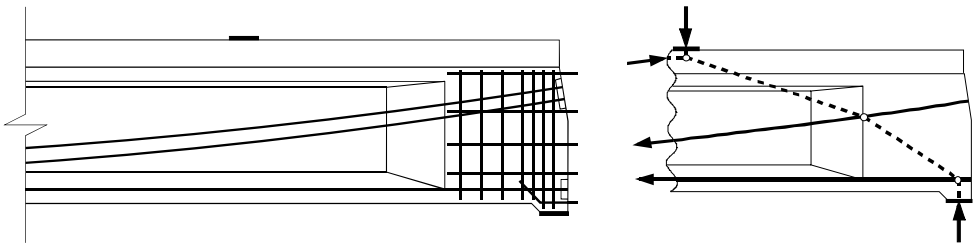

Figure 136 – Strut and tie model.

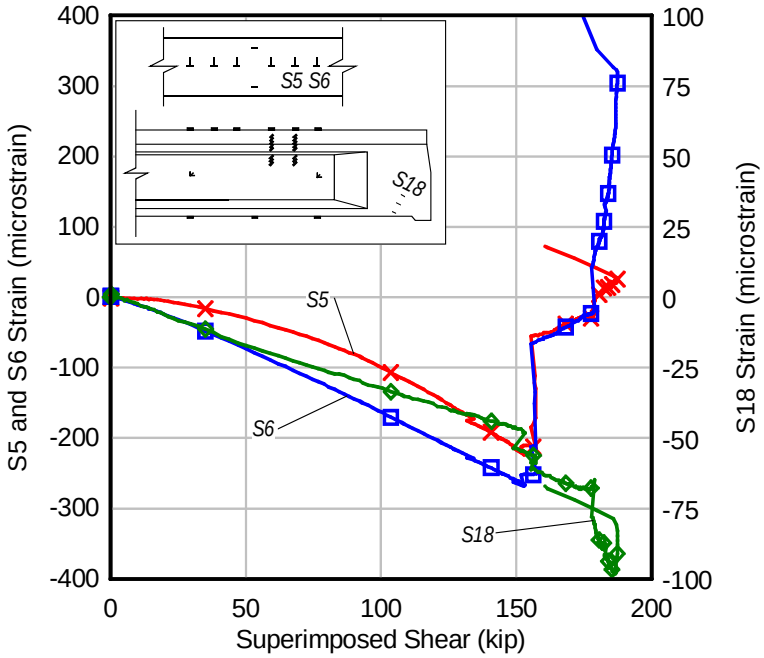

Figure 137 – Strain gage plot for S5, S6, and S18.

6.12 Comparison with Theoretical Capacities

Table 25 shows a comparison of the experimental girder capacity with calculated capacities using the following methods:

1. Modified compression field theory (MCFT) from AASHTO LRFD Bridge Design Specification (2007).
2. Strut and Tie method (STM) from AASHTO LRFD Bridge Design Specification (2007).
3. Detailed method (ACI) from American Concrete Institute ACI 318 (2008)

Nominal moment capacity, M_n, was calculated using the method of strain compatibility (Table 26). Material properties used in the moment, shear and STM calculations were taken

from the concrete cylinder and PT bar test data as follows: 4.0 ksi compressive strength of concrete topping slab, 8.1 ksi compressive strength of the concrete girder, 170 ksi ultimate strength of PT bars, and 29,700 ksi Young's modulus of PT bars. The concrete compressive strengths are representative of the range of tested values. A Ramberg-Osgood equation was fit to the stress-strain curve for use in the strain compatibility calculations. Based on the experimental data, 11% was used for the initial losses. Based on the AASHTO equation, 33% was used for the long term losses.

Data gathered and observations made during testing indicate that the girders had reached (or nearly reached) their flexural capacity. This is corroborated by the large difference between the tested capacity and calculated shear capacities. Consequently, the experimental capacities shown in Table 25 provide a lower bound strength for comparison with the calculated strengths.

The STM procedure was applied only to the a/d=2 test. The STM in Figure 138 shows the internal forces in the girder at capacity. Based on the load displacement curve, it is thought that the PT bars had reached yield before loading was terminated, which simplified determining the force in the bars. Consequently, it was assumed that the PT bars controlled the capacity rather than the nodal regions and struts. This assumption established the force in the PT bars at yield or beyond, and a stress of 170 ksi was used for the STM. Knowing the forces in the bars and the reaction at the support, the forces in the struts were found using a truss analysis. The STM gave the most accurate prediction of capacity, overestimating the capacity by approximately 8%. This is not surprising, however, because the bars controlled the capacity similar to that of the flexural capacity.

Table 25 – Comparison of calculated shear capacity with experimental results.

a/d	V_{EXP} (kip)	**ACI**		**STM**		**MCFT**	
		V_n (kip)	$\frac{V_{EXP}}{V_n}$	V_n (kip)	$\frac{V_{EXP}}{V_n}$	V_n (kip)	$\frac{V_{EXP}}{V_n}$
2	196	92	2.13	213	0.92	111	1.77
3	142	66	2.15	---	---	93	1.53
3 (2nd Test)	133	66	2.02	---	---	93	1.43

Table 26 – Post-Tensioned girder nominal moment capacities (kip-ft).

a/d	$\mathbf{M_{exp}}$	$\mathbf{M_n}$	$\frac{M_{EXP}}{M_n}$
2	1507	1402	1.07
3	1685	1503	1.12
3 (2^{nd} Test)	1587	1503	1.06

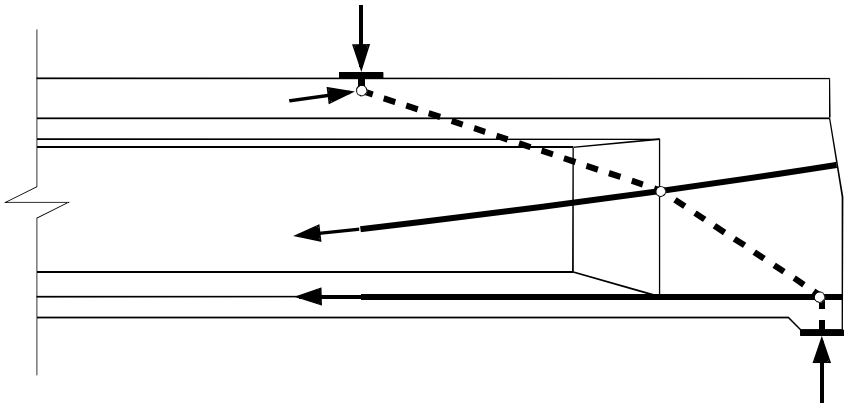

Figure 138 – Forces in strut-and-tie model for superimposed load (self-weight not included).

6.13 SUMMARY AND CONCLUSIONS

Three girders were constructed and post-tensioned using plans for an existing bridge. The test girders closely matched a girder design that was used in Florida in the 1950s. The girders had no shear reinforcement outside of the end block, approximately 3 ft from each end of the girder. Each girder had two straight PT bars and two parabolic PT bars. The bars were anchored using 1.75-in. thick steel plates. Post-tensioning stresses were monitored and recorded. Losses were calculated using strains measured during stressing. Seating and elastic losses were determined from measured strain data. In addition, creep and shrinkage losses were monitored for approximately 2.5 days. Losses due to creep and shrinkage were higher than values calculated using LRFD.

The effect of support conditions on girder behavior was also evaluated. The support conditions were of interest because existing girders in the field have been observed to bear directly on concrete. A test was conducted with a shorter a/d ratio to determine the behavior of the girder subjected to loads near the support. Shear behavior was of interest because the girders

lacked shear reinforcement outside of the end blocks. The lack of shear reinforcement has led to low ratings for bridges built with this type of girder. Following are the salient findings from the research:

1. Girders bearing directly on concrete behaved the same as girders bearing on neoprene pads up until cracking occurred. The girder bearing directly on concrete displayed a 7% larger capacity than the girder bearing on a neoprene pad. The girder bearing on concrete, however, displayed nearly half the displacement capacity than that of the girder on neoprene.
2. Variation of the bearing condition did not change the failure mode, which was a flexural failure.
3. The girder tested at an a/d ratio of two did not fail in shear, even with the absence of shear reinforcement.
4. A strut & tie model best represented the behavior of the girder tested with an a/d ratio of two.
5. The moment capacity of each girder was accurately predicted using the principles of strain compatibility. The calculated moment capacities were between 6% and 12% lower than the experimentally determined capacities.

7 OVERVIEW OF MAJOR FINDINGS

The testing reported in the research report focused primarily on the capacity and failure modes of prestressed concrete girders tested in three-point bending with the load point offset so as to cause high shear to moment ratios. The objective was to determine the "shear" capacity of the girders and to determine the behavior mode relative to the models currently available in the AASHTO LRFD design specifications to predict shear capacity. All of these girder designs (or very similar designs) are in use in Florida Bridges.

Three different sets of bridge girders were tested. Each had their own unique configuration. The Type IV girders had a debonding pattern that did not meet LRFD requirements. The Type III girders used a combination of harped and straight strands with a precast panel deck system. The PT girders used a bar post-tensioning system that was designed and installed nearly 40 years ago, and is not currently used in new construction. This design had no shear reinforcement away from the end block.

The Type IV girders failed due to separation of the bottom bulb flange, which is described in more detail below and in the report. This premature failure restricted the capacity of the girder, not allowing it to reach the full shear capacity as predicted by the three code models in the table. The Type III girders failed from strand slip for a/d up to approximately 3. The strand slip and ultimate capacity were favorably influenced by vertical and horizontal end block reinforcement as discussed below. Finally, the PT girders had capacities well beyond those predicted. Note that the girders were not taken to their full capacity due to lab safety concerns. Nevertheless, the results indicate that the girder had reserve capacity well beyond that predicted by the code equations for shear, even though there were no stirrups provided in the web.

7.1 TYPE IV GIRDERS

The type IV girders failed in an unusual manner not associated with typical shear or flexure failure modes. Furthermore, the capacity of the girder was lower than predicted by code shear models. The early failure of the girder was attributed to two characteristics of the girder design. One was the irregular debonding pattern that placed fully bonded strands in the flanges of the bottom bulb and debonded strands under the web. The other was the lack of confinement steel in the bottom bulb near the support. Figure 139a illustrates the flow of forces as capacity is imminent in a girder with all strands fully bonded. The strut and tie model shows a diagonal

strut and a longitudinal tie that are typical of a girder with a short shear span. The strut passes through the web and terminates under the load point at one end and at a node just over the support at the other end. The tendon forms the tie, which must be anchored into the node over the support point to ensure equilibrium. The typical mode of behavior for this configuration is for the strand to slip. This typically occurs when the load point is very near the support, which results in a short strand development length.

In these test girders, only the strands in the outside portion of the flange were bonded near the support, and thus able to act as ties as shown in Figure 139b. This resulted in a disruption of the node at the support point. Because of the offset between the strut in the web and the two ties in each flange of the bulb (fully bonded strands), secondary struts formed to transfer the load laterally to the nodes at the ties. Additional secondary struts were essential between the support and the nodes at the ties to complete the load path to the support. Both pairs of secondary struts induced horizontal components that acted transverse to the beam. A tension tie is shown between the flange nodes in the illustration. The test beam, however, lacked transverse reinforcement that might have held the bulb together after cracking.

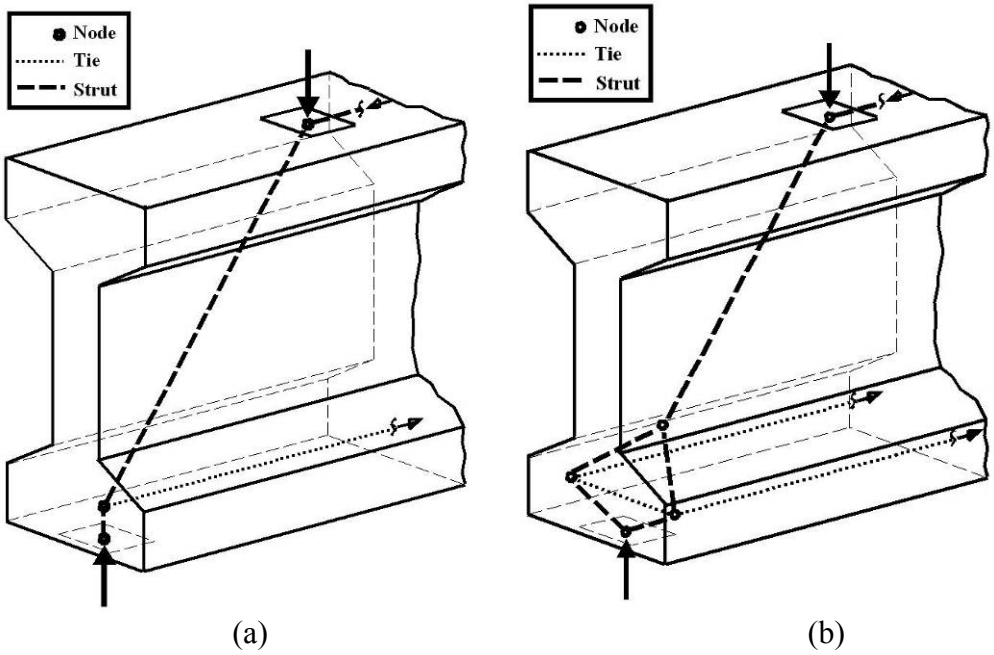

(a) (b)

Figure 139 – Strut and tie model for tendon with (a) fully bonded strands and (b) an excessive number of strands debonded under the web.

Figure 140 shows the cracking pattern exhibited by girder A2U1 after reaching capacity. The girder capacity was controlled by the formation of a large crack at the outer pair of strands in the bulb flange. It is believed that this crack formed as a result of the transverse tensile stresses in the concrete resulting from strut divergence shown in Figure 139b. The crack formed at the edge of the bearing pad. As the crack progressed along the beam it angled toward the web and terminated at the web at a distance of approximately half the girder depth. This crack caused a loss of the tie from the outside node, thus resulting in the strand peeling away from the bulb as indicated by the arrow. This behavior may have caused problems with strand slip measurements, since the frame supporting the displacement devices was attached to the bulbs.

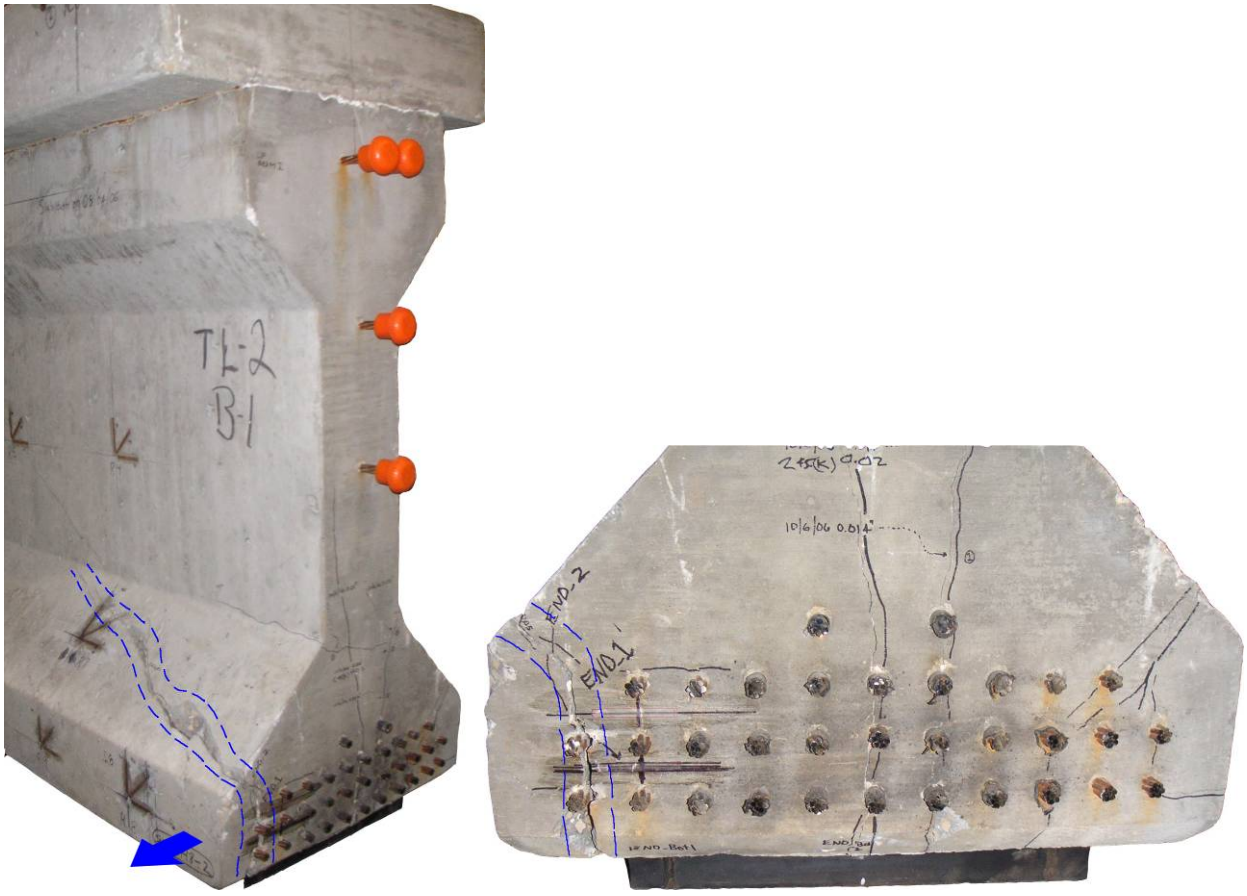

Figure 140 – Bulb cracking pattern caused by excessive debonding under the web.

7.2 TYPE III GIRDERS

As indicated in the summary table, many of the Type III girders with small a/d ratios failed due to strand slip. Generally, a flexure-shear crack formed near the support that

interrupted the strand development length. Figure 141 shows a plot of shear vs. displacement and shear vs. strand slip for three selected strands. The first crack formed at 182 kips where a slight slip in the strands can be seen. Reserve load capacity, however, was provided by the supplemental vertical and horizontal mild steel reinforcement included in the end region of the girder. If the girder was constructed without this end reinforcement, it is likely that a mechanism would have formed and the girder would have been unable to carry additional load. The capacity would have been dependent solely on the slip resistance of the strand between the crack and the girder end.

The photograph in Figure 142 shows the girder with the primary crack and the associated free body diagram with the forces generated when the flexure-shear crack formed. As shown in the free body diagram, the mild steel reinforcement in the end of the beam is activated when the crack forms and the strands slip. As the load was increased, however, the steel eventually either yielded or failed in bond or both. Figure 141 and Figure 142 both exhibit a range between 182 kips and 230 kips where the strand continues to slip and there is a slight loss in stiffness. After 230 kips, though, the strand slip increases markedly and the stiffness begins to decrease rapidly. This is thought to be where the mild steel reinforcement yielded. Due to the gradual reduction in stiffness exhibited in the load-displacement plot, it is believed that some of the bars reached yield. If some or all of the bars had experienced a bond failure, the load displacement would have indicated a sudden decrease in load.

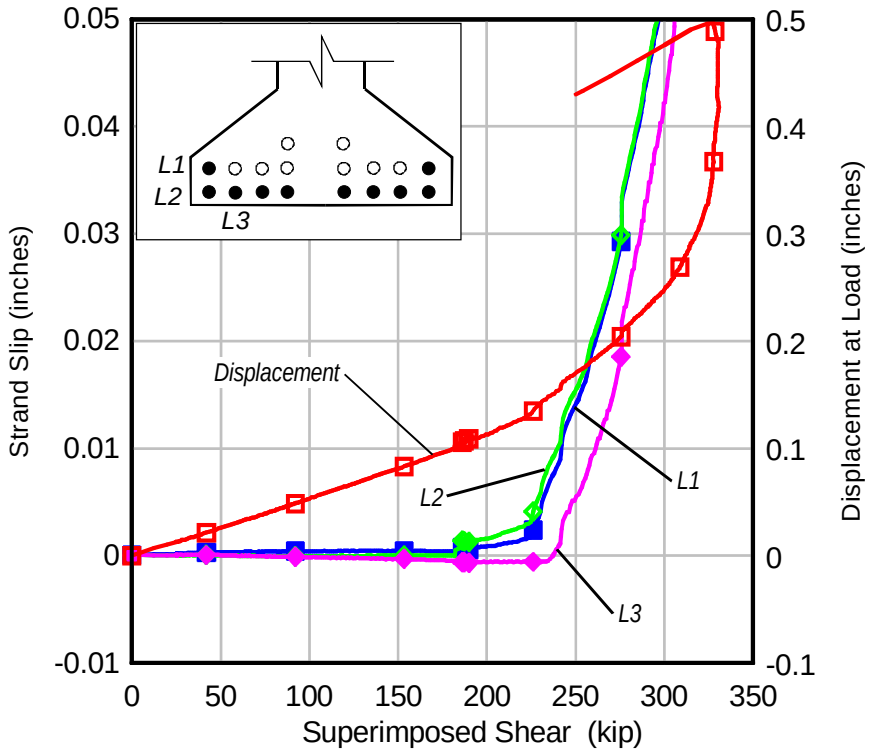

Figure 141 – B1U1 strand slip and displacement.

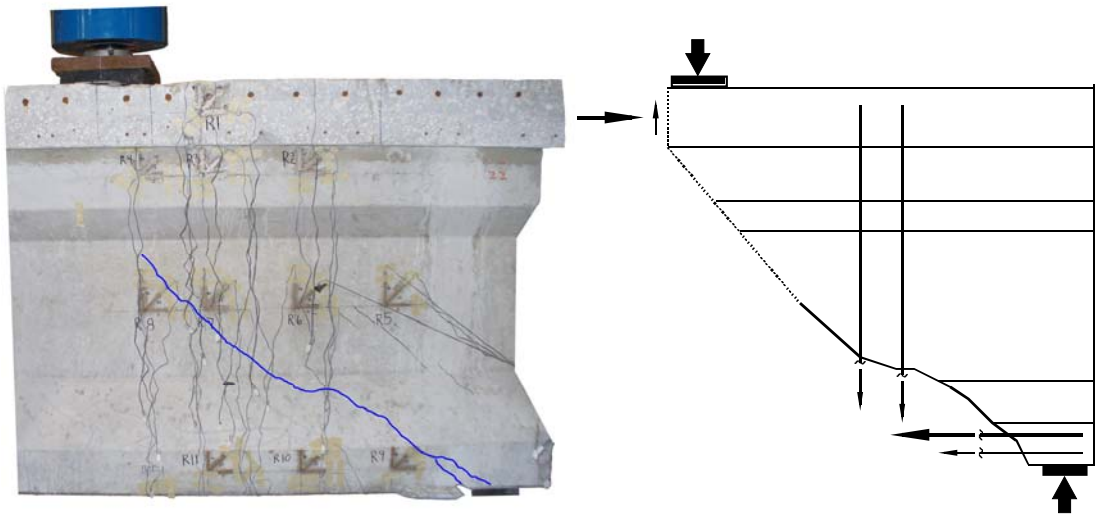

(a) (b)

Figure 142 – Girder B1U1 (a) photo with the primary crack enhanced and (b) free body diagram including contribution of vertical and horizontal reinforcement

7.3 PT GIRDERS

In addition to capacity, the effect of longitudinal support restraint was investigated in the PT girders (Figure 143).

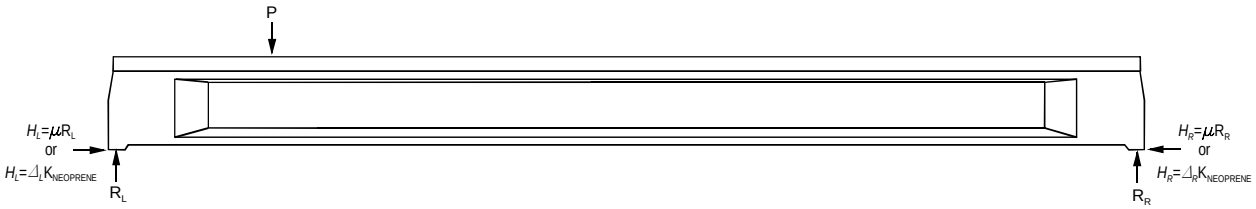

Figure 143 – Horizontal reactions generated by the varying support conditions.

The overall behavior of tests C1U3 and C2U3 are illustrated in Figure 133. Test C1U3 was placed directly on concrete supports while C2U3 was placed on neoprene. The shear at which cracking first occurred was approximately 74 kips for both tests. Furthermore, the behavior up to cracking appears similar between the two girders, indicating that the different support conditions had little effect before the girder cracked. This lack of difference is likely due to the relatively small amount of support movement needed to relieve arching action before cracking occurs. Post-cracking behavior diverges for the two girders. The girder supported on concrete continues to a peak capacity slightly larger (about 6.5%) than that of the girder on neoprene. The girder on neoprene, however, appears to have nearly twice the displacement capacity of the girder bearing directly on concrete.

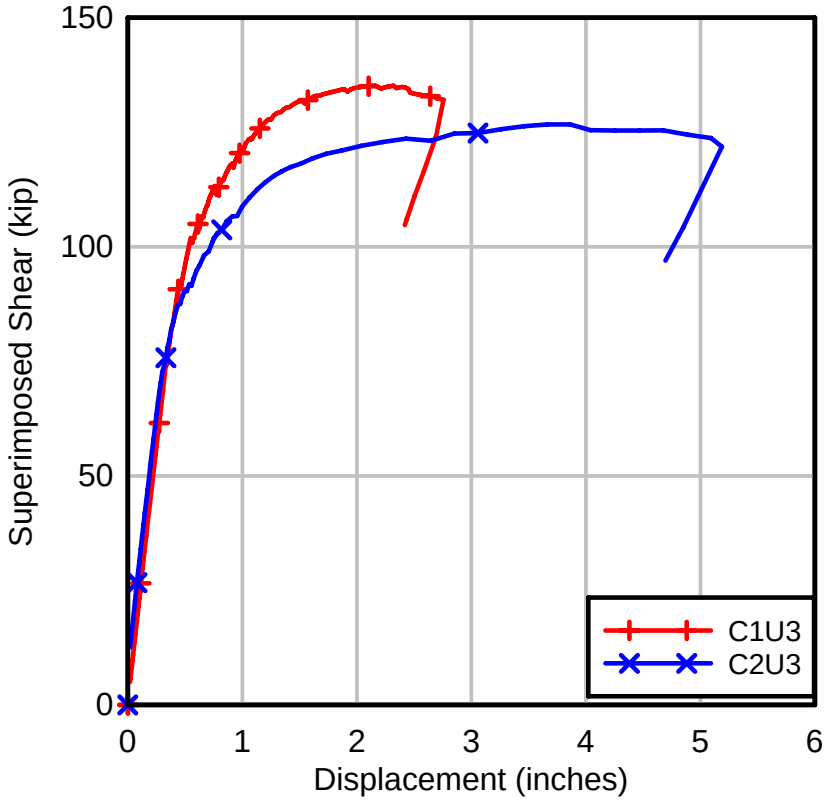

Figure 144 – Load vs. displacement for C1U3 and C2U3.

8 REFERENCES

AASHTO LRFD Bridge Design Specifications, American Association of State Highway Transportation Officials, Washington, DC, 2007.

AASHTO Standard Specifications for Highway Bridges, American Association of State Highway Transportation Officials, Washington, DC, 2002.

ACI 318, Building Code Requirements for Structural Concrete and Commentary, American Concrete Institute, Farmington Hills, MI, 2008.

Alshegeir, A. and Ramirez, J. (1992). "Strut-Tie Approach in Pretensioned Deep Beams." *ACI Structural Journal*. 89(3), May-Jun, 296-304.

Avendano, A. R. and Bayrak, O. B. (2008). "Shear Strength and Behavior of Prestressed Concrete Beams," University of Texas at Austin, report IAC-88-5DD1A003-3, Sep 2008, 170 pp.

Bakht, B. and Jaeger, L. (1988). "Bearing Restraint in Slab-on-Girder Bridges." *Journal of Structural Engineering*. 114(12), Dec, 2724-2740.

Brown, M. D., Bayrak, O., and Jirsa, J. O., (2006). "Design for Shear Based on Loading Conditions," *ACI Structural Journal*, 103(4), Jul-Aug 2006.

Collins, M. and Mitchell, D. (1991). *Prestressed Concrete Structures*. Prentice-Hall, Englewood Cliffs, NJ., 766 pp.

Lybas J., Fagundo F, Cook R., and Hoffman V. (1998). "Effects of Internal and External Constraints on the Shear and Bond Strength of Precast Prestressed Concrete Girders." University of Florida. Report for the Florida DOT Research Management Center, Tallahassee, FL

Giaccio, C., Al-Mahaidi, R., and Taplin, G. (2002). "Experimental study on the effect of flange geometry on the shear strength of reinforced, concrete T-beams subjected to concentrated loads." *Canadian Journal of Civil Engineering*. 29(6), Dec, 911-918.

Hawkins, N. M., Kuchma, D. A., Mast, R. F., Marsh, M. L., and Reineck, K. H. (2005). "Simplified Shear Design of Structural Concrete Members," National Cooperative Highway Research Program Report 549, July 2005.

Khalifa, A. and Nanni, A. (2000). "Improving shear capacity of existing RC T-section beams using CFRP composites." *Cement & Concrete Composites*. 22(3), Jun, 165-174.

MacGregor, J. and Wright, J. (2005). *Reinforced Concrete Mechanics and Design Fourth Edition*. Pearson Prentice-Hall, Upper Saddle River, NJ. 1132 pp.

Polak, M. and Dubas,, J. (1996). "Shear design of high strength concrete beams – Canadian code perspective." *Canadian Journal of Civil Engineering*. 23(4) Aug, 809-819.

Ramirez, J. (1994). "Strut-Tie Design of Pretensioned Concrete Members." *ACI Structural Journal*. 91(4), Sep-Oct, 572-578.

Razaqpur, A. and Isgor, O. (2006). "Proposed Shear Design Method for FRP-Reinforced Concrete Members without Stirrups." *ACI Structural Journal.* 103(1) Jan-Feb, 93-102.

Ramirez, J. A. and Russell, B. W. (2007). "Transfer Development, and Splice Length for Strand/Reinforcement in High-Strength Concrete," National Cooperative Highway Research Program Report 12-60, July 2007.

Saenez, N. and Pantelides, C. (2005). "Shear Friction Capacity of Concrete with External Carbon FRP Strips." *Journal of Structural Engineering*. 131(12) Dec, 1911-1919.

Schlaich, J., Schafer, K., Jennewien, M. (1987). "Toward a Consistent Design of Structural Concrete." *Journal Prestressed Concrete Institute*. 32(3), May-Jun, 74-150.

Shahawy, M. and Cai, C.(1999). "A new approach to shear design of prestressed concrete members." *PCI Journal*. 44(4) Jul-Aug, 92-117.

Wolf, T and Frosch, R (2007). "Shear Design of Prestressed Concrete: A Unified Approach." *Journal of Structural Engineering*. 133(11) Nov, 1512-1519.

APPENDIX A – TEST DATA - AASHTO TYPE IV GIRDERS

Table 27 – Concrete mixture design.

Constituents	Test girder - 1		Test girder – 2	
	Truck-1 (lbs)	Truck-2 (lbs)	Truck-3 (lbs)	Truck-4 (lbs)
Cement	3870	3865	3865	3865
Fly ash	990	985	1025	980
Coarse aggregate	11500	11500	11360	11480
Fine aggregate	7340	7260	7300	7340
Water	964	1060	1088	1082
Admixtures	(fl. oz)	(fl. oz)	(fl. oz)	(fl. oz)
Air entraining agent	13	13	13	13
Superplasticizer	130	130	130	130
Water reducer	115	115	115	115

Table 28 – Concrete plastic properties.

	Test girder-1		**Test girder -2**	
Plastic properties	**Truck-1**	**Truck-3**	**Truck-3**	**Truck-4**
Unit weight	139.63 pcf	139.63 pcf	139.63 pcf	139.63 pcf
Air content	3.7%	3.4%	3.6%	3.0%
Temperature	91°F	91°F	91°F	90°F
Slump	6.5-in.	6.5-in.	5.5-in.	6.75-in.
Water/cement ratio	0.32	0.34	0.34	0.34

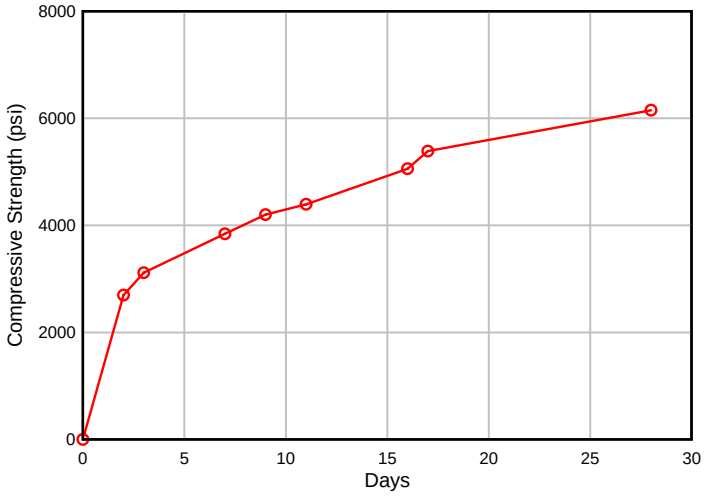

Figure 145 – Concrete Compressive Strength Gain Curve

Table 29 – Modulus of rupture results 3 days before flexure tests.

MOR	f_r (psi)	$f_r/\sqrt{f'_c}$
MOR-2	799	9.61
MOR-4	650	7.82
MOR-5	677	8.14

Table 30 – Steel strength and modulus.

Sample Number	1	2	3	4	AVG	ASTM A416
Strength (ksi)	277	275	287	282	280	>250
Elongation (%)	5.99	5.68	7.08	5.88	6.14	>3.5%
Yield point at 1% elongation	57630	57320	54270	57110	56582	>
Modulus of Elasticity (ksi)	29,200	29,200	30,000	29,900	29,575	n/a

Type IV AASHTO Girders – 15 ft Shear Test with FRP

Load Deflection Plot

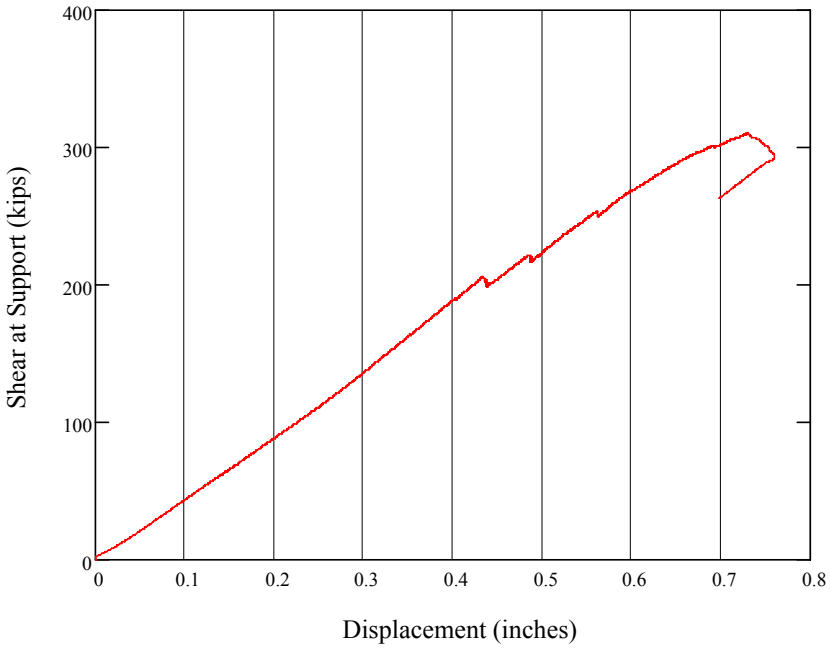

This plot shows the deflection at the point of loading. As the girder was loaded the plot indicates linear-elastic behavior up to a load of 264 kips where the girder first cracked. The cracks were visibly noted to occur in the locations shown in the figure below. A loss in load was noted immediately after first crack indicating a loss in stiffness. Based on the slope of the initial linear elastic behavior and comparing it to the new slope you see there is a slight reduction in new stiffness. Another crack opens up at 281 kips followed by a slight reduction in load possibly indicating a further loss in stiffness. The slope of the load displacement curve following this second crack, however, does not seem to indicate a significant change.

Diagram of Crack Pattern (Shear at the Support = 205 kips)

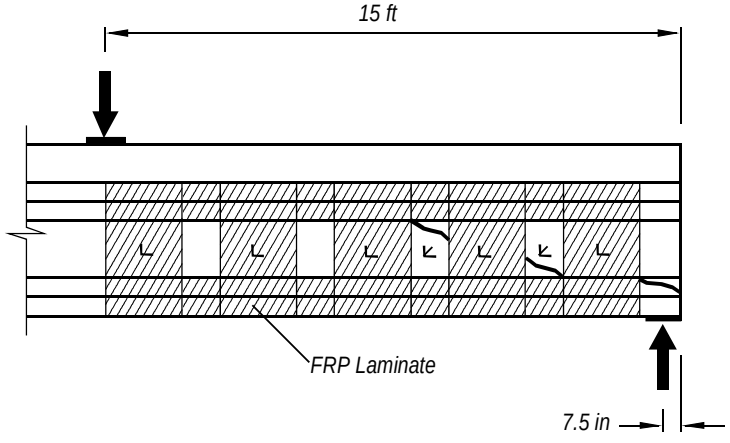

Diagram of Final Crack Pattern (Shear at the Support = 310 kips)

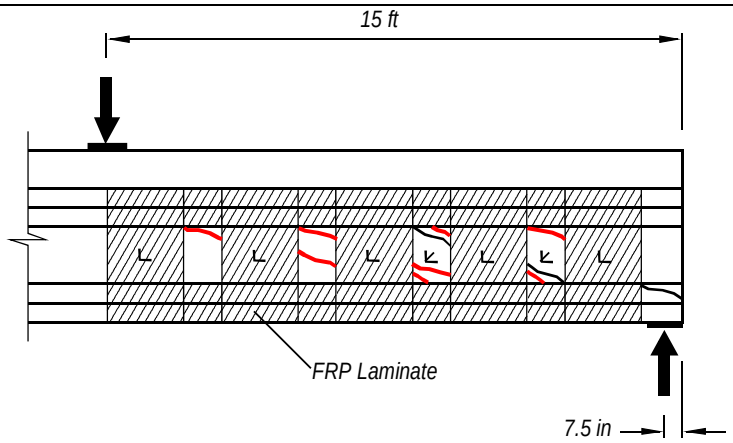

These diagrams illustrate the pattern of cracking. The black lines show the initial cracking and the red lines show where more cracks developed.

Type IV AASHTO Girders – 15 ft Shear Test (Control)

Load Deflection Plot

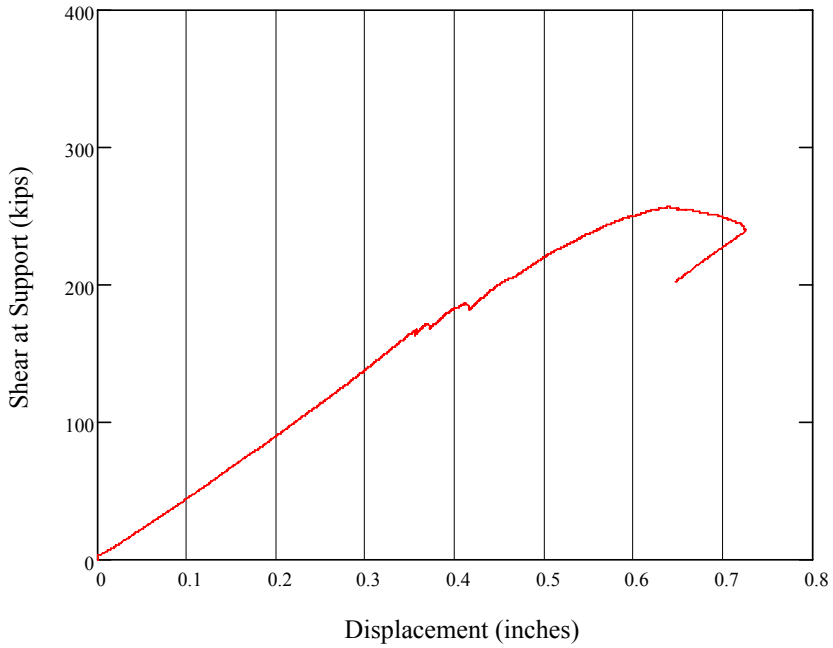

Diagram of Crack Pattern (Shear at the Support = 170 kips)

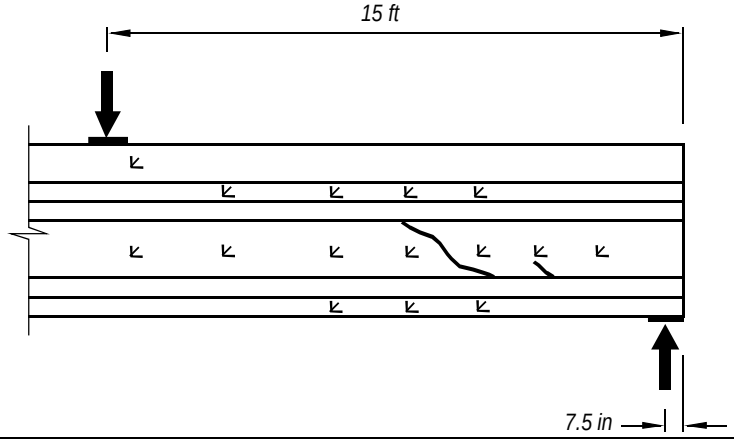

Diagram of Final Crack Pattern (Shear at the Support = 256 kips)

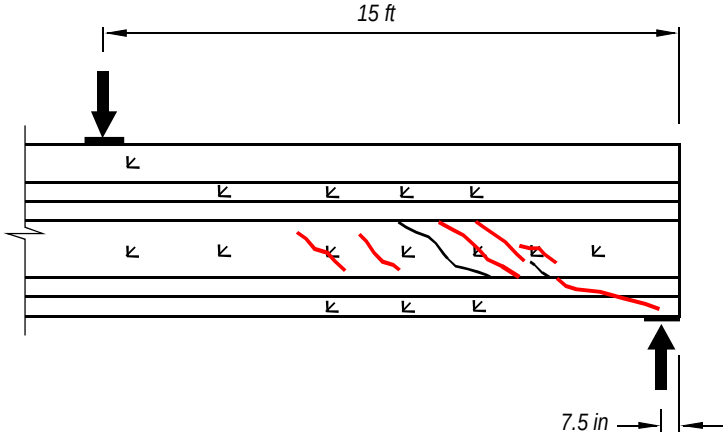

These diagrams illustrate the pattern of cracking. The black lines show the initial cracking and the red lines show where more cracks developed.

Type IV AASHTO Girders – 7 ft 2 in Shear Test on FRP

Load Deflection Plot

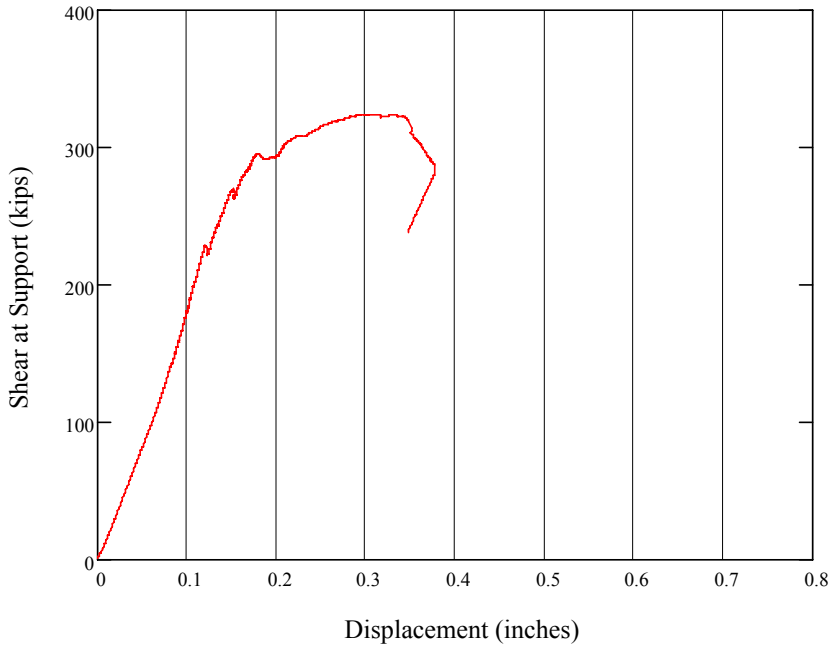

Diagram of Crack Pattern (Shear at the Support = 228 kips)

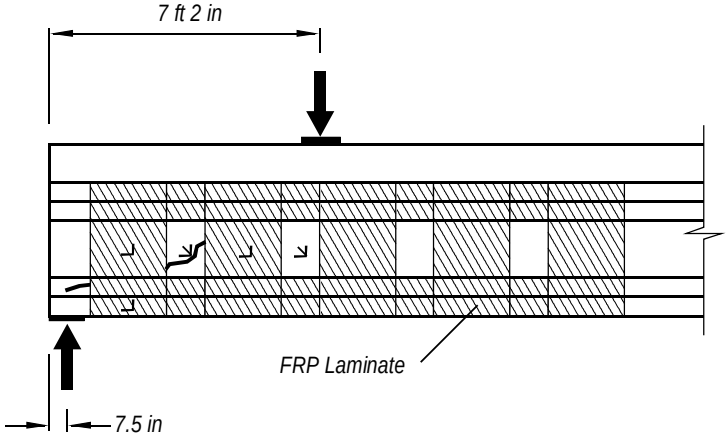

Diagram of Final Crack Pattern

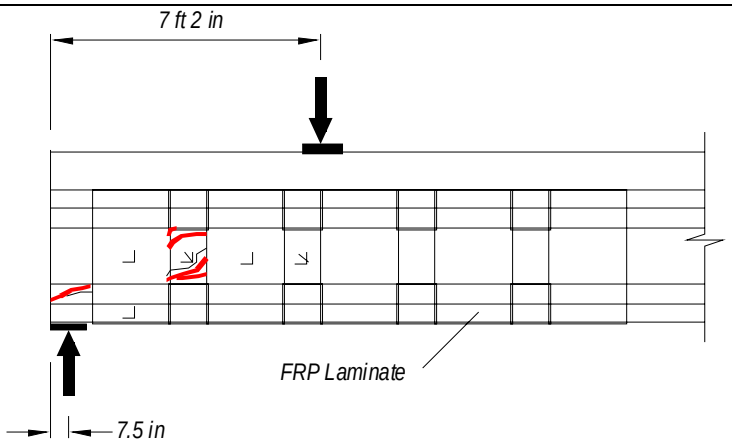

These diagrams illustrate the pattern of cracking. The black lines show the initial cracking and the red lines show where more cracks developed. The gage rosettes are also shown.

Type IV AASHTO Girders – 7 ft 2 in Shear Test (Control)

Load Deflection Plot

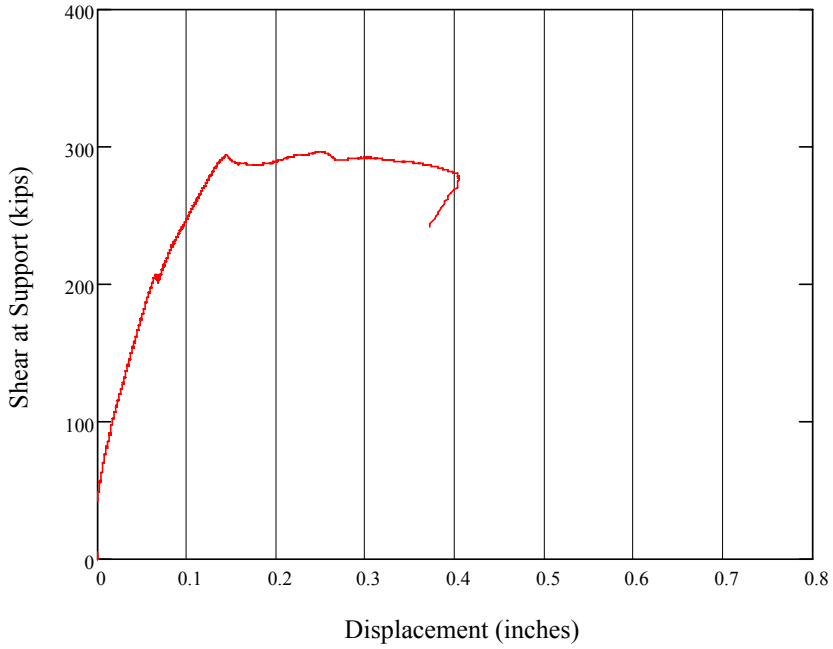

Diagram of Crack Pattern (Shear at the Support = 205 kips)

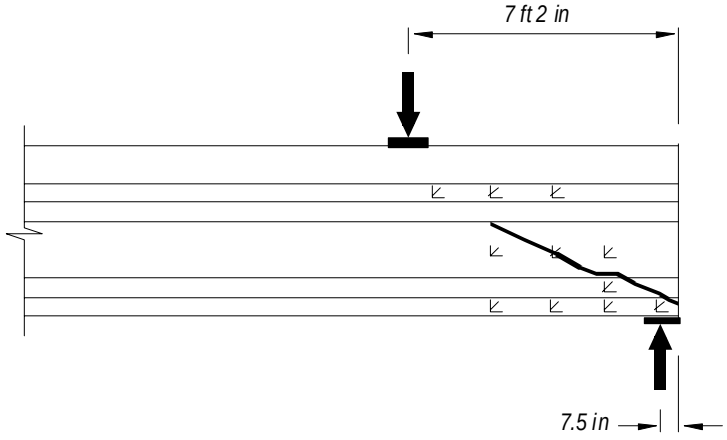

Diagram of Final Crack Pattern

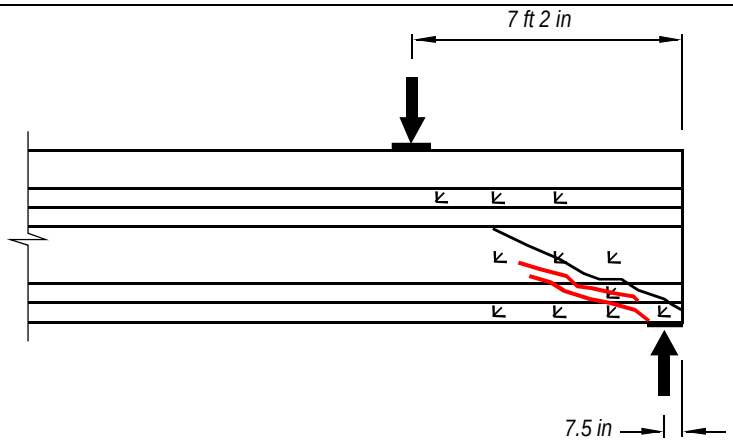

These diagrams illustrate the pattern of cracking. The black lines show the initial cracking and the red lines show where more cracks developed. The gage rosettes are also shown.

Strain Rosette	First Crack Strain (Max, Microstrain)	First Crack Angle (Degrees)
RFS42_28	250	-89
RFS78_28	130	72
RCS42_50	30	-45
RCS60_50	40	-55
RCS78_50	40	-78
RCS24_28	120	79
RCS42_28	125	89
RCS60_28	120	75
RCS24_12.5	150	75
RCS7.5_4	35	88
RCS24_4	30	10
RCS42_4	105	10
RCS60_4	150	8
RFL42_28	135	88
RFL78_28	155	88
RFL168_60	88	-10
RCL60_50	30	-45
RCL78_50	60	-47
RCL96_50	30	16
RCL132_50	30	8
RCL24_28	110	85
RCL42_28	160	90
RCL60_28	300	-80
RCL78_28	100	85
RCL96_28	140	-90
RCL132_28	130	90
RCL168_28	190	82
RCL60_4	115	12
RCL78_4	150	10
RCL96_4	190	3
RCL168_60	60	-3

APPENDIX B – TEST DATA – AASHTO TYPE III GIRDERS

Type III AASHTO Girders – a/d=1 in Shear Test

Load Deflection Plot

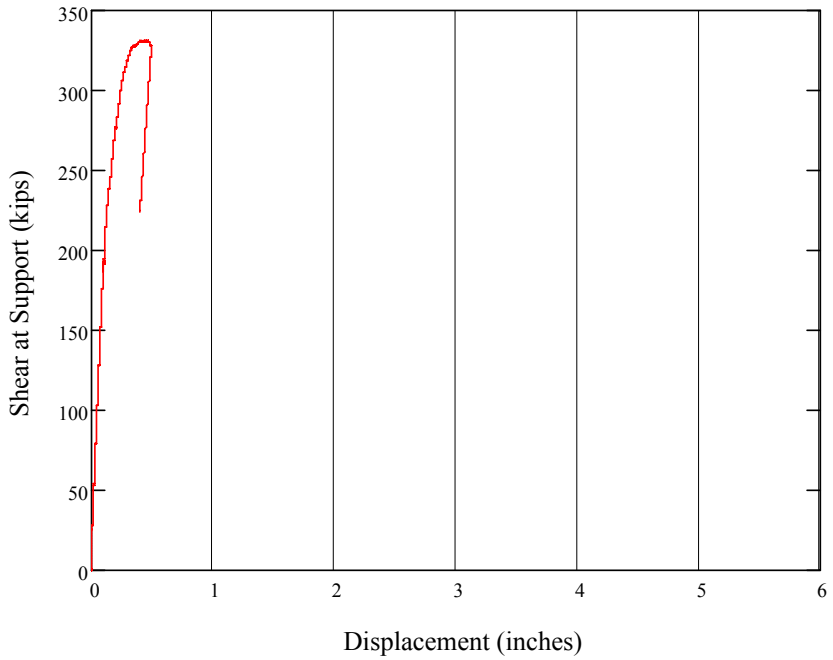

Diagram of Crack Pattern (Shear at the Support = 182 kips)

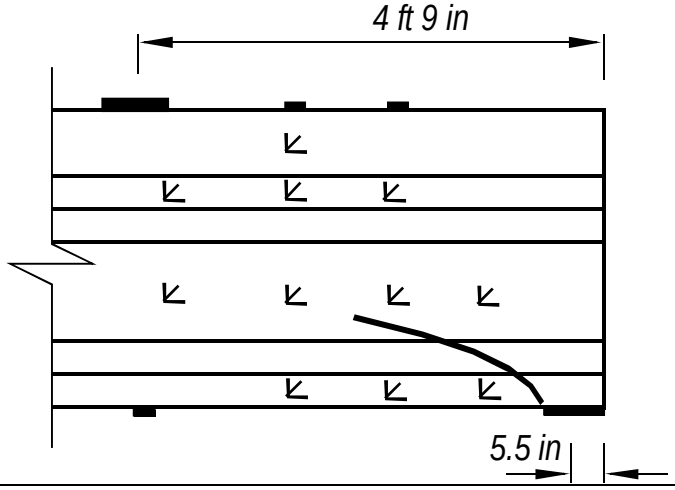

Diagram of Final Crack Pattern

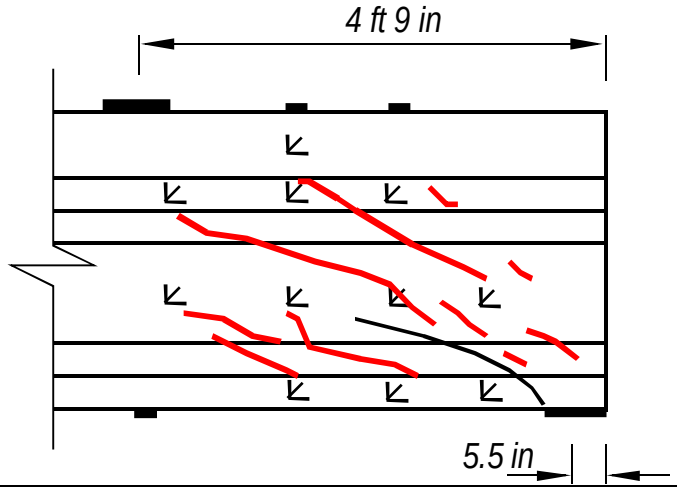

These diagrams illustrate the pattern of cracking. The black lines show the initial cracking and the red lines show where more cracks developed. The gage rosettes are also shown.

Type III AASHTO Girders – a/d=2 in Shear Test

Load Deflection Plot

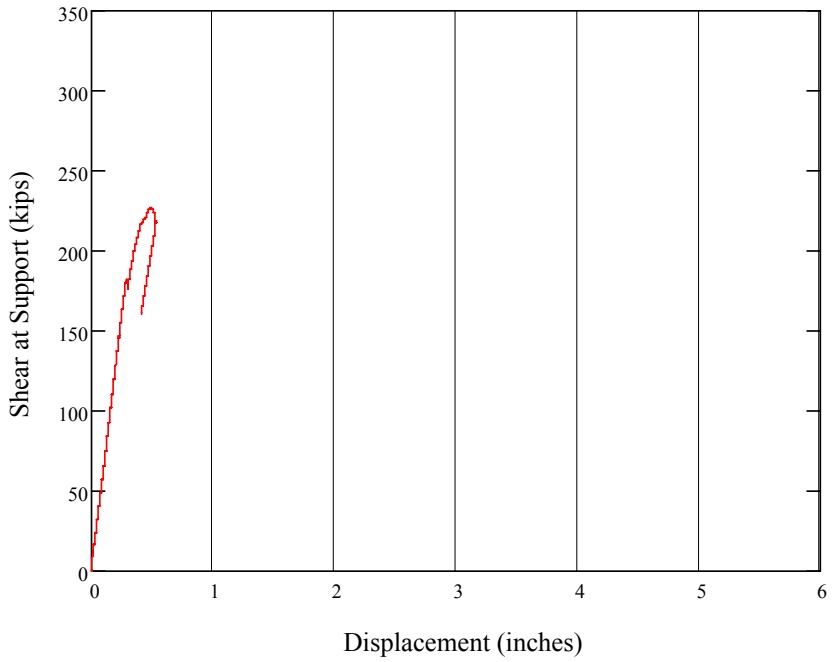

Diagram of Crack Pattern (Shear at the Support =181 kips)

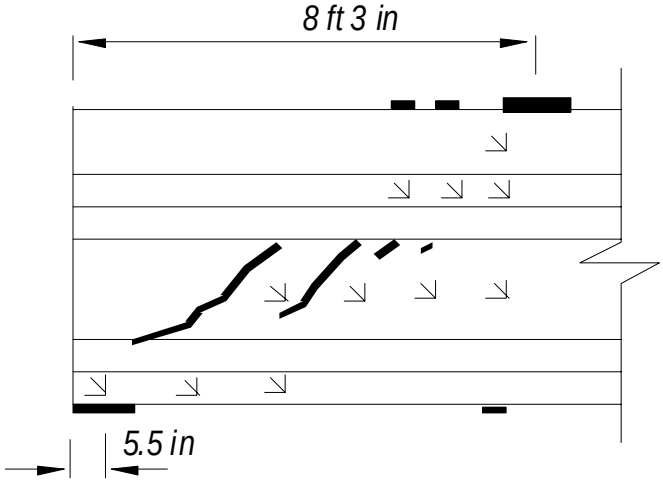

Diagram of Final Crack Pattern

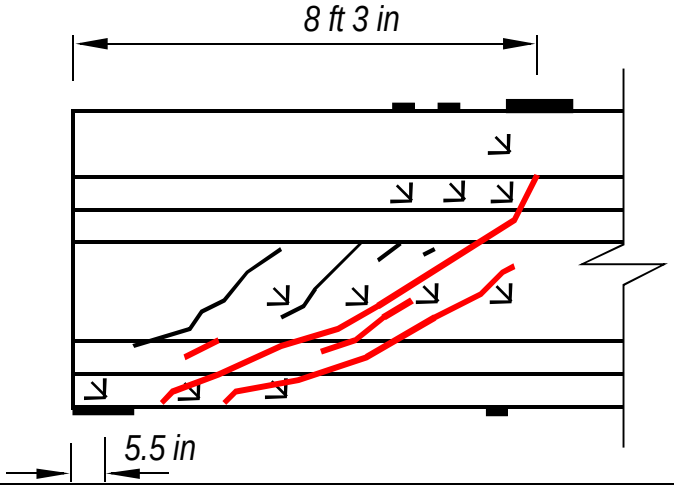

Type III AASHTO Girders – a/d=2 in Shear Test (Second Test)

Load Deflection Plot

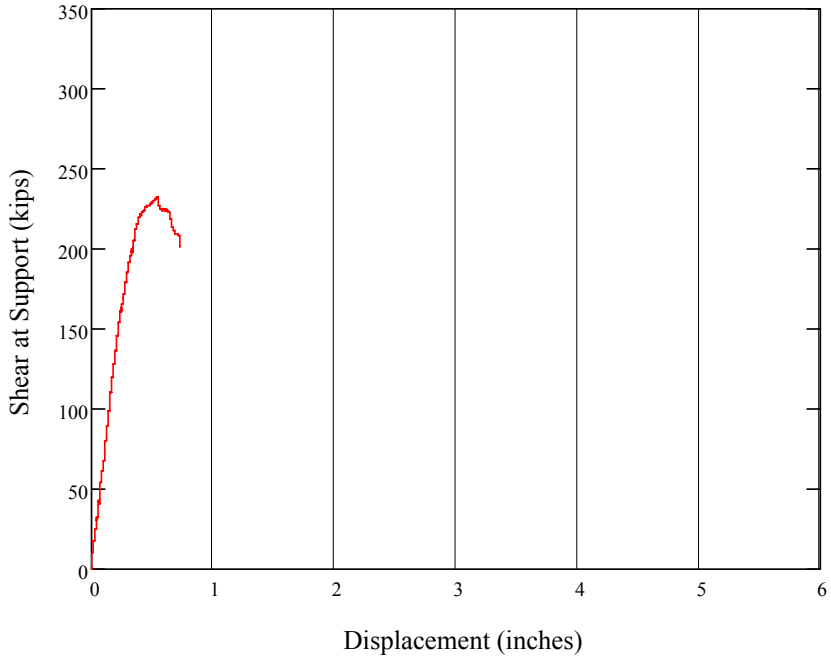

Diagram of Crack Pattern (Shear at the Support =162 kips)

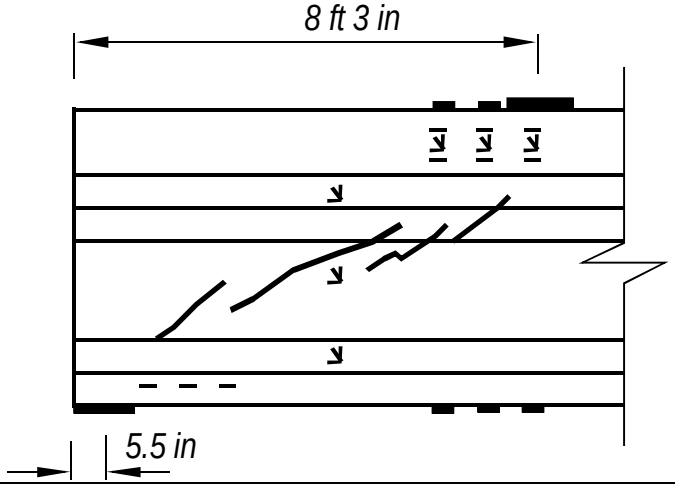

Diagram of Final Crack Pattern

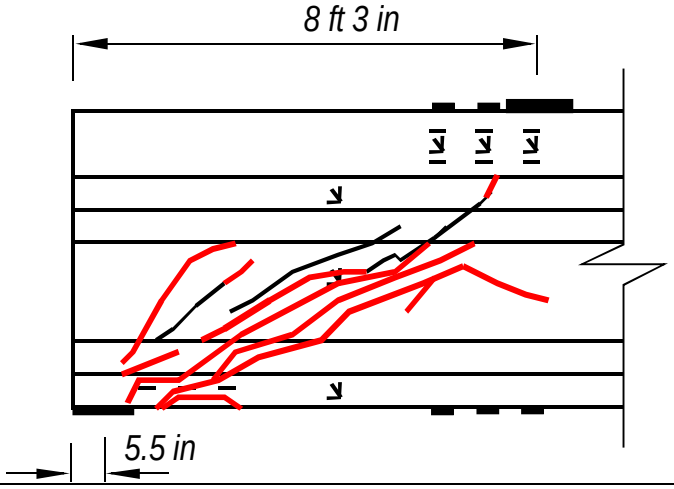

Type III AASHTO Girders – a/d=3 in Shear Test

Load Deflection Plot

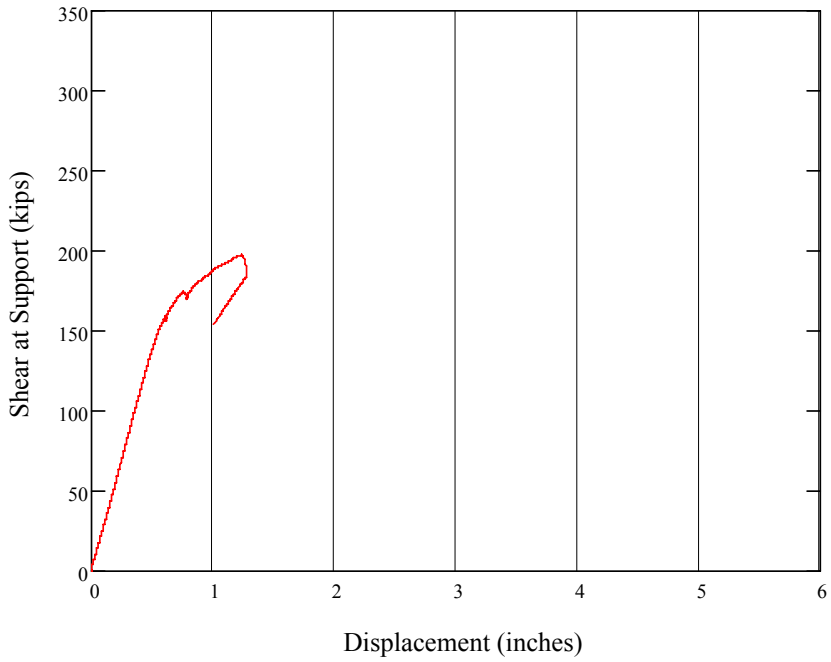

Diagram of Crack Pattern (Shear at the Support = 138 kips)

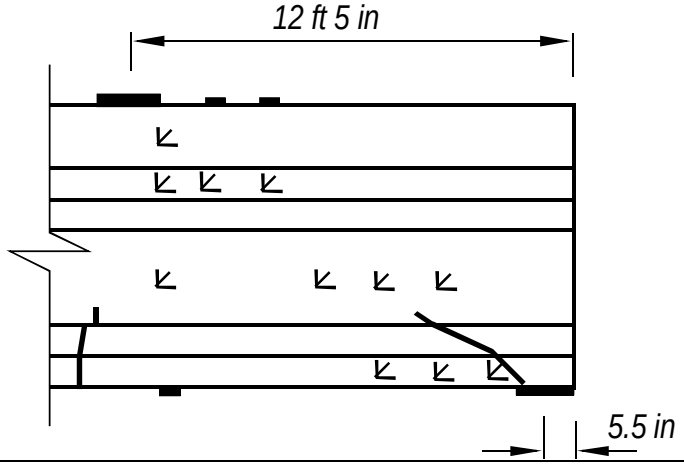

Diagram of Final Crack Pattern

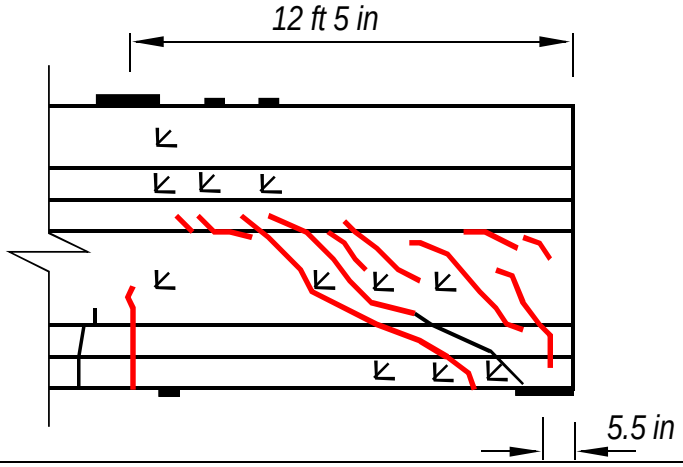

Type III AASHTO Girders – a/d=4 in Shear Test

Load Deflection Plot

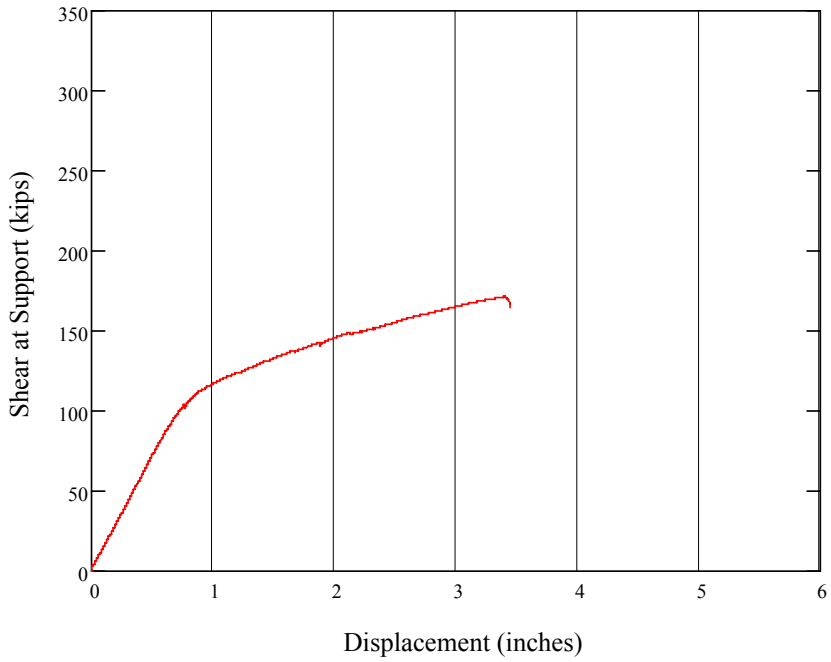

Diagram of Crack Pattern (Shear at the Support = 105 kips)

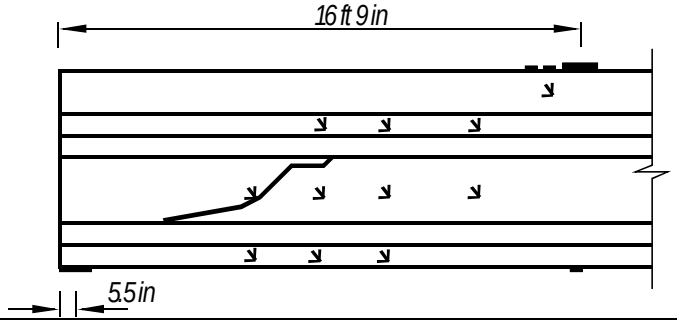

Diagram of Final Crack Pattern

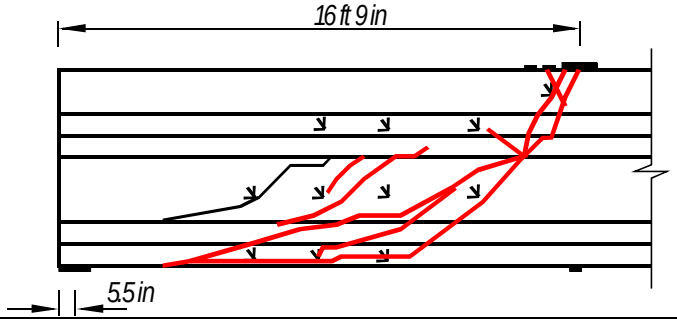

Type III AASHTO Girders – a/d=4 in Shear Test (Second Test)

Load Deflection Plot

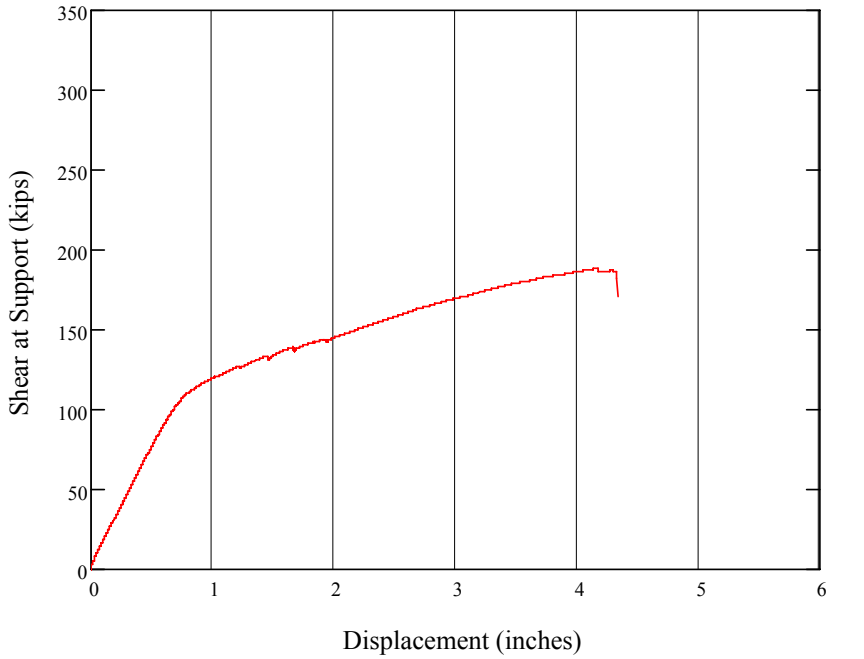

Diagram of Crack Pattern (Shear at the Support =162 kips)

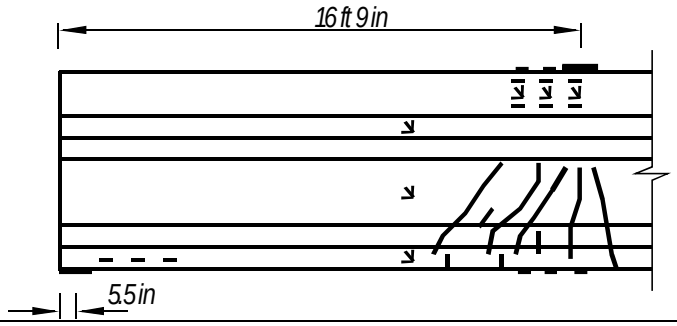

Diagram of Final Crack Pattern

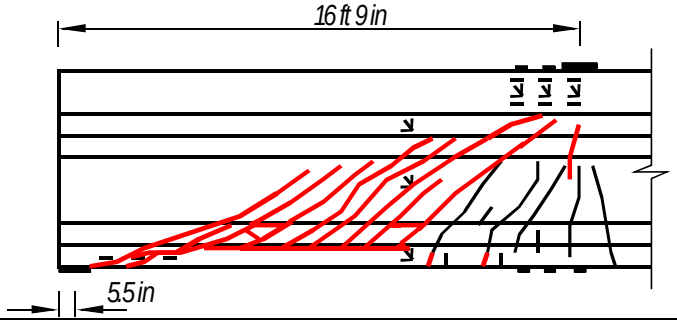

Type III AASHTO Girders – a/d=5 in Shear Test

Load Deflection Plot

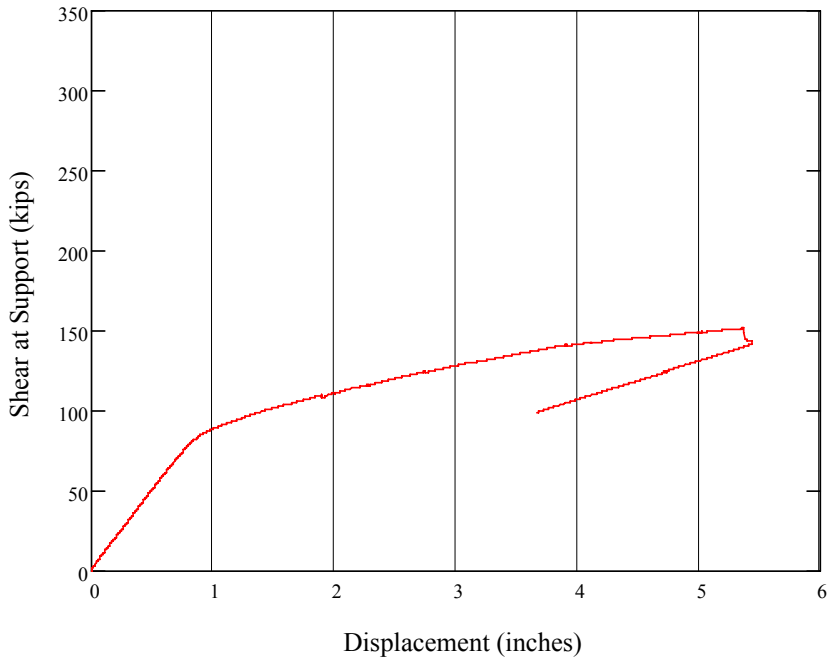

Diagram of Crack Pattern (Shear at the Support = 91 kips)

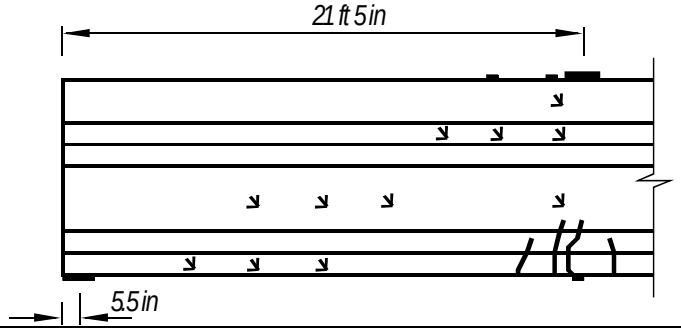

Diagram of Final Crack Pattern

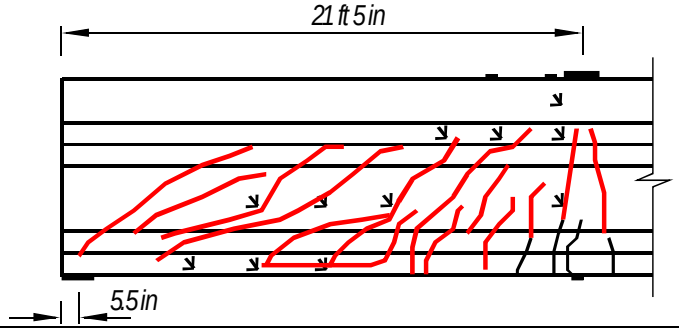

Strain Rosette	First Crack Strain (Max, Microstrain)	First Crack Angle (Degrees)
1R45_49	45	12
1R33_39.5	12	-65
1R45_39.5	75	-72
1R53_39.5	20	60
1R21_24	400	8.5
1R33_24	30	30
1R45_24	170	77
1R53_24	150	67
1R21_4	105	65
1R33_4	160	-8
1R45_4	195	0
2R87.5_49	70	-32
2R65.5_39.5	70	-44
2R75.5_39.5	40	25
2R87.5_39.5	20	-40
2R35.5_24	135	90
2R53.5_24	285	90
2R71.5_24	185	90
2R87.5_24	160	-82
2R5.5_4	275	90
2R23.5_4	130	20
2R35.5_4	135	10
3R137.5_49	135	5
3R107.5_39.5	50	-20
3R125.5_39.5	75	-12
3R137.5_39.5	105	90
3R53.5_24	210	-90
3R71.5_24	240	90
3R87.5_24	180	90
3R137.5_24	250	55
3R35.5_4	120	45
3R53.5_4	150	-10
3R71.5_4	212	-8
4R177_49	45	-10
4R77_39.5	30	-45
4R93_39.5	50	-30
4R129_39.5	75	-10
4R57_24	160	-87
4R77_24	900	90
4R93_24	130	79
4R129_24	135	80
4R57_4	130	25

4R77_4	160	5
4R93_4	200	-10
5R245.5_49	300	-10
5R209.5_39.5	155	-15
5R233.5_395	120	-20
5R245.5_39.5	100	-20
5R155.5_24	225	45
5R173.5_24	190	65
5R191.5_24	190	75
5R245.5_24	240	-90
5R137.5_4	335	0
5R155.5_4	465	-5
5R173.5_4	450	-8